



FACULTY OF SCIENCE
UNIVERSITY OF COPENHAGEN

Physical characterization of phospholipid nanotubes and the effect of BAR domain proteins on their mechanical stability

Ph.D Thesis

Younes Farhangi Barooji

Supervisors:

Lene Oddershede

Seyyed Nader Seyyed Reihani

Advisor:

Poul Martin Bendix

March 2015

List of publications

- P. Ramesh, Y.F. Baroji, S.N.S. Reihani, D. Stamou, L.B. Oddershede, P.M. Bendix; FBAR syndapin 1 recognizes and stabilizes highly curved tubular membranes in a concentration dependent manner; Scientific Reports , vol 3, pp. 1565 (2013)
- Y.F. Baroji, L.B. Oddershede, S.N.S. Reihani, P.M. Bendix; Fluorescent quantification of size and lamellarity of membrane nanotubes. European Biophysics Journal, vol 43, pp. 595-602 (2014).
- Y.F. Baroji, Andreas Rrvig-Lund, Szabolcs Semsey, Lene B. Oddershede, S. Nader S. Reihani, and Poul M. Bendix; IBAR domain proteins: membrane tubulation, stiffness of ABBA coated tubes and reversibility of tubulation (under preparation).

Acknowledgements

This thesis was written in collaboration between two universities: the Optical Tweezers group at the Institute for Advanced Studies in Basic Sciences (IASBS) in Zanjan, Iran and the Optical Tweezers group at Niels Bohr Institute (NBI) in Copenhagen, Denmark. First of all, I would like to thank my supervisors, Seyed Nader Seyed Reihani and Lene Oddershede for their patient guidance, encouragement and immense knowledge. They supported me in every way. I always be grateful to them and will use their advice in my life.

Also, many thanks to my advisor, Poul Martin Bendix, who has keen insights, the excellent knowledge of the instruments and MatLab programming. I will always be grateful for his ideas and encouragement during this process.

I would also like to thank all the members of the staff in the Optical Tweezers group at IASBS and NBI. In particular, I would like to thank Thomas Andersen and Hanne Christensen for their help during my stay in Copenhagen.

Finally, I would like to thank my family, and especially my brothers for their continued support and encouragement.

Abstract

Phospholipid nanotubes are unique assemblies of phospholipid molecules which can be reconstituted *in-vitro*. They are excellent models for studying the biophysics of nanotubes in living cells. With a radial size of ca. 10 nm, they are well suited for studying size effects and the influence of curvature on protein binding. In this project, we used various assays to produce nanotubes, which were subsequently size calibrated by using a new calibration scheme based on fluorescent intensity from fluorophores incorporated in the tubular membrane. The results were used to identify uni- and multilamellar tubes. The shape dynamics of unilamellar tubes was further quantified by tracing the contour of the nanotubes and calculating the correlation between tangent vectors along the contour. This correlation provides a measure for the tube stiffness, which is called the persistence length. More importantly, it was revealed for the first time that persistence length scaled linearly with tube radius. The persistence length analysis of lipid tubes can be useful to understand the mechanical properties of tubes in cells.

The assay for quantifying size and persistence length of freely suspended nanotubes was used to measure the effect of laser excitation of fluorescent tubes with different radial size. During extended illumination, the stiffness was shown to decrease for membrane tubes in a size specific manner.

Identifying the lipid nanotube radius (typically between 10 and 100 nm) by its persistence length and intensity is highly useful for understanding the role of membrane associated proteins in membrane remodeling.

BAR (BinAmphiphysinRvs) domain proteins as a membrane associated proteins play an important role in membrane remodeling, e.g. during the endocytosis process and filopodium formation. Here, the effect of three membranes of the BAR domain family was considered: F-BAR, Arfaptin (classical BAR) and I-BAR. The effect of these proteins on the membrane can be different due to their structure and curvature. We investigated the effect of the F-BAR (Syndapin 1) domain protein on the persistence length of the tubular membranes having different radii. This was achieved by calculating the persistence length of F-BAR coated nanotubes and it was revealed that the stiffness of the F-BAR coated tubular membranes is 5 times higher than protein free tubular membranes. Phospholipid nanotubes (tethers) were also pulled from the vesicle membranes and the curvature sensitivity of the proteins on them was tested against a spectrum of curvatures. We observed that Arfaptin proteins bind very well to the lipid membrane in a low concentration of salt and lead to the tubulation of the membrane. Finally, The tubulation of membranes by I-BAR proteins was quantified. The persistence length of I-BAR coated phospholipid nanotubes was found to increase by factor 2 in comparison to the protein free tubes having the same size.

keywords: Phospholipid nanotube, Vesicle, Persistence length, Optical tweezers, BAR domain proteins

Contents

List of publications	1
Acknowledgements	2
Abstract	3
1 Preface	3
2 Cell membrane and lipid tubes	5
2.1 The cell	5
2.1.1 Cell membrane	6
2.1.2 Inside of the cell	6
2.2 Phospholipid molecules	7
2.3 Self-assembly of phospholipids	9
2.4 Vesicles	10
2.4.1 Spontaneous swelling method	11
2.4.2 Electroformation method	12
2.4.3 Deformed shape of vesicles	12
2.5 Lipids nanotubes	13
2.5.1 Biological lipid nanotubes	13
2.5.2 Artificial lipid nanotubes	14
2.6 Energy associated with bending and stretching a membrane	15
3 BAR domain proteins and their roles in membrane deformation	19
3.1 BAR domain superfamily members	20
3.2 Deformation of the membrane by BAR domains	22
4 The production of spontaneous phospholipid nanotubes and the study of their physical properties	24
4.1 One-end-free phospholipid tubes	25
4.2 Spontaneous free end phospholipid nanotubes	26
4.3 Quantification of the radius and lamellarity of phospholipid nanotubes by their persistence length	27
4.3.1 Phospholipid nanotubes' imaging	28
4.3.2 The tangent vectors on a phospholipid nanotube	29
4.3.3 Phospholipid nanotubes radius	31
4.3.4 Multilamellar Phospholipid nanotubes	34

4.4	The tubular vesicle	36
4.5	The effect of fluorescent illumination on tube stiffness	37
4.6	Conclusions	39
5	Curvature-sensing of BAR domain proteins and tubulation of membranes by them	40
5.1	The effect of F-BAR on phospholipid nanotubes	41
5.1.1	F-BAR senses curvature on a tether pulled by optical tweezers	41
5.1.2	Curvature sensitivity of F-BAR on tethers with different diameters	43
5.1.3	Investigation of the stability of a F-BAR coated tether by optical tweezers	44
5.1.4	The persistence length of F-BAR coated phospholipid nanotubes	45
5.1.5	Tubulation of the vesicle membrane in the presence of the F-BAR	46
5.2	Arfaptin coated phospholipid nanotubes	46
5.3	I-BAR coated phospholipid nanotubes	48
5.3.1	Tubulation by I-BAR domains can be reversibly controlled by protein concentration	48
5.3.2	Tubulation by I-BAR domains can be reversibly controlled by the membrane surface tension	51
5.3.3	The persistence length of I-BAR coated phospholipid nanotubes	53
5.3.4	Making inward tubes by optical tweezers without and in presence of I-BAR	54
5.4	Conclusions	56
6	Conclusions and outlook	57
7	Appendices	59
7.1	Appendix A	59
7.2	Appendix B	62
7.3	Appendix C	63
8	Articles	73

Chapter 1

Preface

In recent years, physicists and biologists have collaborated to solve interesting problems in biological system. This relatively new field of biophysics has been quite successful, for instance in understanding mechanical properties of cell membranes and their deformation in processes, such as exo- and endocytosis, cell migration and filopodia formation. Observing the mechanical aspect of these processes has become more achievable by developing tools, e.g. confocal and fluorescent microscopy, optical tweezers and micro-manipulation systems.

In this thesis, we aim to measure the mechanical properties of artificial membrane nanotubes. In our research, three types of membrane nanotubes were created and investigated under confocal microscopy. First, spontaneously forming fluorescently marked phospholipid nanotubes were produced from the swelling of phospholipids on a glass surface and their radii was found by measuring their persistence length and intensity. The second kind of nanotube was created by pulling a tether from a vesicle membrane using optical tweezers and the third kind was produced by the tubulation of the vesicle membrane during the binding of BAR (Bin, amphiphysin, Rvs domain) domain proteins. The concrete goals of the project were to measure the persistence length and diameter of these three kinds of phospholipid nanotubes and explore the curvature sensitivity of BAR domain proteins.

Thesis outline

- Chapter 2 gives an introduction of a cell and the membrane deformation process, a short history about the production of an artificial membrane, and the energy equations describing the membrane deformation which were used in this thesis.

- In chapter 3, BAR domain proteins are introduced and their role in membrane curvature is discussed. From the BAR domain superfamily, we used three members (F-BAR (Syndapin 1), Arfaptin and I-BAR) to explore the role of these proteins in sensing and inducing curvature on membranes.
- Chapter 4 includes the method that we utilized to create spontaneous phospholipid nanotubes and to quantify lamellarity of phospholipid nanotubes by measuring their persistence length and radius. At the end of this chapter there are experiment observations about the conversion of nanotubes to tubular vesicles and the effect of illumination on their persistence length.
- Chapter 5 includes the experiment observations and physical measurements of curvature sensitivity of F-BAR domain proteins on tether and spontaneous phospholipid nanotubes. The tubulation of the vesicle membrane was observed by binding F-BAR and Arfaptin, which is discussed in this chapter. In addition, the chapter includes a discussion on the reversibly of tubulation versus I-BAR concentration or increasing membrane tension by micropipette aspiration.
- Appendix A : Persistence length equations
- Appendix B : Power spectrum method for calibrating optical tweezers
- Appendix C : Production of vesicles and chamber preparation

Chapter 2

Cell membrane and lipid tubes

Firstly, in this chapter, there is a short introduction to the properties of cell membranes and some of their components. Then the self-assembly of lipid molecules and artificial membranes are discussed along with a focus on cylindrical and spherical membrane shapes. Finally, equations describing the energy and the effect of membrane curvature are explored. Introducing a cell and the equations of the membrane manipulation will aid in understanding the results on the vesicles membrane, which will be presented in chapters 4 and 5.

2.1 The cell

The word "cell" comes from the Latin *cella* and means a small room. Cells are the basic biological structure of living organisms and they can replicate independently. The size of a cell is microscopic with a diameter between 5-100 μm . Cells have a variety of sizes, shapes and they have a various functions depending on their location in the body. For example, white blood cells destroy harmful bacteria and protect the body against infection such as in wounds. Neuronal cells are long and have filaments to deliver messages from the brain to the other parts of body and vice versa. The skin is a barrier which protects muscles and the internal part of body from the outside. Skin cells should therefore have sufficient thickness and should replicate as soon as a wound emerges. Red blood cells, which deliver oxygen through the vessels, are flexible as it is crucial for them to change their shape when crossing a thin vessel. In short, there are a variety in shapes and functions of cells, but they generally contain similar components and structure. Figure 2.1 presents a schematic of a typical cell and in the following subsections, their cellular components will be briefly described.

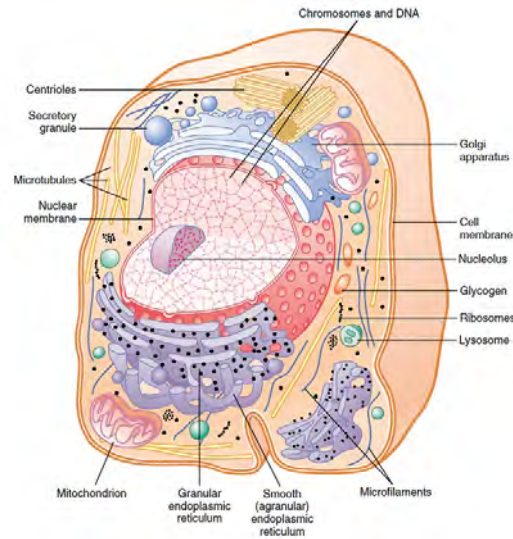


FIGURE 2.1: A Schematic of a typical cell

2.1.1 Cell membrane

The cell membrane is a wall composed of lipid molecules and proteins which separates the inside and outside of the cell and has a thickness of 5 nm [1, 2]. Besides providing protection, the function of a membrane is to deliver material into and out of the cell. The cell membrane contains 55% proteins and 45% lipids (25% phospholipids, 13% cholesterol, 3% carbohydrates, 4% other lipids). Membrane lipids are amphiphile molecules which have a polar head (water loving) and a non-polar tail (fat loving). To protect the lipid tails from water in the cell, the lipids assemble into bilayers with the tails facing each other and the polar head comes together facing the water phase, as shown in Figure 2.2. Membrane proteins are also delivery channels facilitating the transport of material into and out of the cell. The intermediate layer of the membrane is hydrophobic and ion (polar) materials are not able to cross the membrane apart from through the designated protein channels.

2.1.2 Inside of the cell

Cells are organized into two groups: eukaryote with a nucleus and prokaryote without a nucleus [1, 2]. The nucleus of cells is involved in protein production, synthesis and cell division. The endoplasmic reticulum is around the nucleus with ribosomes that synthesize proteins. After proteins are made in the reticulum, they are transported to the Golgi apparatus by a small spherical bilayer (vesicle). The Golgi apparatus is a series of flattened, stacked pouches called cisternae. Vesicles from endoplasmic reticulum carry proteins to the Golgi where proteins synthesize there. Finally, proteins and lipids are

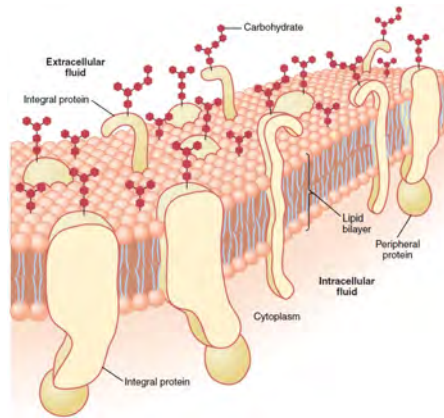


FIGURE 2.2: Structure of membrane bilayer

packaged into vesicles for delivery to target destinations.

Another important component in cells is the cytoskeleton which acts to organize and maintain the cell's shape. The eukaryotic cytoskeleton is composed of microfilaments (actin filaments), intermediate filaments and microtubules.

2.2 Phospholipid molecules

As mentioned in subsection 2.1.1, the cell membrane contains 25% phospholipid molecules. Phospholipids are used to produce artificial membranes such as liposomes and vesicles. As it has been shown in Figure 2.3, phospholipid molecules have two parts: a polar head group typically consisting of a choline, serine or ethanolamine and a hydrophobic part usually consisting of 2 long fatty acid hydrocarbon chains (CH_2). There are two groups of fatty acids, saturated and unsaturated. An unsaturated fatty acid refers to the presence of one or more double bonds between carbons and a saturated fatty acid is saturated with hydrogen and thus does not contain double bonds.

Phospholipids can exist in different phases, referred to as ordered and disordered. In the absence of cholesterol, these phases are the gel and the liquid phase. In the liquid phase, the tails of the molecule are more flexible than in the gel phase. For each kind of phospholipid, there is a specific transition temperature which is sensitive on the length and saturation level of the fatty acid chains. The transition temperature decreases by the number of unsaturated carbon double bonds and the length of fatty acid chains. Two kinds of phospholipid molecules "POPC" and "PC" are shown in Figure 2.4 which have -2 and 33 degree centigrade transition temperatures respectively. Many types of phospholipids are produced in the purified form for research purposes. Two well-known companies which produce these molecules are: Avanti Lipids (<http://www.avantilipids.com>) and Sigma-Aldrich (<http://www.sigmaaldrich.com>).

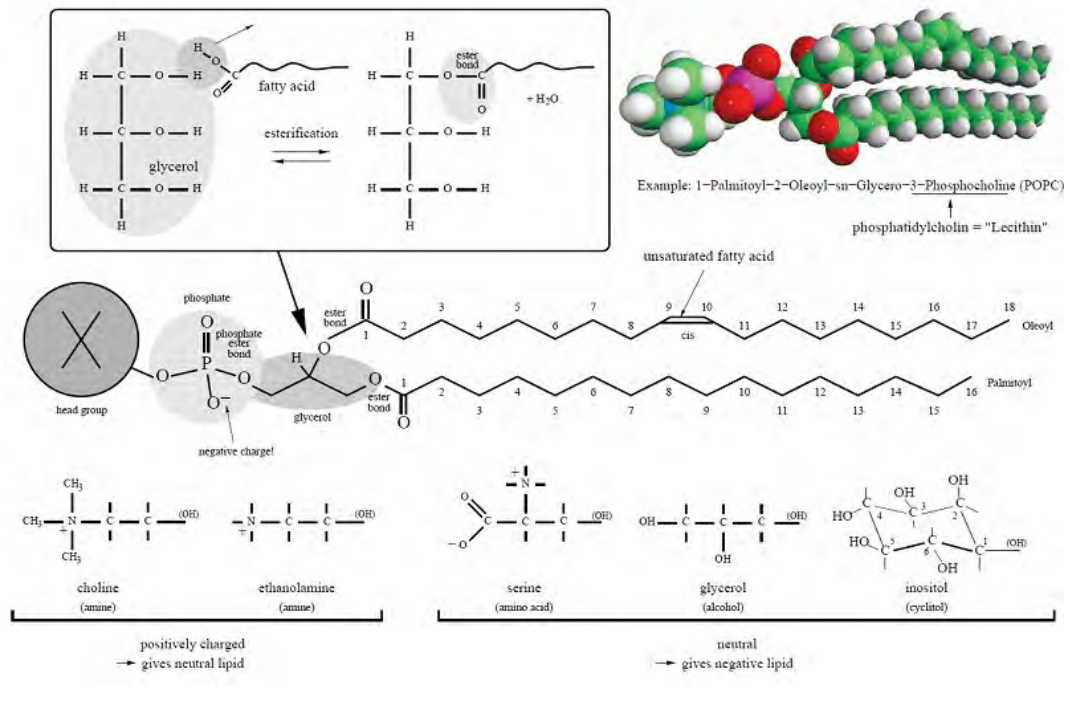


FIGURE 2.3: a typical structure of a phospholipid molecule

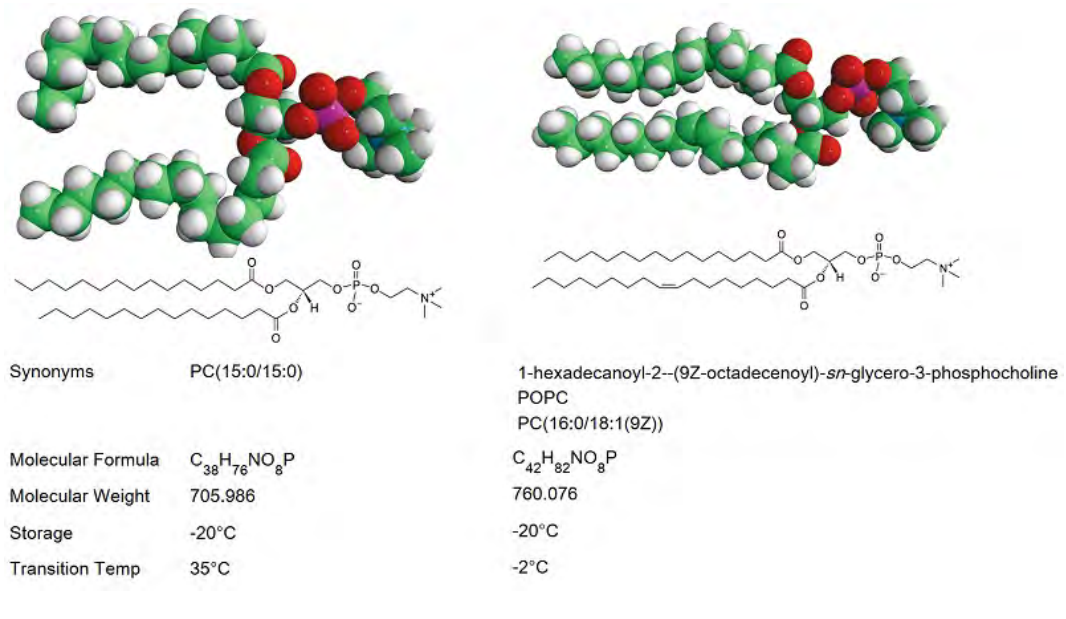


FIGURE 2.4: Two different phospholipid molecules; POPC and PC

2.3 Self-assembly of phospholipids

As mentioned in the previous section, phospholipids are amphiphil molecules which produce self-assemble structures in the polar solution such as water, sucrose and sorbitol. Figure 2.5 shows the self-assembly structure in which the hydrophobic tails of the molecules have been sandwiched between hydrophilic heads. The shape of a phospholipid determines which structure can be produced after the molecules have been assembled. In 1976 Israelachvili and his colleague considered parameters which determine the kind of structure based on the molecular shape of the lipid [3]. The three parameters presenting a phospholipid molecule's shape include the length of the hydrocarbon chain (l_c), the volume of the space that the chain occupies (v) and the effective area of molecule's head (a). For example, for a spherical micelle with the radius of R which contains N phospholipids, the area and the volume of the micelle is given by :

$$S = 4\pi R^2 = Na \quad (2.1a)$$

$$V = \frac{4}{3}\pi R^3 = Nv \quad (2.1b)$$

by combining two equations, the radius of the micelle is derived $R = 3v/a$. On the other hand, the tail parts of molecules occupy inside of sphere, so the radius of sphere is smaller or equal with radius, $R = 3v/a \leq l_c$. This result is $P = v/al_c \leq 1/3$ where P is called the packing parameter. There are similar conclusions for other self-assembling structures :

$$\frac{1}{3} \leq \frac{v}{al_c} \leq \frac{1}{2} \quad \dots\dots\dots \text{cylindrical micelle} \quad (2.2a)$$

$$\frac{1}{2} \leq \frac{v}{al_c} \leq 1 \quad \dots\dots \text{planar structure, vesicles and tubs} \quad (2.2b)$$

$$1 < \frac{v}{al_c} \quad \dots\dots\dots \text{inverse structure} \quad (2.2c)$$

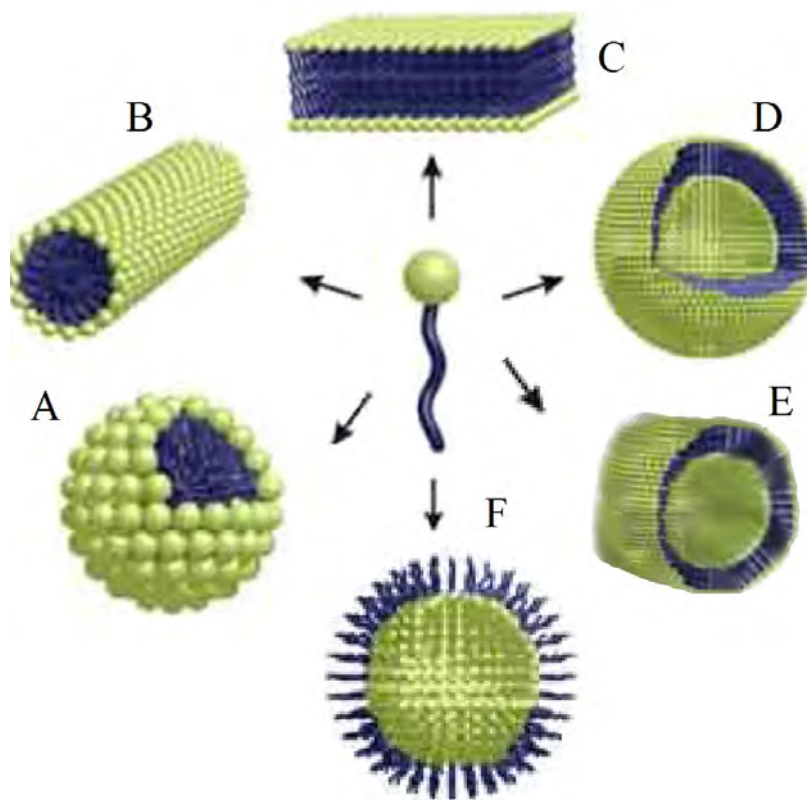


FIGURE 2.5: Self-assembly of Amphiphil molecules; spherical micelle (A), cylindrical micelle (B), planar structure (C), Vesicle (D), cylindrical vesicle (E) and inverse structure (F).

2.4 Vesicles

Liposomes are small vesicles (a few tens of nanometers in diameter) that exist as transport carriers within cells. These vesicles are associated with both endo- and exocytosis during the transport of molecules across, for example, the plasma membrane, see Figure 2.6 [1, 4]. During these processes, vesicles bud off and fuse with the plasma membrane thus facilitating loading and delivery of molecules across the membrane. In our research, we considered artificial vesicles which are produced in the lab. The small size of vesicles (diameter $<$ micrometer) is a very good model for biological vesicles. Giant vesicles (diameter $>$ a few micrometers) are good models for the cell membrane. In 1960 Bangham and his colleague observed small and spherical vesicles under electronic microscopy for the first time [5]. Subsequently, many researchers from physics, chemistry and biology have worked to produce vesicles with a different radius and lamellarity. These days vesicles are produced with various models, e.g. Small Unilamellar Vesicles (SUV), Giant Unilamellar Vesicles (GUV), and Large Multilamellar Vesicles (LMV). There are various methods to produce these different kinds of vesicles, some of which can be found on

"<http://www.avantilipids.com>" and references [6–9]. Recently, there has been much research on the application of vesicles in drug delivery and researchers have introduced new methods for making vesicles with drugs and genes inside the vesicle [10]. In the following subsections, the two main methods of vesicles' production, which have mostly been used by researchers are explained.

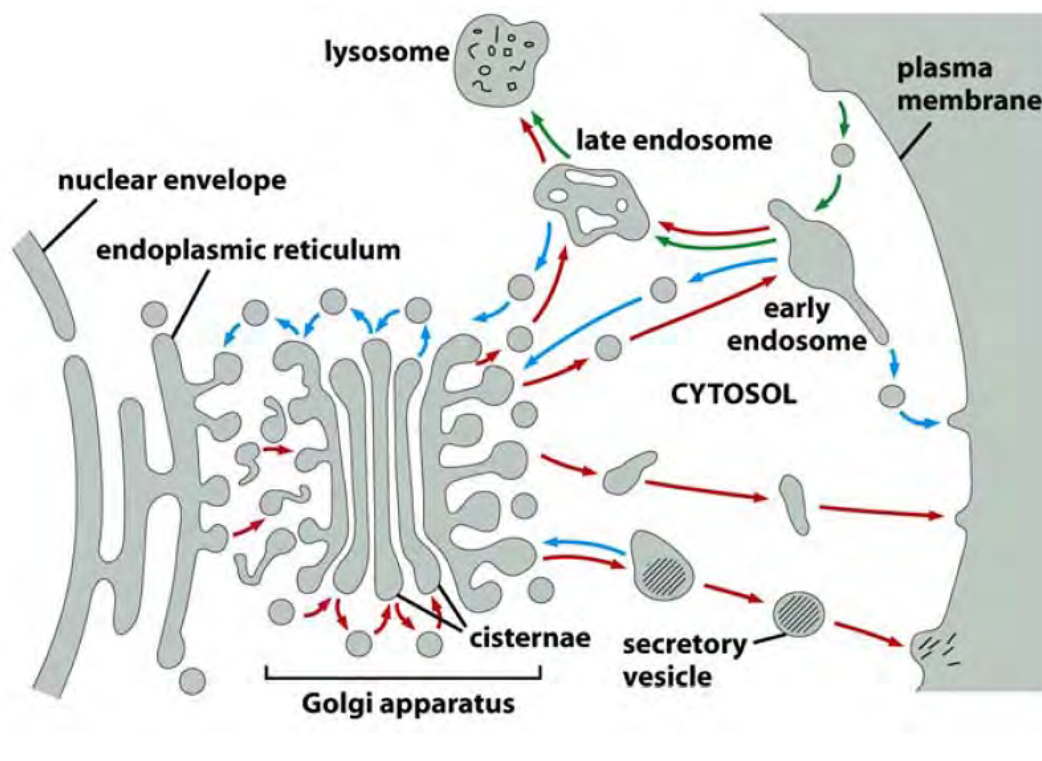


FIGURE 2.6: Vesicle trafficking inside the cell [1].

2.4.1 Spontaneous swelling method

The spontaneous swelling method was presented by Reeves and Dowben [8]. Following them, researchers have adapted and optimized this method to produce unilamellar vesicles with desired sizes. In short, there are 6 steps in the spontaneous swelling:

- 1) The stock solution is prepared mixing of the phospholipids in chloroform (methanol) in the desired molar ratio. The stock solution should be kept at -20 degrees centigrade.
- 2) 50 μl of solution from (1) is coated and dried by using a glass syringe on a teflon surface (a teflon cup is usually about 3 cm in diameter and height).
- 3) The coated surface is placed under nitrogen gas for several minutes for more evaporation of the chloroform.
- 4) To gain complete evaporation of the chloroform, the cup is put into a vacuum chamber for 2-3 hours.
- 5) Swelling solution (Phosphate Buffered Saline (PBS), sucrose, etc) is added to the cup

and the top is sealed with parafilm to prevent evaporation of the solution.

6) The lipid film is allowed to swell during the gentle hydration at a higher temperature than the transition temperature of phospholipids for 6-12 hours. During this time the lipid film swells to form both multi- and unilamellar lipid vesicles.

2.4.2 Electroformation method

The electroformation method is used to produce GUVs by most researchers and it was first presented by Angelova in 1986 [9]. There have been changes to this method since then in order to optimize vesicle production and we used this method to produce GUVs. The steps of this method are similar to the spontaneous swelling method. In this method phospholipids were coated on the Indium Tin Oxide (ITO) surface of the coverslip. The coated coverslip was put under nitrogen gas for several minutes and then placed into a vacuum chamber. After 2 hours an o-ring was placed on the top of coated area and filled with swelling solution. Another ITO coverslip was put on the top of the o-ring and the solution was then sandwiched between ITO coverslips. Next, an AC electric voltage (10 Hz, 1.5 V) was applied between the plates for 2 hours and the GUVs were produced. GUVs are mostly unilamellar and big in size (20-50 μm in diameter) in comparison to the spontaneous swelling method.

2.4.3 Deformed shape of vesicles

Phospholipid membranes are flexible and become deformed by changing the parameters such as with osmotic pressure, a medium viscosity and lipid mixture [11]. Deformation of red blood cells due to osmotic pressure and in certain diseases has been observed [12, 13]. One interesting property of the membrane deformation is the budding of small vesicles from the main membrane, also called a bleb. The budding of the vesicles has been observed and studied in biological cell division [14] and artificially *in-vitro* condition in vesicles [13, 15, 16]. As an example, Figure 2.7 shows deformed shapes of vesicles in the presence of peptides $A\beta$. $A\beta$ leads to an increase in the membrane area, inducing vesicle transformation.

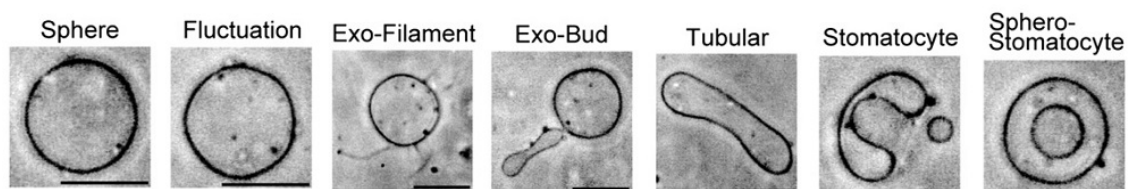


FIGURE 2.7: Deformation of a vesicle membrane in the presence of peptides $A\beta$ [13].

2.5 Lipids nanotubes

In this section, an explanation concerning lipid nanotubes is given. Firstly, the subsection introduces biological lipid nanotubes which are observed in biological systems or produced experimentally on the cell membrane. In the second subsection, the artificial phospholipid nanotubes are discussed, which are a good experimental model for cellular tubes. Phospholipid nanotubes are also useful in the investigation of membrane associated proteins in membrane remodeling. In our work, we produced phospholipid nanotubes and used them to consider the effect of BAR domain proteins on the membrane, which will be discussed in chapters 4 and 5.

2.5.1 Biological lipid nanotubes

Membrane nanotubes with a radius of about 100 nm can be extracted from the red blood cell membrane. These kinds of membrane nanotubes were stretched by a fluid shear stress with a length of up to 10 μm [17]. Short length membrane nanotubes have also been observed in the endoplasmic reticulum and the golgi apparatus by electron microscopy [18, 19]. Also motor proteins on microtubular play an important role in the formation of these kinds of nanotubes [20]. There are other kinds of nanotubes which emerge from the cell membrane and are caused by the polymerization of cytoskeletal filaments. Membrane filaments are made by the polymerization of actin filaments or microtubular. Polymerization forces are enough to curve the membrane and stretch it [21, 22]. Filopodias grow, shrink, and act as sensing structures for the cell to probe the microenvironment. Also, filopodias have the ability to interact with external objects such as bacteria and artificial nanotopographies [23–25]. The growing and shrinking of filopodia from (and to) membranes can not be done solely by actin filaments; another class of proteins involved in the deformation of membranes are called BAR (BinAmphiphysinRvs) domain proteins. These proteins play an important role in sensing membrane curvatures and bending membranes into shapes that are dictated by their intrinsic molecular shape [26, 27]. These proteins will be discussed more in chapter 3.

Lipid nanotubes have also been observed between cells which are called intercellular nanotubes [28–32]. They help to deliver materials between two cells directly. Material delivery is useful for the biological balance between cells, but it has been determined that these nanotubes also would allow neurons to transport an infectious agent composed of protein [33]. Transmission of HIV-1 via intercellular connections has been estimated as 100-1000 times more efficient than a cell-free process [34].

Figure 2.8 shows various membrane nanotubes and filaments that have been mentioned.

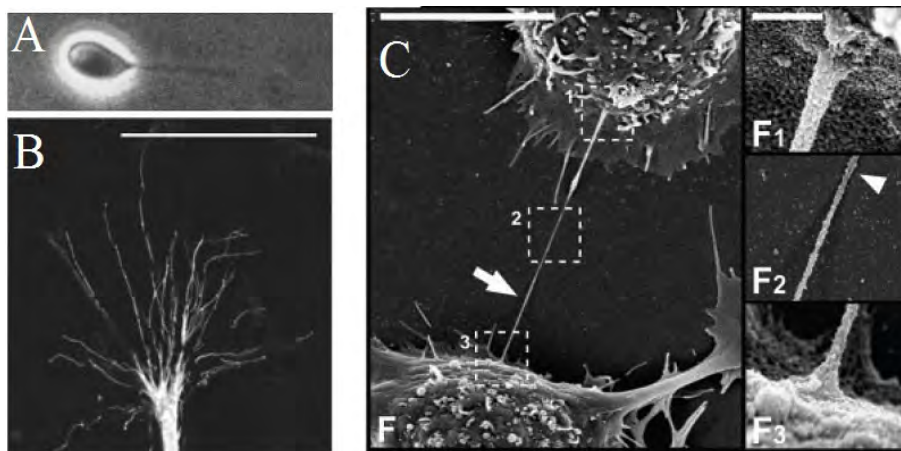


FIGURE 2.8: Biological membrane nanotubes: A) Stretched nanotubes from the red blood cell membrane by fluid stress[17]. B) Filopodias from endothelia [35]. C) Inter-cellular nanotubes between PC12 [28].

2.5.2 Artificial lipid nanotubes

Artificial lipid nanotubes are produced from phospholipid molecules and other amphiphilic molecules (without the phosphate head) [36]. Phospholipid nanotubes with properties such as flexibility and rigidity are more like biological lipid nanotubes and are good experimental models of cellular tubes. Artificial phospholipid nanotubes, which are produced experimentally, can be classified into 3 categories:

Tethers: These nanotubes are extracted by applying a point force on the vesicle membrane. The point force can be applied by mechanical manipulation [37, 38], optical or magnetic tweezers (Figure 2.9 A) [22, 39, 40], motor proteins [41], and microtubular polymerization (Figure 2.9 B) [22]. Phospholipid nanotubes (diameter 100 nm- 1 μm) also are pulled out of the membrane by fluid flow (Figure 2.9 E) [42, 43] or applying an electric field on the coated lipid stock [44].

Protein coated nanotubes : Membrane associated proteins (e.g. BAR domain proteins) can bind to a membrane and change its curvature. BAR domain proteins are able to tubulate a lipid membrane. The extent of tubulation depends on the protein concentration whereas the diameter of the resulting tubules depends on the molecular shape of the protein (2.9 D) [45–47].

Free ends spontaneous phospholipid nanotubes: These kinds of nanotubes have been produced recently by mechanical manipulations and swelling techniques (Figure 2.9 C) [48, 49].

Figure 2.9 illustrates artificial phospholipid nanotubes.

In our research, we produced these 3 types of nanotubes which will be explained in chapters 4 and 5.

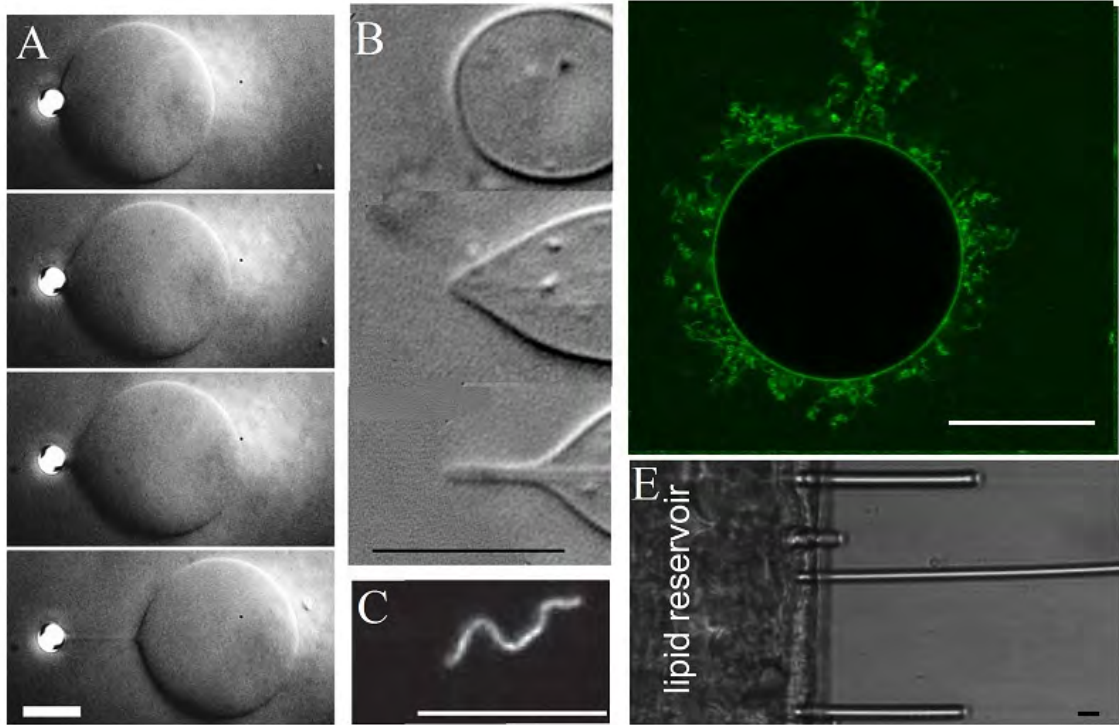


FIGURE 2.9: Phospholipid nanotubes : A) A pulled nanotube from a vesicle membrane (tether) by optical tweezers [40]. B) Polymerization of microtubules inside a vesicle [22]. C) Free ends-phospholipid nanotubes [48]. D) Arfaptin proteins lead to tubulation of membrane. E) Fluid flow on the lipid stock (reservoir) forms lipid tubes [42]. The scales are $10 \mu\text{m}$.

2.6 Energy associated with bending and stretching a membrane

The bending energy of a membrane with area A and two principal curvatures of C_1 , C_2 is given by [50]:

$$E_H = \frac{\kappa}{2} \oint (C_1 + C_2 + C_0)^2 dA + \kappa_G \oint C_1 C_2 dA \quad (2.3)$$

where κ is the bending rigidity constant. C_0 is the spontaneous curvature of the membrane (characterizing the asymmetry of the membrane if either the lipid composition or the surrounding medium is different on the two sides). The integral covers the entire surface of the membrane [51]. κ_G is the Gaussian bending rigidity and corresponds to the changes in topology [52, 53]. For a symmetric vesicle membrane with a constant topology, equation 2.3 is rewritten as:

$$E_H = \frac{\kappa}{2} \oint (C_1 + C_2)^2 dA . \quad (2.4)$$

So then for a vesicle with a radius R ($C_1 = C_2 = 1/R$):

$$E_H = 8\pi\kappa . \quad (2.5)$$

And for a tubular membrane with the radius of r and the length of l ($C_1 = 0, C_2 = 1/r$):

$$E_H = \frac{\kappa\pi l}{r} . \quad (2.6)$$

The bending rigidity is an important parameter considering physical and mechanical properties of the membrane. There are several ways [54] to measure the bending rigidity, but the two main methods are: fluctuation spectroscopy, in which the physical parameters are extracted from the thermal undulations of the membrane [55] and the micropipette aspiration method [56, 57], in which a part of the vesicle membrane is aspirated into the micropipette and the vesicle is held by the aspiration pressure P (Figure 2.10). The relation between the membrane tension and the aspiration pressure is given by Law of Laplace:

$$\sigma = \Delta P \frac{R_p}{2(1 - R_p/R_v)} \quad (2.7)$$

where $\Delta P, R_p$ and R_v are the aspiration pressure, micropipette and vesicle radius respectively. Measuring the relative area change allows for extracting the value of the bending rigidity [58]:

$$\frac{A - A_0}{A_0} = \frac{k_B T}{8\pi\kappa} \ln\left(1 + 0.1 \frac{\sigma A}{\kappa}\right) + \frac{\sigma}{k_a} \quad (2.8)$$

where k_a is the stretching elasticity modulus of the lipid membrane. For a membrane with a thickness of h , the stretching elasticity is given by: $k_a = \alpha\kappa/h^2$ where α is a numerical constant. A_0 would be extracted from the radius of the vesicles (R_0) in the beginning of aspiration ($A_0 = 4\pi R_0^2$). The proportionality between the apparent area and the aspiration length (L_p) can be approximately estimated using the following [59]:

$$\Delta A \approx 2\pi R_p \left(1 - \frac{R_p}{R_v}\right) L_p \quad (2.9)$$

In a typical experiment, different aspiration pressures can be applied to a membrane leading to different aspiration lengths. Then for each length, the value of the tension and the relative area change are calculated from equations 2.7 and 2.9. Finally, a diagram of $\Delta A/A_0$ versus σ is plotted and, using equation 2.8, the magnitude of κ and k_a are calculated.

The bending rigidity is a small value and the experimental results are sensitive to the magnitude of the bending rigidity. Researchers usually find different numbers for the bending rigidity, for example, for the POPC membrane, the bending rigidity has been reported between $3 - 15 \times 10^{-20} J$ [54].

For a vesicle with the surface area, A , and the volume of the vesicle, V , the free energy

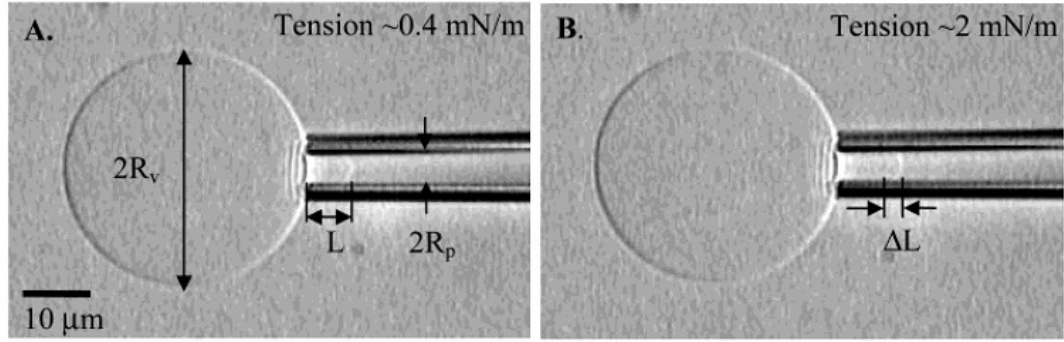


FIGURE 2.10: Micropipette aspiration experiment [60].

of the membrane can be written [61]:

$$F = E_H + \sigma A - PV \quad (2.10)$$

where P is the inside pressure (relative to the outside) and is zero when a vesicle is suspended in an isotonic medium.

If a point force, f , is used to extract a tether with radius r and length l from a vesicle membrane (see Figure 2.11), the free energy of the nanotube (tether) using equations 2.6 and 2.10, is written ($P=0$):

$$F = \frac{\kappa\pi l}{r} + 2\pi r l A - fl \quad (2.11)$$

By minimizing F with respect to radius we see that the surface tension reduces the radius and the bending rigidity works to increase the radius. By minimizing the energy in eq. 2.11 with respect to radius and length, the equilibrium radius r and force f become:

$$\frac{\partial F}{\partial l} = 0 \Rightarrow f = 2\pi\sqrt{2\sigma\kappa} \quad (2.12a)$$

$$\frac{\partial F}{\partial r} = 0 \Rightarrow r = \sqrt{\frac{\kappa}{2\sigma}} \quad (2.12b)$$

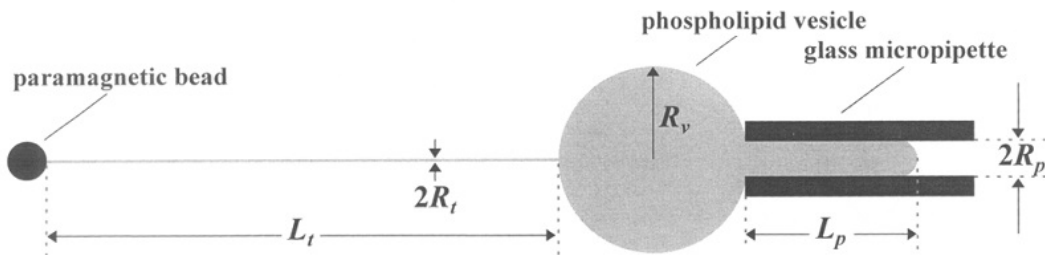


FIGURE 2.11: Optical Tweezers - Micropipette aspiration method [39].

If the tether has been cut from the attached point on the membrane, it would shrink and convert to a spherical shape to minimize the bending energy. For example, a nanotube with radius, $r = 20 \text{ nm}$ and length, $l = 100 \text{ }\mu\text{m}$ converts to a sphere membrane with radius, $R = 1 \text{ }\mu\text{m}$ (with a constant area constraint, $R = \sqrt{0.5rl}$). By using a typical number of the bending rigidity, $\kappa = 40 \text{ pNnm}$ and the surface tension of the membrane, $\sigma = 0.05 \text{ pN/nm}$, the nanotube has a bending energy of $E_H = 628000 \text{ pNnm}$ (equation 2.6), which is much greater than the bending energy of a spherical vesicle, $E_H = 1000 \text{ pNnm}$ (equation 2.5). Therefore, with regard to the bending energy, transformation of a nanotube to a spherical vesicle is favorable. During this transformation the volume changes whereas the area of the membrane is constant. For a lipid nanotube there is a difference in area between the outer and inner leaflets of the membrane bilayer. For a bilayer with the thickness of h , the difference in area is calculated as $2\pi hl$ by subtracting the inner leaflet area, πrl , from the outer leaflet area, $2\pi(r+h)l$ (see Figure 2.12) [49]. In contrast to a nanotube, the difference in area is negligible as the vesicle radius is much bigger than the bilayer thickness ($R \gg h$). Therefore, during transformation, half of the lipids in the extra area of the outer leaflet of the nanotube, $2\pi hl$, should transport to the inner leaflet. This process costs an energy which opposes nanotube-vesicle transformation. In this project, we also considered the conversion of nanotubes to tubular vesicles in the 2D chamber which will be discussed in chapter 3.

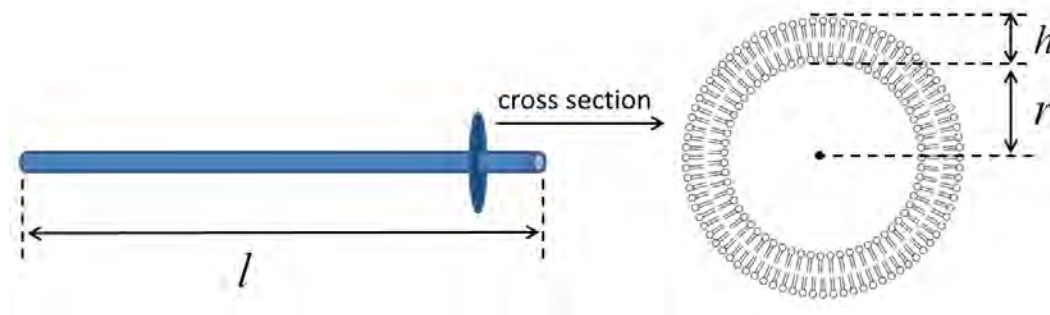


FIGURE 2.12: Drawing of a phospholipid nanotube which shows its geometrical parameters.

Chapter 3

BAR domain proteins and their roles in membrane deformation

BAR domain proteins bind to membranes with different curvature preferences. They sense membrane curvature and stabilize it by electrostatic binding to the membrane and inserting amphiphatic helices into it. They play a role in biological system such as cell division, vesicle budding , and cell migration [46, 47]. These proteins bind to membranes by electrostatic interaction between negative charges of the membrane and positive charges on the BAR domain. The shape of BAR domains exhibits various positive and negative curvatures and the charges are on the curved face. In the binding process, BAR domains induce their curvatures on the membrane. In this chapter there will be a short explanation concerning BAR domain types, shapes, and their interaction with membranes. In chapter 5, I will explain how the curvature sensitivity of BAR domain proteins on the vesicle and tube membrane was quantified.

3.1 BAR domain superfamily members

Arfapin's protein structure (classic BAR) was first presented by Walker et al in 2001 [62] while the structures of other BAR domain proteins were revealed in 2004 [63], especially regarding their size and curvature [64–66]. Figure 3.1 shows the structure of the family members and their subfamily. These domains can be classified into 4 different domains: *Classical BAR domain*: The concave face of this protein has positive charges, which allows the protein to bind to the membrane.

N-BAR domain: This type of the BAR domain has two N-terminal amphipathic helices. In binding with membranes, the helices are inserted into the hydrophobic part of the bilayer, which induces curvature on the membrane and so then the BAR domains stabilize it.

F-BAR domain: This domain also has an intrinsic crescent shape and binds to membranes via its concave face. F-BAR domains contain two hydrophobic wedge loops which are inserted into the lipid bilayer during the binding of the BAR to the membrane.

I-BAR (inverse BAR) domain: There are three types of I-BARs called ABBA (Actin-Bundling protein with BAIAP2 homology), MIM (Missing In Metastasis) and IRSp53 (Insulin receptor phosphotyrosine 53kDa substrate). The positive charges are on the convex face of the domain. Thus, the I-BAR domains bind to a membrane and stabilize negative curvatures in contrast to the classical BAR domains, which sense and induce positive curvature.

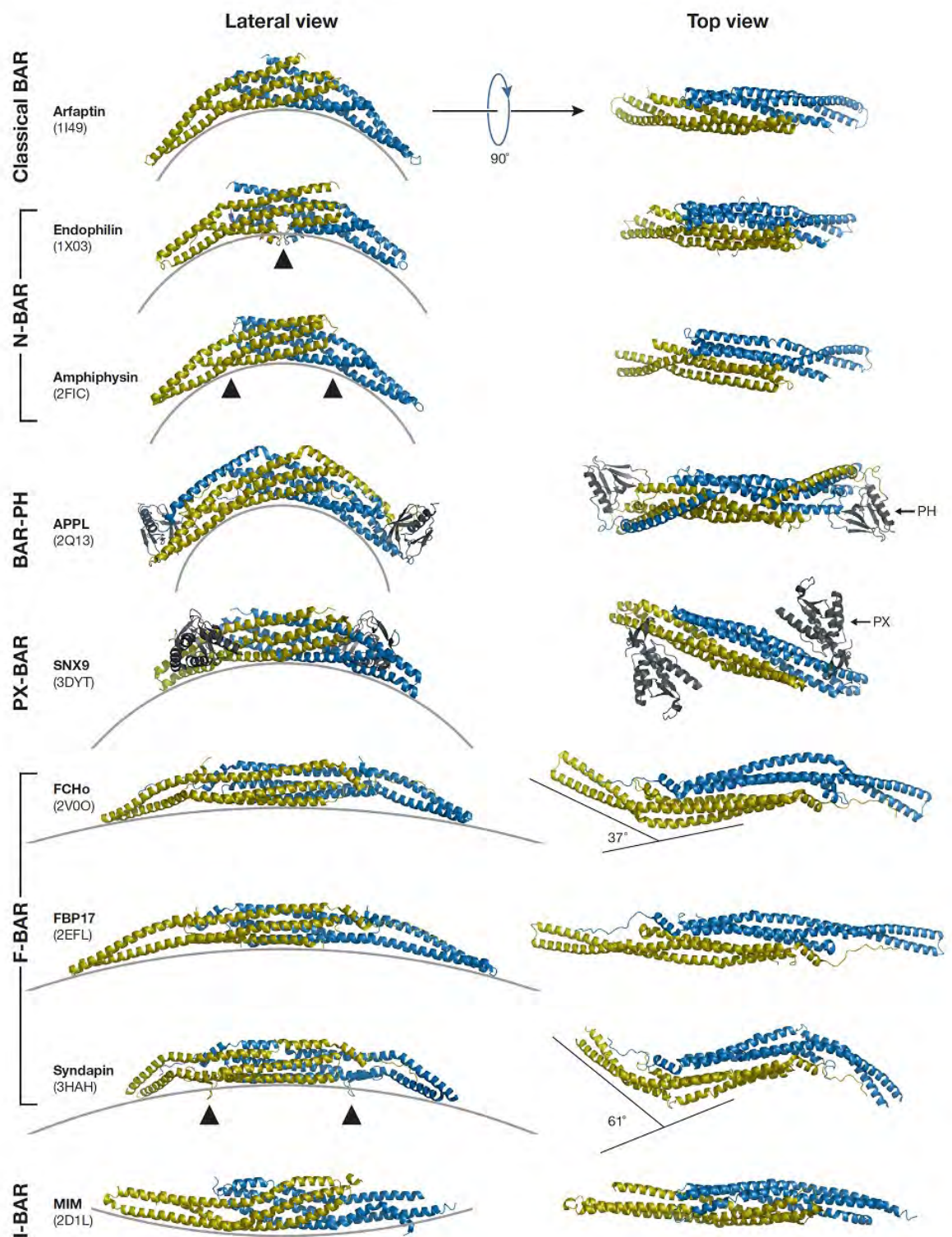


FIGURE 3.1: BAR modules (one monomer in yellow and the other in blue) viewed from the side (left) and from the top (right) [66].

3.2 Deformation of the membrane by BAR domains

Membranes change curvature during biological processes, such as cell division, vesicle budding, endo- and exocytosis, membrane fusion, cell migration, and in the growth of filopodia. One of the important mechanisms which lead to a curvature change on the membrane is polymerization of intracellular filaments, associated with the binding of proteins. Figure 3.2 A shows schematically how a membrane is curved by this mechanism [26]. BAR domain proteins, in particular domains containing amphiphatic alpha helices, play an important role in both bending of membranes and sensing membrane curvatures. Figure 3.2 B presents a model for the generation of membrane curvature by BAR proteins.

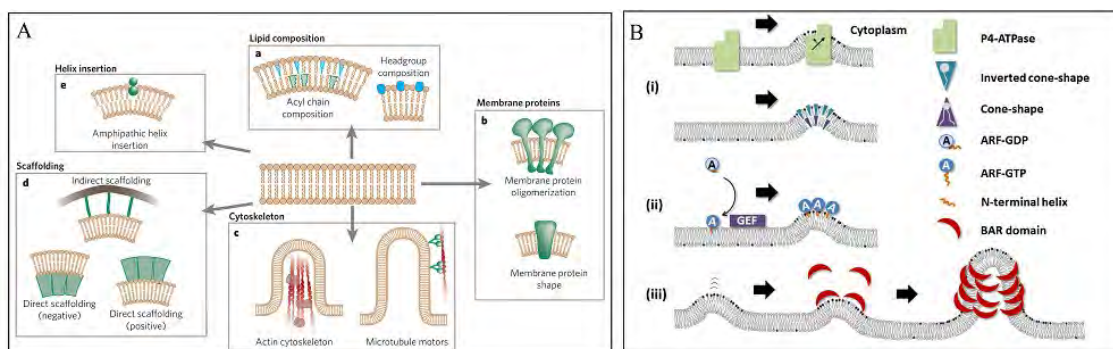


FIGURE 3.2: A) Five main categories for the process of membrane deformation [26]. B) Membrane deforming mechanism which shows how BAR domains induce curvature [27].

As previously mentioned, it seems in biological systems, deformation of a membrane begins with other proteins and BAR domain proteins mostly sensing and stabilizing the curvature on the membrane. However there have been several different mechanisms presented that describe the role of BAR domains in membrane deformation and it will take more experimental research to determine exactly how BAR proteins affect membrane curvature. So far, it has been observed that domains with amphiphatic helices induce preliminary curvature by inserting helix into a leaflet of the membrane and the BAR domains reinforce and stabilize it [26]. The tubulation of membranes has been observed in the presence of Arfapatin and N-BAR *in-vitro* conditions [45, 63]. In the presence of F-BAR domains, membrane tubulation occurs less in comparison with N-BAR and also generates tubes that are larger in diameter [67–70].

I-BAR domains sense and induce negative curvature on the membrane [71]. These domains cooperate with various components of the actin filament assembly and other proteins to promote filopodia protrusion [72–74]. Figure 3.3 presents a model of the stages of filopodia formation and illustrates the functions of key proteins [75].

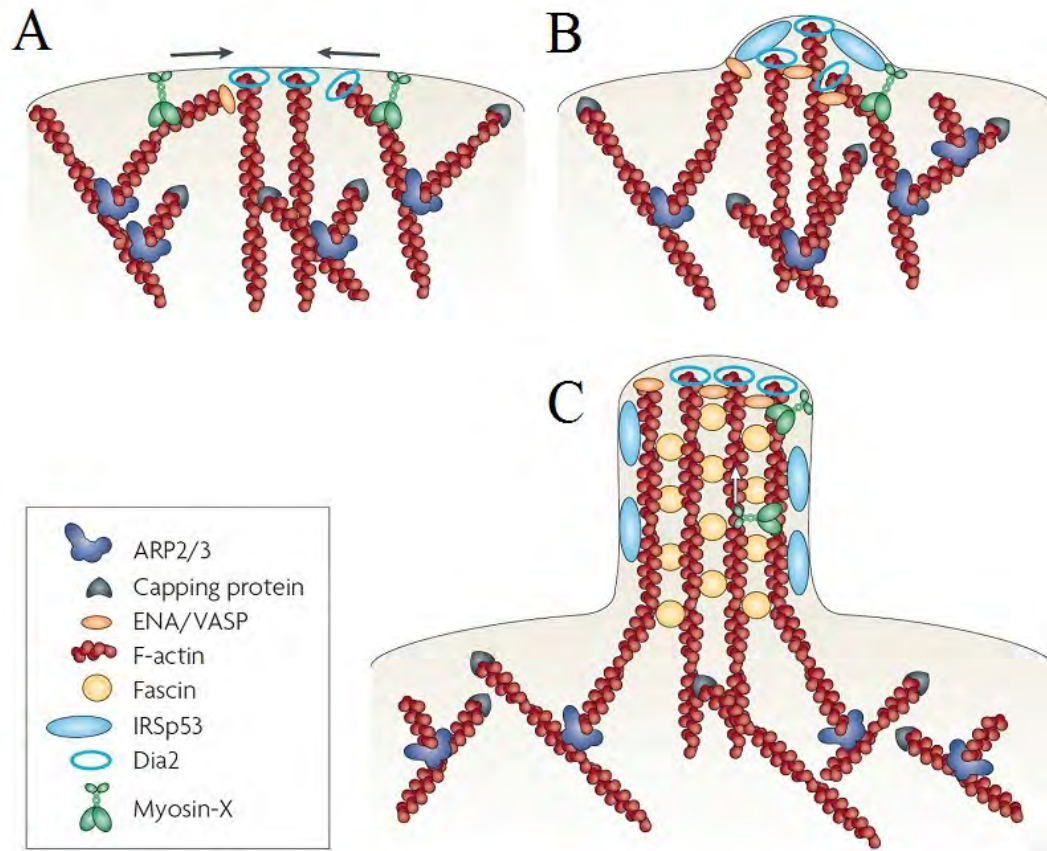


FIGURE 3.3: A model for a filopodia formation [75]; A) The ends of the elongating actin filaments converge, leading to the initiation of a filopodium. B) When the preliminary filopodium begins to push the membrane, the IRSp53 (or other inverse I-BAR domain proteins) facilitate membrane protrusion by directly deforming or tubulating the membrane. C) A filopodium with key proteins.

Chapter 4

The production of spontaneous phospholipid nanotubes and the study of their physical properties

Section ?? included an explanation about lipid nanotubes and their importance in biological systems. In this chapter, we will demonstrate how to create phospholipid nanotubes and tubular vesicles, and then consider their properties such as their rigidity, persistence length, radius, and stability. The stiffness and radius of phospholipid nanotubes will be used to determine how BAR domain proteins bind to different curvatures. Thus, this investigation leads to an understanding of mechanical properties and the molecular details of BAR domains. By comparing the stiffness of protein coated tubes (e.g. F-BAR) to the bare membrane tubes, more information can be obtained regarding the proteins' organization on membranes. The investigation concerning the binding of BAR domain proteins will be discussed in the next chapter.

4.1 One-end-free phospholipid tubes

In the electroformation method to produce vesicles, phospholipid nanotubes are usually created between the vesicles and the surface of the chamber. When one delivers the vesicles' solution from electroformation chamber to a microscopic chamber, some of the nanotubes remain preserved. These nanotubes are very thin; one end is free and other is attached to a vesicle. Nanotubes are unstable; they slowly shrink and their radius increases, while their length decreases. Thin tubes have a high curvature and according to equations 2.5 and 2.6, converting a thin tube to a spherical vesicle leads to a decrease in the bending energy, which is favorable energetically. Gradually the thin tube converts to a small attached vesicle to the main large vesicle and finally fuses onto the membrane (Figure 4.1 A) [76]. The optimized and appropriate method to create lipid tubes is through the swelling of the dried lipid reservoir on a surface by using the force of the fluid flow (Figure 4.1 B). The diameter of tubes and their multilamellarity depend on chamber preparation and flow speed [43, 77]. This method has normally been used to produce tubular vesicles which have a diameter of about 1-5 μm). Tubular vesicles have been studied with consideration for Rayleigh-Plateau instability, also called pearling instability [43, 78, 79]. In pearling instability, tubular vesicles under tension can convert to connected quasi-spherical bulbs (Figure 4.1 C, D).

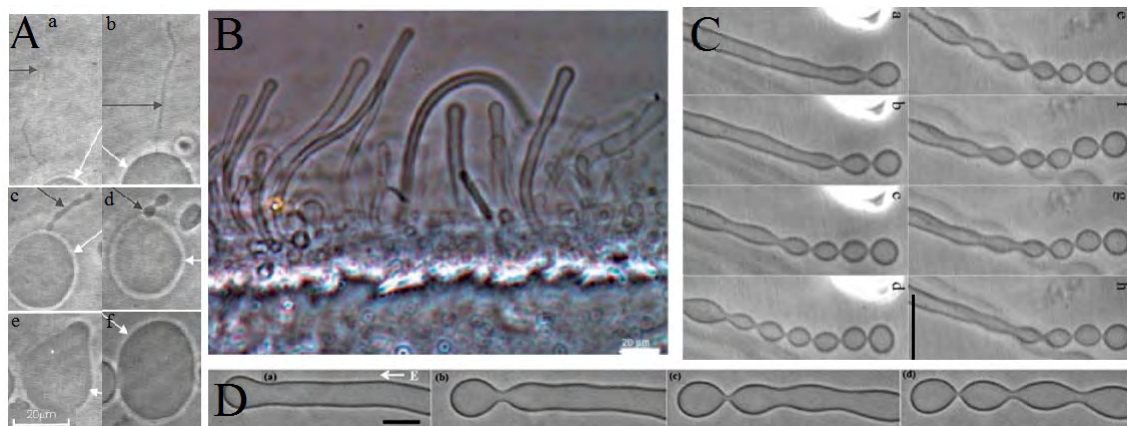


FIGURE 4.1: Phospholipid tubes with one free end. A) Phospholipid nanotubes after vesicle preparation which are unstable and shrink to the membrane [76]. B) Phospholipid microtubes have been produced by the fluid flow method [43]. C) Pearling of microtubes by an amphipathic anchoring polymer, which was injected around the vesicle using a micropipette [79]. D) Pearling instability on microtubes by applying an electric field [43]. Scale is 10 μm .

4.2 Spontaneous free end phospholipid nanotubes

Making free end phospholipid nanotubes and studying their stability is useful to extract the mechanical property of the membrane bilayer by using thermal fluctuation. As it was mentioned in section 2.6, nanotubes are energetically unstable. However, their period of stability can be increased by the manipulation of the lipid mixture, the shape of the chamber where the nanotubes are placed, and with a medium solution. Recently in an experiment, a long tether was extracted from a vesicle membrane and was then separated from the vesicle membrane by mechanical manipulations [49]. Consequently, by this method, a free end nanotube was created and its stability was studied (Figure 4.2).

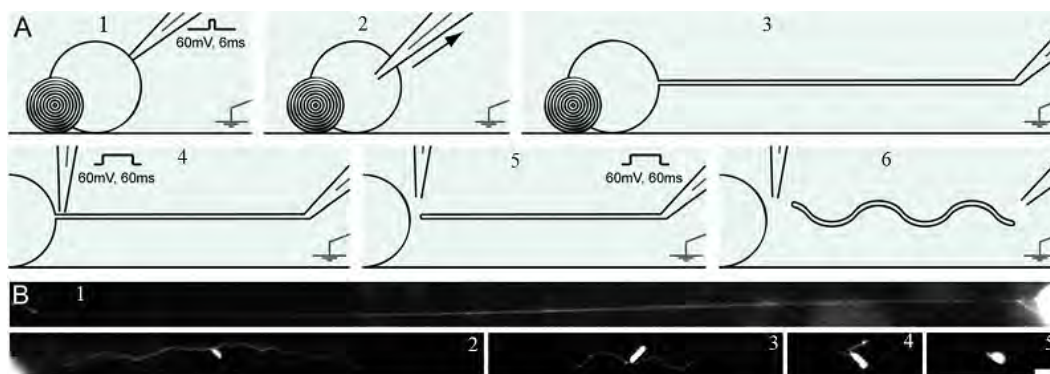


FIGURE 4.2: A) Schematic of pulling a nanotube from the membrane and cutting the attached point from the membrane (making a free end nanotube). B) A long phospholipid nanotube (length $300 \mu\text{m}$) after being released from the membrane shrinks and evolves into an elongated vesicle [49].

Recently a simple swelling method for making spontaneous free ends phospholipid nanotubes has been presented [48], which we also utilized. In our method, a phospholipid stock solution was made from POPC and TR-DHPE (98:2 mol%) in a concentration of 10 gL^{-1} in chloroform. TR is a fluorescent dye with an excitation maximum of 590 nm and an emission of 615 nm. $50 \mu\text{L}$ of this solution was dried out at the bottom of a glass vial to form a lipid film. Subsequently, the lipid film was hydrated with $300 \mu\text{L}$ of milli-Q water at room temperature for 5 hours. Finally, $1 \mu\text{L}$ from the solution was sandwiched between a cleaned coverslip and a microscope slide which had already been coated with an α - Casein solution (2 mg/mL). This was in order to prevent the adhesion of the phospholipid nanotubes to the glass surface. The chamber was sealed-off with vacuum grease to prevent the sample from drying. As it has been shown in Figure 4.3 A, there are high concentration phospholipid nanotubes in the chamber, which makes distinguishing free end nanotubes difficult. Another chamber was made from a solution diluted 100 times to facilitate tracking and imaging individual free end phospholipid

nanotubes. Figure 4.3 B shows six consecutive images of a free ends phospholipid nanotube. Phospholipid nanotubes were illuminated by an Hg lamp and the fluorescence images were obtained by an EMCCD (Electron Multiplying Charge Coupled Device) camera.

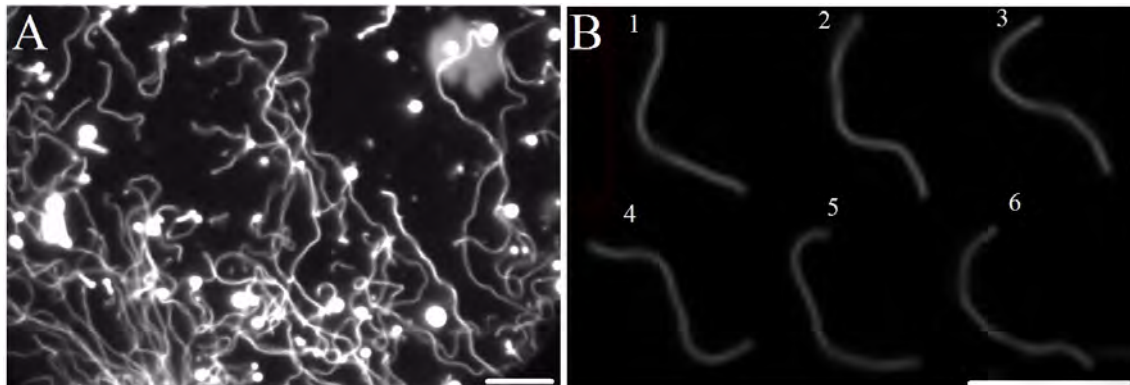


FIGURE 4.3: A) The phospholipid nanotubes' image of fluorescence microscopy (Hg lamp). B) Six consecutive images of a free end phospholipid nanotube, which show the fluctuation of it. Each snapshot is separated by 5 s. Scale is 10 μm .

4.3 Quantification of the radius and lamellarity of phospholipid nanotubes by their persistence length

The flexibility and rigidity of filaments can be identified by their persistence length. As a physical definition, the length scale beyond which the filament shows significant curvature due to thermal forces, is known as the persistence length, L_p [80]. The thermal bending of filaments can be discussed in terms of the three-dimensional persistence length, $L_p = \frac{EI}{kT}$ (E and I are Young's modulus and the geometrical moment of inertia of the cross-section of filament respectively) [81]. Informally, a filament that has a length much shorter than the persistence length, behaves like a rigid rod. However, if the length is equal to the persistence length, it becomes a semi flexible elastic rod, whereas if the filament has a much longer length than the persistence length, it is completely flexible and the properties can only be described statistically, such as a random walk (Figure 4.4).

The persistence length of biological polymers depends on their composition as well as their geometrical properties. For example, DNA has a persistence length of about 50 nm [82], actin filament has a persistence length of 17 μm [80] and microtubules are more stiff, with a persistence length of millimeters [81].

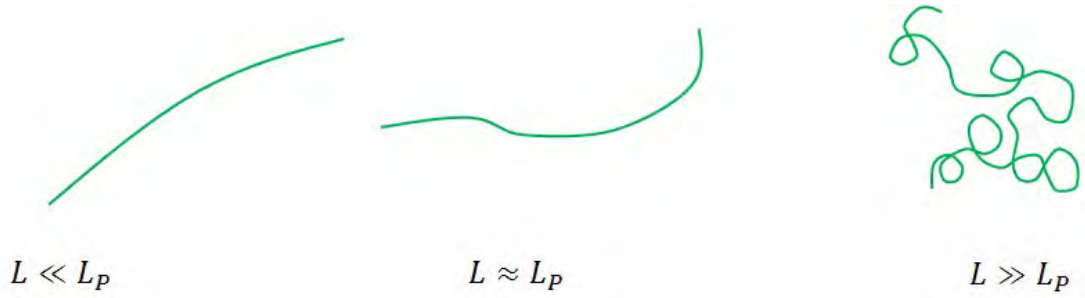


FIGURE 4.4: A schematic of three filaments with a length smaller ($L \ll L_p$), equal ($L \approx L_p$) and bigger ($L \gg L_p$) than its persistence length.

There are several different methods to measure the persistence length of a filament[83, 84]. To find the persistence length of phospholipid nanotubes, the Cosine Correlation Function (CCF) method was used. In the first step of this method, the consecutive images of a filament under thermal fluctuation have been taken. In each snapshot, the skeleton of the filament is extracted and divided into many vectors whose size should be smaller than the persistence length, such as in tangent vectors. The persistence length of the nanotube is related to the correlation of the tangent vectors [85, 86]:

$$\langle t(s) \cdot t(s+x) \rangle = \exp\left(\frac{-x}{2L_p}\right) \quad (4.1)$$

where $t(s)$ is a tangent vector in initial position s and x is the distance of the tangent vector $t(s+x)$ from point s (Figure 4.6 E). In Appendix A, it is shown that how this equation can be obtained.

4.3.1 Phospholipid nanotubes' imaging

The Leica confocal microscopy with a water immersion objective (Leica HCX, PL APO, 63, NA = 1.2 Water Corr CS) was used to capture images of nanotubes. The intensity of phospholipid nanotubes was measured from confocal images due to their superior axial resolution ($0.5 \mu m$) in comparison to images which have been taken by an EMCCD camera. The average intensity on several images of an attended tube was measured focusing on the part of tube with maximum intensity (see Figure 4.8A). The fluorescent consecutive images of nanotubes (less blurry than confocal images) were recorded by EMCCD camera and the images were used to determine the nanotubes' persistence length. Figure 4.7A shows the difference of intensity of the two phospholipid nanotubes with either confocal or fluorescent images, shown in Figure 4.5B.

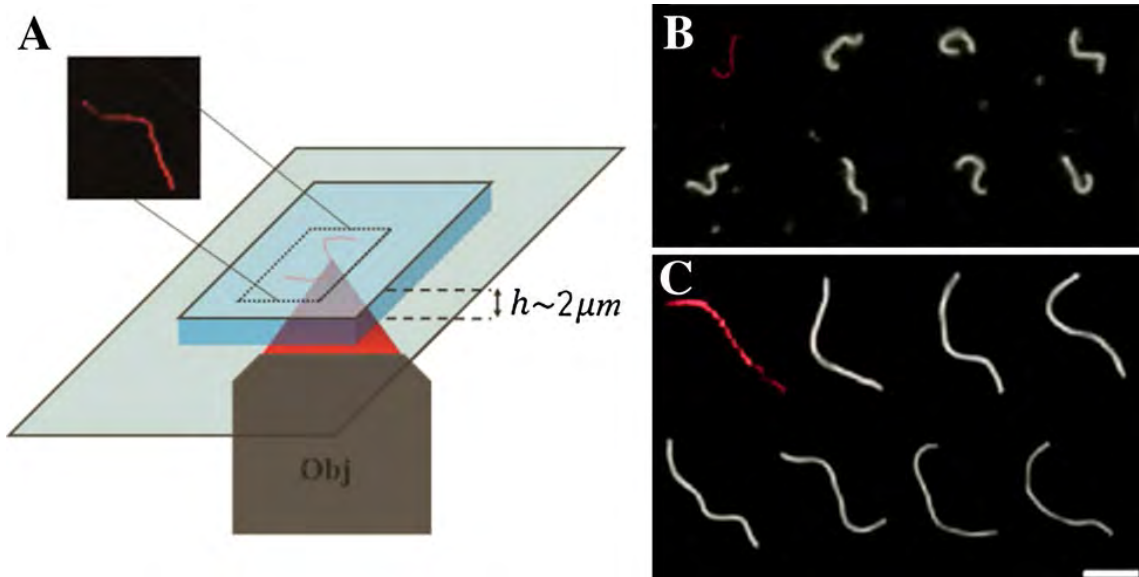


FIGURE 4.5: A) An illustration of our semi 2 dimensional chamber and a confocal image of a typical phospholipid nanotube. B, C) Consecutive images of two phospholipid nanotubes which have different intensities. Images with white signal of nanotubes were captured under Hg lamp by an EMCCD camera. The first images show confocal images; the value of intensity was measured from the red TR-DHPE signal. The scale bar is $5 \mu m$.

4.3.2 The tangent vectors on a phospholipid nanotube

We made a two dimensional chamber (section 4.2) to capture snapshots of the entire length of the phospholipid nanotube. The thickness of several chambers (the distance between two slides) was measured by using the reflection of the laser from glass-water interfaces [87] and the thickness about $2 \pm 0.5 \mu m$ was calculated. The thickness between slides can also be estimated. If a drop with $1 \mu l$ size is spread between slides $2 \times 2 cm^2$ due to capillarity force, the distance between them should be approximately $2.5 \mu m$. Figure 4.5 A shows a schematic of our semi 2D chamber.

The chamber was placed on the stage of microscope and a desired phospholipid nanotube was found under confocal scanning (SP5, Leica) and several images of it were captured for the intensity measurement. The intensity was used for measuring the radius of the tube (explained in the next section in more detail). In second the step hundreds of consecutive images of the same tube were taken under fluorescent illumination (Hg lamp) using an EMCCD camera. The EMCCD images were used to find the persistence length of the tube. To find the persistence length of a nanotube by using eq. 4.1, the skeleton of the nanotube has to be located in each frame and divided into tangent vectors. We developed a MATLAB program to track nanotube skeletons and to digitize them to tangent vectors. Our method was inspired by the digitization method of Ott et al(1993)[86]. First, all consecutive images of the nanotube are loaded in the program

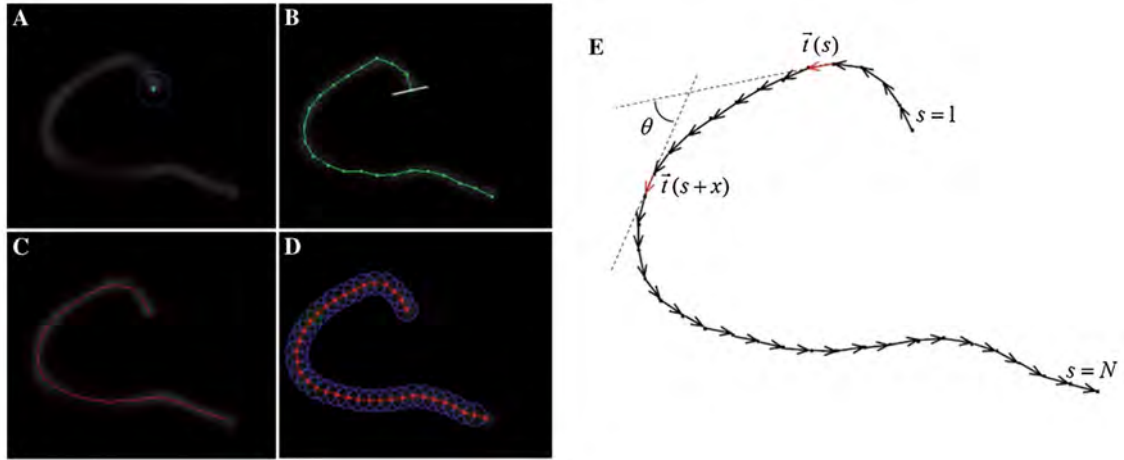


FIGURE 4.6: Procedure to track and find tangent vectors along nanotubes. A) The starting point of the nanotube is determined by a click on one end. There is a circle around this point which is used to find the second point. B) The second point along the nanotube is found by looking at the highest intensity on the circle. This procedure is repeated to find other points which are connected with a green line. C) By tracking the Gaussian profiles' intensity along the green line on the nanotube, the skeleton was revealed with a sub-pixel resolution. D) The nanotube is divided into the digitized points. E) Tangent vectors on the nanotube

and, in each frame, the starting point of the nanotube is determined by a click on one end of the nanotube. Hence, the program works as follows:

A) A circle with a radius of several pixels (length about $0.8 \mu m$) is drawn around the start position. The radius of the circle is smaller than the persistence length of the nanotube. However how can the persistence length be judged before measuring it? The answer is that the exact value of the persistence length can not be estimate by looking the image, but we can see along the selected radius; the tube is almost straight, so the radius of circle is smaller than the persistence length of the nanotube (Figure 4.6 A).

B) The radius of the circle (radius line) scans the entire circle area and the program measures average intensity along with the radius line. Hence, the highest intensity determines the orientation of the nanotube and the end of the radius line on the arc is the second point along the nanotube. This procedure is done for second point in order to locate the third point and it is repeated to find remaining points. Figure 4.6 shows digitized points found by this method which are connected by a green line.

C) The green line in step B is the crude skeleton of the nanotube; it is used to find the skeleton which has the optimal spatial resolution. The program uses a perpendicular line to the green line in order to measure the intensity profile of the nanotube and then fits a Gaussian profile to this intensity to define center position of intensity. The red line in Figure 4.6 C shows the line of the skeleton as a result of this step.

D) The program uses the circles with predefined radii to digitize points along the skeleton of the nanotube. As Figure 4.6 D and E show, the intersection points of the circles with

the skeleton determine tangent vectors along the nanotube.

By using this algorithm, it is not necessary to use the binary format of the image to track the nanotube and the original data is not lost.

About 150-200 consecutive images of the nanotube were used to calculate the persistence length of the nanotube by using eq. 4.1. The logarithm of the tangent correlation function versus the distance of tangent vectors, x , (eq. 4.1) of the two tubes with different intensities (Figure 4.7 A) shown in Figure 4.7 B. Solid lines show the fit of eq. 4.1 on the experimental data; the persistence length of tubes is extracted from the slope of the fit. Tube 1 and 2 with low and high intensities have the persistence length of (2.36 ± 0.08) and $(8.32 \pm 0.07) \mu m$, respectively.

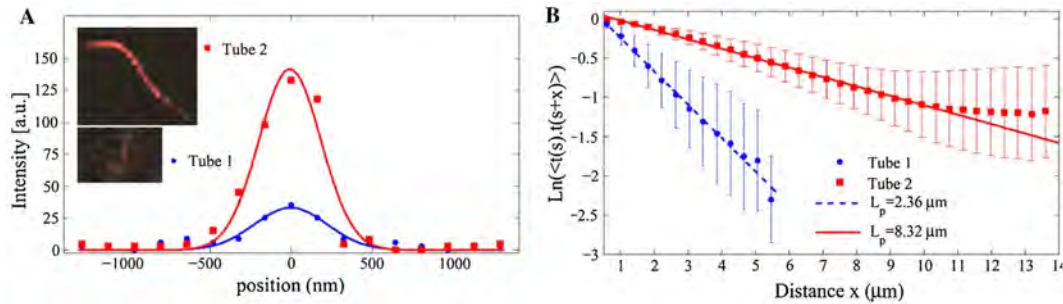


FIGURE 4.7: A) Intensity profile of two phospholipid nanotubes. B) Cosine correlation function diagram as a function of separation, x , along the arc. Tube 2 with high intensity has a significantly larger persistence length compared to tube 1.

There are two reasons why tubes have a difference of intensity level. firstly, their radius is different and, secondly, they might have a difference of lamellarity. If the lamellarity of the tubes is the same, it should be concluded that the tubes having the same intensity also have the same persistence length due to their equal radii. However, in our data, we saw tubes with the same intensity but with significantly different persistence length values. Figure 4.8 shows that tube 2 and 3 have the same intensity ($I = 210$ a.u.) but different persistence lengths due to their different radii and lamellarities.

4.3.3 Phospholipid nanotubes radius

As shown in Figure 4.9 A, the multilamellarity of phospholipid nanotubes begins with a special intensity that depends on the intensity, I_{min} , of the unilamellar nanotube with the smallest radius, r_{min} . A tube with twice the minimum radius ($2r_{min}$) has the intensity of $2I_{min}$. If a second bilayer is added on the unilamellar phospholipid nanotube with the radius and intensity of r_{min} and I_{min} , the radius of the new multilamellar nanotube is $r_{min} + \Delta r$. However, its intensity is $(2 + \Delta r/r_{min})I_{min}$ where $\Delta r \sim 5nm$ is the thickness of the bilayer. It can be concluded that the difference in intensity level of the tubes is

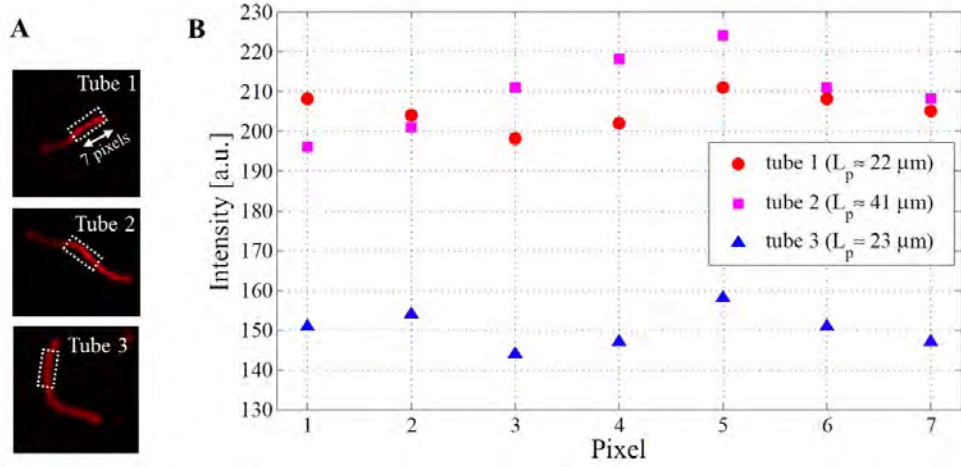


FIGURE 4.8: A) Three typical tubes, the part of the tubes in focus were used to measure intensity. B) The intensity of the tubes versus selected pixels along the tubes' axis. Tube 2 and 3 have the same intensity but different persistence lengths due to multilamellariy.

due to a difference in radius or lamellarity as illustrated schematically in Figure 4.9 B (the bilayer thickness has been ignored). Therefore, we can label each tube a unilamellar tube, which has an intensity between I_{min} to $\sim 2I_{min}$, and the radii of the 1, 2, and 3 bilayer tubes can be labeled r , r_2 , and r_3 . Hence, there is a linear dependence between the radius of the tubes and their intensity as defined by: $r = \alpha I$, $r_2 = 1/2\alpha I$, $r_3 = 1/3\alpha I$ (see Figure 4.9 B), where α is a proportionality constant (notice that this assumption is acceptable for tubes with a diameter smaller than the confocal imaging depth).

The radius of a unilamellar tube, r , can be obtained from the expression [48, 61] (see Appendix A):

$$L_P = \frac{2\kappa\pi r}{k_B T} \quad (4.2)$$

κ and k_B denote the bending rigidity and Boltzmanns constant, respectively. By the substitution of $r = \alpha I$ in this equation, it can be rewritten as:

$$L_P = \frac{2\kappa\pi\alpha I}{k_B T} \quad (4.3)$$

To find the proportionality constant, α , we selected tubes which had the intensity value between I_{min} to $\sim 2I_{min}$ ($I < 70$ a.u.). This area of intensity was called "the unilamellar area". Figure 4.10 shows the diagram of the persistence length of the tubes versus their intensity in the unilamellar area. The solid red line is a fit of eq. 4.3 on the experimental data points (bottom axis) where the value of $\alpha = 0.616$ was extracted from the slope. This value was used to calculate the radius of the phospholipid nanotubes; the results are shown on the top axis of Figure 4.10. Therefore, the minimum radii of the phospholipid nanotubes is approximately $r_{min-ex} \sim 18$ nm. The minimum radius for lipid nanotubes

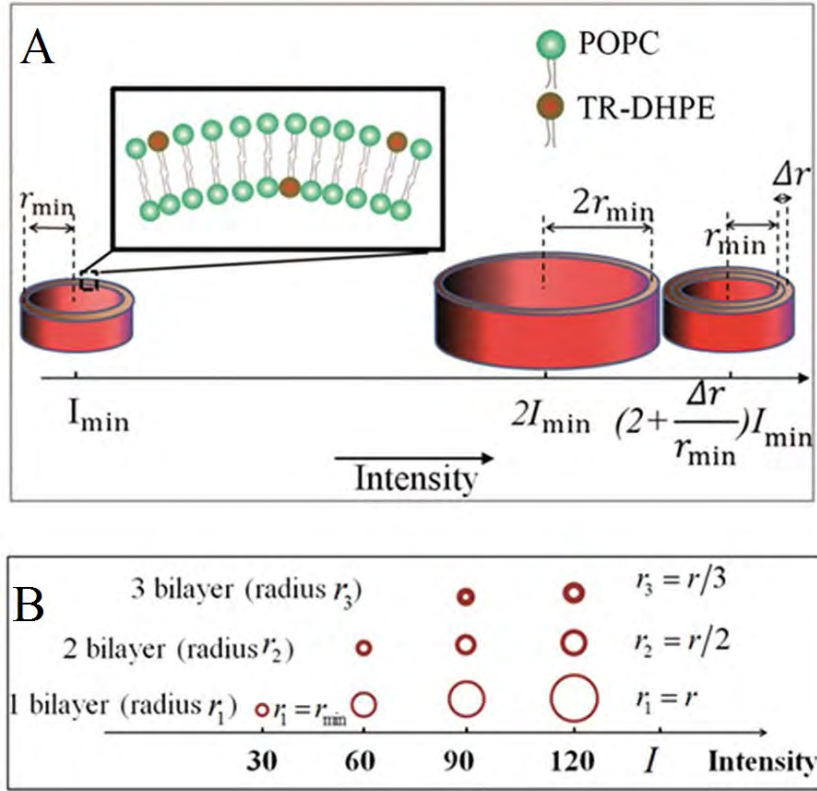


FIGURE 4.9: Illustration of multilamellarity on the phospholipid nanotubes. A) A diagram of three tubes shows if unilamellar phospholipid nanotubes with the smallest radius has an intensity of I_{min} , multilamellarity begins from the intensity above $(2 + \Delta r/r_{min})I_{min}$. B) In the multilamellar area, the scattering of phospholipid nanotubes in the intensity diagram could be due to a difference in radius and lamellarity.

can be estimated theoretically by the balance between the bending energy of a tube and the surface energy. The bending energy of a tube with the length of l and the radius of r is given by $E_{bend} = \kappa\pi l/r$ which is unfavorable to create a tube. The favorable energy to create a tube from a flat membrane is the edge energy $E_{edge} = 2\gamma(2\pi r + l)$, where γ is the edge tension of the lipid bilayer. For a flat membrane with a length far greater than its width ($r \ll l$), the edge energy can be rewritten as $E_{edge} = 2\gamma l$. The minimum radius of the tube is achieved by equating E_{bend} and E_{edge} which gives $r_{min-th} = \pi\kappa(2\gamma)^{-1}$. For POPC phospholipid tubes, the bending rigidity of the membrane and the edge tension are given by $\kappa = 19 k_B T$ [88] and $\gamma = 6 \pm 0.3 pN$ [89], respectively. By the substitution of these values to r_{min-th} , the theoretical minimum radius was found to be $r_{min} \simeq 20.4 nm$. This amount corresponds well with the experimental value (18 nm, see Figure 4.10).

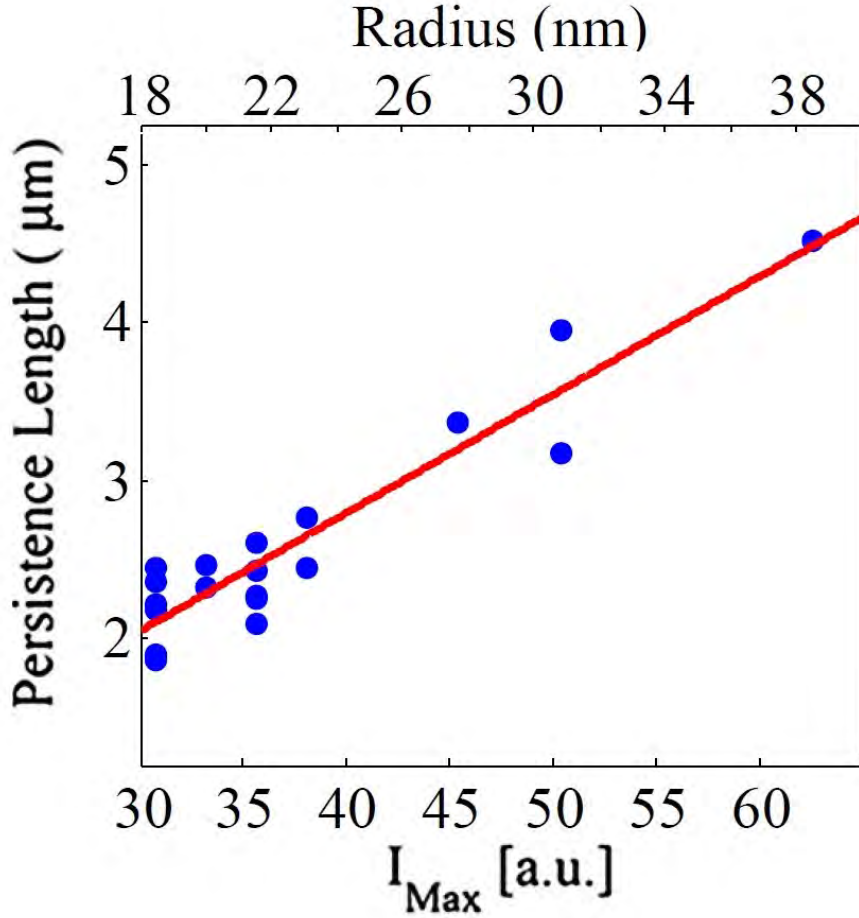


FIGURE 4.10: The persistence length of phospholipid nanotubes versus their intensity for unilamellar area ($I < 70$). The solid red line is the linear fit of equation 4.3 through data points, where the value of $\alpha = 0.616$ was extracted from the slope of the fit, is then used to determine the radius of the nanotubes (top axis).

4.3.4 Multilamellar Phospholipid nanotubes

For tubes with more than one bilayer (multilamellar tubes), the bending rigidity of a lipid membrane is related to the total membrane thickness h , as [59]:

$$\kappa = \frac{k_A h^2}{24} \quad (4.4)$$

k_A is the area compression modulus.

Therefore, if the bending rigidity of the unilamellar tubes is labeled κ , the bending rigidity of 2 and 3 bilayer would be 4κ and 9κ respectively. With the substitution of these expressions into equation 4.2, similar equations can be written for 2 and 3 bilayers'

nanotubes:

$$L_P(2) = \frac{4\kappa\pi\alpha I}{k_B T} \quad (4.5a)$$

$$L_P(3) = \frac{6\kappa\pi\alpha I}{k_B T} \quad (4.5b)$$

Note that in eq. 4.2, $r_2 = 1/2\alpha I$, $r_3 = 1/3\alpha I$ was substituted for 2 and 3 bilayer.

Figure 4.11 shows the diagram of the persistence length versus the tubes' intensity. This diagram shows the persistence length of 64 individual phospholipid nanotubes. The scattering of data (intensity above 70 a.u.) represents the multilamellarity of the nanotubes. Equations 4.3, 4.5a and 4.5b are plotted on this diagram and correspond to uni (red line), double (blue line) and trilamellar (green line) tubes. As can be seen, most tubes are unilamellar (data in red shaded region).

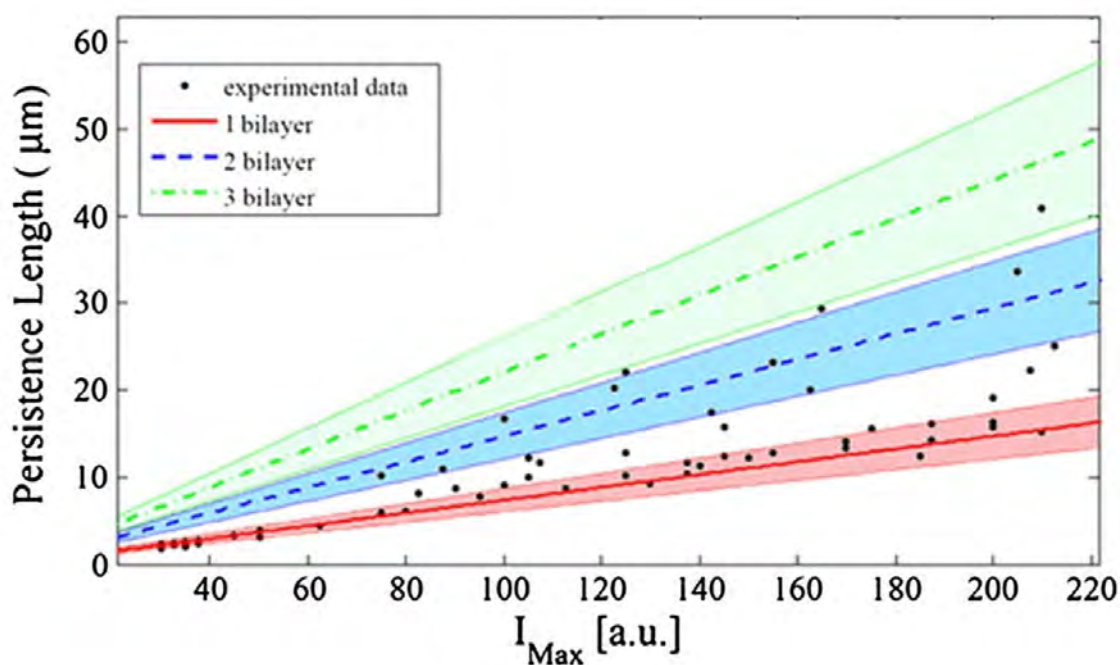


FIGURE 4.11: Diagram of the persistence length of phospholipid nanotube as a function of their intensity. The data below 70 a.u. (x axis) is in the unilamellar area and has been discussed in Figure 4.10. The red, blue, and green lines are the theoretical plots of equations 4.3, 4.5a, and 4.5b correspond to the single, double and trilamellar tubes, respectively. The errors (color shaded regions) were calculated from the unilamellar area in Figure 4.10

4.4 The tubular vesicle

As discussed in sections 2.6 and 4.2, phospholipid nanotubes are unstable and most of them shrink to liposomes or tubular structures. It was discovered that the final shape also depends on the chamber shape which contains tubes. Initially, after a semi-two-dimensional chamber was made, most of the lipid tubes were long with a smaller radius than the resolution limit of the light microscopy (Figure 4.12 A). However, after a while, they began to shrink. Most of the thin tubes, and especially the long tubes, shrunk and converted to tubular vesicles with a measurable radius as could be measured from the intensity profile across the tube on the confocal images (Figure 4.12 B). This observation is similar to the prior experiment [49, 76] as it was explained in section 4.2. As in the three-dimensional chamber, the free end lipid nanotubes finally convert to a spherical shape (stomatocyte membrane). However in our case, phospholipid nanotubes were in two-dimensional chamber and there was not enough space for the tubes to transform to a spherical vesicle. Figure 4.12 C shows an example of two tubes transforming to a small vesicle and a tubular vesicle. The tubular vesicles have a radius approximately between 150 and 600 nm and a contour length between 3 and 30 μm .

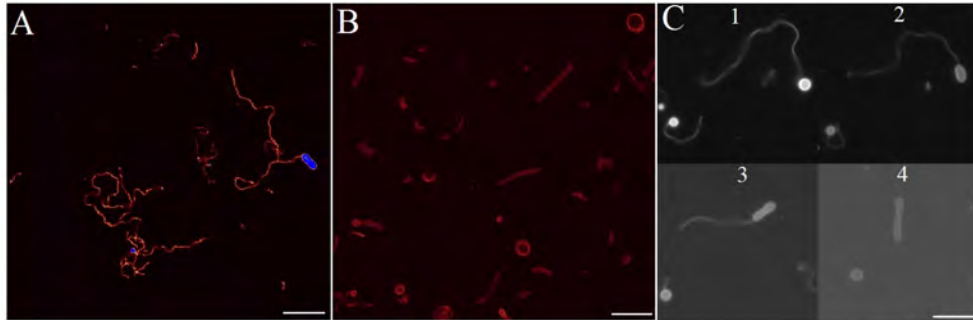


FIGURE 4.12: Transformation of phospholipid nanotubes into tubular vesicles. A) Confocal image of phospholipid nanotubes directly after the 2D chamber was made. B) The sample after 4 hours when nanotubes converted to tubular vesicles C) Consecutive fluorescence images of transformation; it begins from one end of the tubes and takes several minutes to convert to a tubular vesicle or a liposome (small vesicle). Scale bar is 10 μm .

We measured the radius and length of the tubular vesicles and used them to calculate the diameter of vesicles if tubular vesicles converted to spherical vesicles. The radii of the tubular vesicles were calculated by their intensity profiles (Figure 4.13A). The histogram of radius distribution (Figure 4.13A) shows that the radius of the tubular vesicles are distributed around 250 nm. If a tubular vesicle with radius r and length l converts to a spherical vesicle, its diameter would be $D_s = 2\sqrt{rl/2}$. To transform a tubular to a vesicle, D_s should be smaller than the thickness of the chamber. Figure 4.13C shows the histogram of D_s where is distributed around 2 μm . On the other part,

the thickness of the chamber that was measured by laser reflection on the water-glass surface was approximately $2 \mu\text{m}$. Hence there is not enough space for most of the tubulars to convert to vesicles.

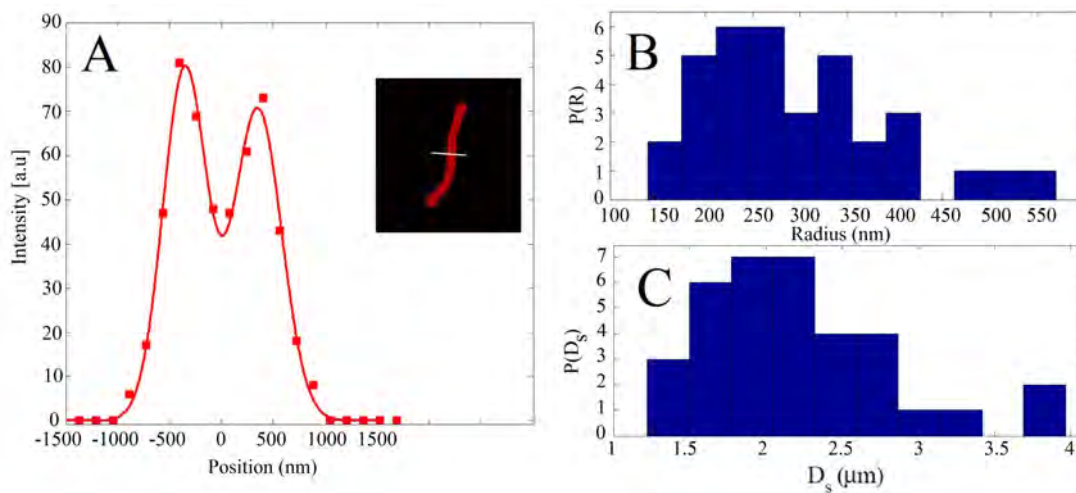


FIGURE 4.13: A) Intensity profile across a typical tubular vesicle. B) Radius distribution of tubular vesicles. C) Histogram of vesicles' radius' if the tubular vesicles could transform to the spherical vesicles.

4.5 The effect of fluorescent illumination on tube stiffness

The effect of fluorescent illumination (Hg lamp) on phospholipid nanotubes and tubular vesicles was quantified by measuring their persistence length during a long period of exposure. The persistence length of several phospholipid nanotubes and tubular vesicles was measured by 40 second sequential steps during a 5- minute illumination (Figure 4.14 B). The results demonstrate that the persistence length of phospholipid nanotubes is constant during illumination (blue circle points in Figure 4.14 B). Interesting result was about tubular vesicles that the persistence length descended significantly during illumination time (red square points in Figure 4.14 B).

Figure 4.15 shows that the counter length of the tubular vesicles increases during illumination time. Tubes elongated approximately 12%, so then by assuming that the area was constant during elongation, means that their radius contracted about 10%. The persistence length of the tube has a linear dependence to its radius, so in this case, the elongation should change persistence length about 10%; however, Figure 4.15 shows that the decrease of the persistence length of tubes is about 50%. Therefore, the large value of decrease in the persistence length of the tubular vesicles cannot just be explained by the effect of tube elongation. We expected a change in lipid material during illumination according to previous observations, in which the bilayer tension increases in strong

illumination [90]. There was no change in the persistence length of the phospholipid nanotubes during illumination time. As already discussed, phospholipid nanotubes have a radius from 18 to 100 nm and tubular vesicles have larger radii. Hence, phospholipid nanotubes have a very high curvature compared to tubular vesicles. Also, the radial shrinking of a phospholipid nanotube needs an energy to alter the bending energy. This is probably the main reason that explains the constant persistence length of phospholipid nanotubes during illumination time.

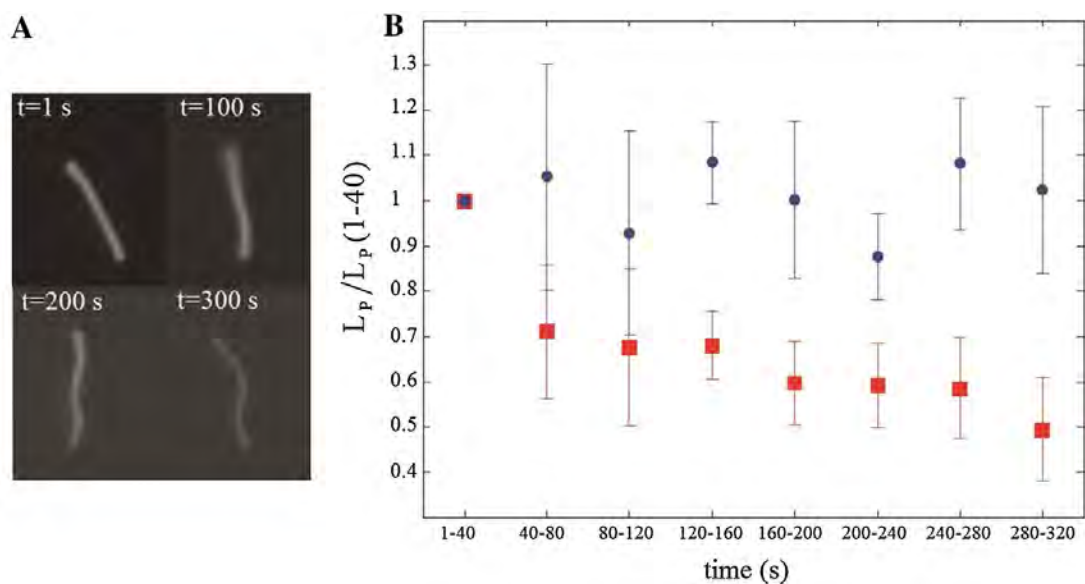


FIGURE 4.14: Effect of Hg lamp illumination on the persistence length of phospholipid tubes. A) Consecutive EMCCD images of a typical tubular vesicle which show that during illumination the tube becomes more flexible. The intensity of the tube decreased during time due to bleaching. B) The normalized persistence length of phospholipid nanotubes (red squares) and tubular vesicles (blue circles) as a function of illumination time. The standard deviation is due to the measurement of the persistence length of 7 phospholipid nanotubes and 7 tubular vesicles.

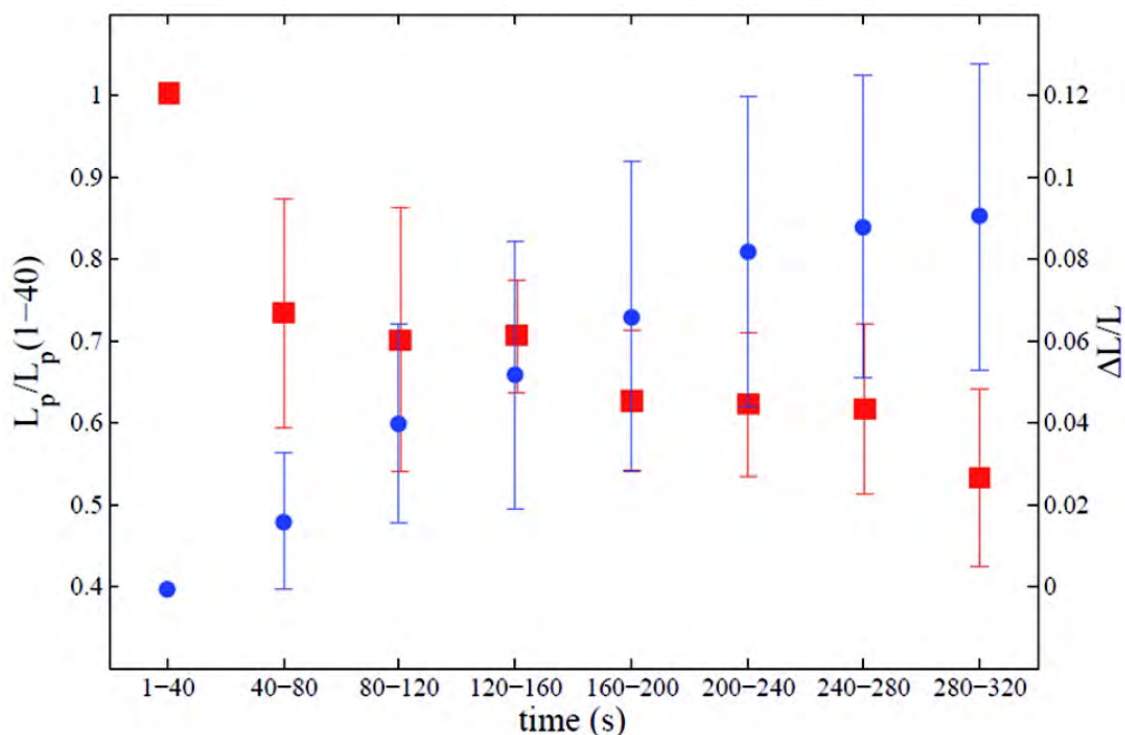


FIGURE 4.15: Normalized persistence length of tubular vesicles versus illumination time (red square, left axis). Right axis shows the relative change of the counter length of tubular vesicles (blue points).

4.6 Conclusions

In this chapter, a novel method was introduced to identify spontaneous phospholipid nanotubes on the basis of their persistence length and intensity under confocal microscopy. The radius of nanotubes was found approximately 18-100 nm. It was also discovered that nanotubes with a lowest intensity (related to the persistence length) are unilamellar, while nanotubes with a higher intensity than the twice of the smallest one can be uni- or multilamellar. The radius of nanotubes and their multilamellarity can be considered in the study of the membrane associated proteins binding to high curved tubes.

In two dimensional chamber, long phospholipid nanotubes convert to tubular vesicles with a measurable radius from optical microscopic images. It was discovered that long time illumination of Hg lamp decreases the persistence length of tubular vesicles whereas the persistence length of phospholipid nanotubes is constant during illumination. These results are useful and the effect of illumination on membranes during data collecting under emission of the Hg lamp should be noted.

Chapter 5

Curvature-sensing of BAR domain proteins and tubulation of membranes by them

BAR domain family proteins were briefly explained in chapter 3. These domains have a spontaneous curvature which leads to membrane curvature sensing and the BAR domain and its helices can facilitate stabilization electrostatic binding to membranes or insertion of amphiphatic helices into a membrane. The effect of three BAR domains on membranes was investigated: F-BAR (Syndapin 1), Arfaptin (classic BAR) and I-BAR (ABBA type) domains on the membrane and phospholipid nanotubes, which will be discussed in this chapter.

First, I will describe how F-BAR syndapin 1 senses the various curvatures on a pulled tether from a vesicle. The persistence length and the stiffness of the F-BAR coated spontaneous tubes will be discussed. Subsequently, in second section, our investigation and observation of the tubulation activity of vesicle membranes due to the binding of Arfaptin-membrane will be explained. Finally, in the last section, The I-BAR effect on the membrane will be discussed. The tubulation activity of the I-BAR is tested with respect to concentration and tension. These results are important for understanding their mechanism in cellular remodeling e.g. tension is suggested to be a master regulator in controlling filopodia formation, endocytosis etc.

5.1 The effect of F-BAR on phospholipid nanotubes

Syndapin 1 F-BAR is a member of the F-BAR domain proteins' subfamily. As shown in Figure 3.1, the F-BAR domain has three members: FCHo, FBP17 and Syndapin. F-BAR domain proteins sense or induce curvature on a membrane and these proteins bind to membranes in biological processes to remodel membranes at endocytic pathways and filopodium formation in association with actin filaments. Unlike FCHo and FBP17, Syndapin contains two wedge loops that can cause tubulation of membranes by inserting them into the leaflet of membranes.

In this section, the curvature sensitivity of the F-BAR will be shown on different curved membranes, which were produced by pulling a tether from the lipid vesicles. The results show that the F-BAR senses highly curved membranes at low density. We also show that the F-BAR binding on the spontaneous phospholipid nanotubes significantly increases their persistence length.

5.1.1 F-BAR senses curvature on a tether pulled by optical tweezers

Two kinds of GUVs were made by the electroformation method: Synthetic lipid vesicles from DOPC, DOPG, DSPE-PEG(2000) Biotin, and Texas Red DHPE(74:25:0.7:0.3 molar ratio), and other GUVs were made from brain lipid vesicles (see preparation method in appendix C) in 300 mM Sucrose. The chamber of the micropipette-optical tweezers assay (appendix C) was made by GUVs in 15 mM NaCl, 270 mM Sucrose incubated with an attended concentration of the F-BAR and streptavidin coated beads (diameter=4.95 μm). The prepared chamber was placed on the stage of the confocal microscope, a filled micropipette with 15 mM NaCl, 270 mM Sucrose was gently input close to a vesicle and, by using a micropipette aspiration assay, a part of the vesicle was aspirated into the pipette. By using optical tweezers, a membrane nanotube (tether) was pulled out of the vesicle (Figure 5.2 A). The membrane tension can be controlled by the suction pressure (eq. 2.7), and concerning eq. 2.12b, the tether radius depends on the magnitude of the membrane tension. The micropipette aspiration equations (2.7 and 2.12b) are not reliable for F-BAR coated membranes. Therefore, before the main experiments in the presence of F-BAR, the tether radius was calibrated by intensity techniques; so then the radii of each tube can be measured by using its intensity. The tube/GUV intensity ratio was measured at various suction pressures and the tube radius was measured using eq. 2.12b (Figure 5.1). This ratio was used to estimate the radius of the tubes in all experiments in the presence of F-BAR.

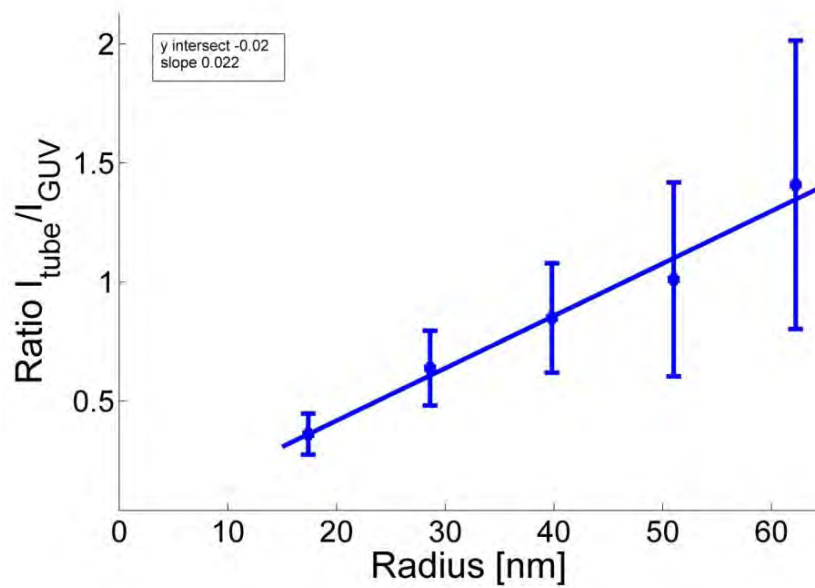


FIGURE 5.1: The tube/GUV intensity ratio versus tube radius. 8 vesicles were used to collect data.

We observed that F-BAR strongly prefers to bind to the tether with small radii (high curvature). Figure 5.2 B shows the signals of TR-DHPE (red) and the F-BAR proteins (white) on the membrane. These signals have been shown in Figure 5.2 C,D as surface plots.

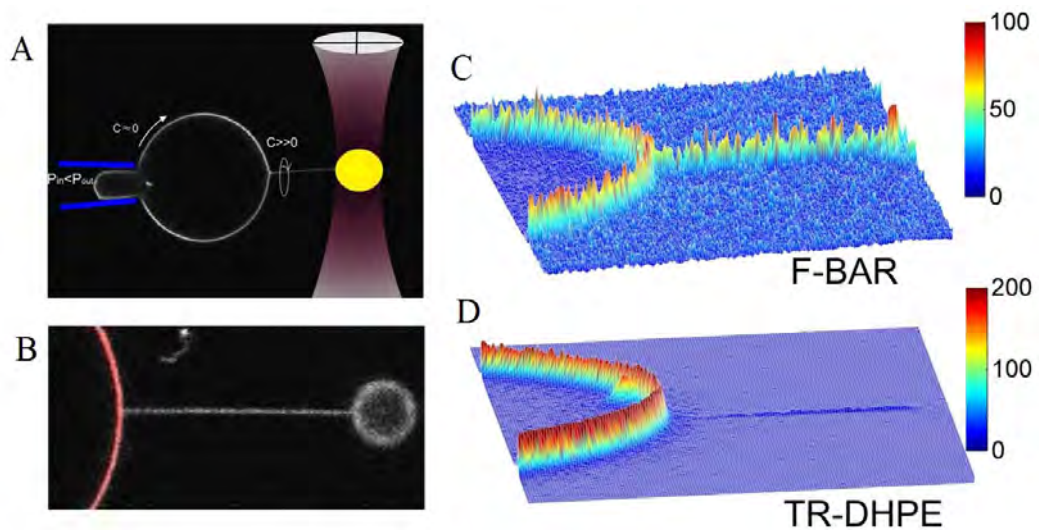


FIGURE 5.2: A) Micropipette-optical tweezers assay which is used to make high curved membrane (tether). B) The confocal microscopy image of the the F-BAR coated membrane with a tether that shows the merged image of two signals: the membrane channel (red) and the F-BAR channel (white). (C and D) surface plots of two signals correspond to (B).

5.1.2 Curvature sensitivity of F-BAR on tethers with different diameters

In the presence of an attendant concentration of the F-BAR, a typical GUV was lightly aspirated into the micropipette and a tether was extracted by moving the chamber using a piezo-electric stage. The radius of the tether (or equivalently tube curvature) was changed using gentle manipulation of the aspiration pressure (see equation 2.7). The tube diameter at various aspiration pressures was measured using a calibrated intensity ratio (see Figure 5.1). To quantify the curvature sensitivity of the F-BAR on the tether, the intensity of proteins on the tube and the GUV (which correspond to the proteins' density) were measured as well as the intensity of the lipid dye. These intensity values were substituted in the defined sorting parameter:

$$\text{Sorting} = \frac{1}{PCF} \frac{(I_{\text{protein}}/I_{\text{membrane}})_{\text{tube}}}{(I_{\text{protein}}/I_{\text{membrane}})_{\text{GUV}}} \quad (5.1)$$

where PCF is a factor which arises due to the polarization direction of the scanning laser [91].

Figure 5.3A shows the sorting parameter for the Synthetic lipid vesicles (DOPC: DOPG 74:25 mol%) as a function of the tubes' radius'. This diagram clearly shows a strong preference of the F-BAR for high membrane curvature (thin tubes). The sorting parameter also has a strong dependence on the concentration of the F-BAR. Sorting was measured in two concentrations of the F-BAR. In a low concentration, 50 nM of the F-BAR (indicated as blue points in Figure 5.3A), it is significantly higher than a high concentration, 500 nM of the F-BAR (indicated as red points Figure 5.3A). The Crowd of proteins on the membrane minimized sensing at high density. The sorting parameter was also measured for brain lipid vesicles in low and high concentration of the F-BAR (Figure 5.3B).

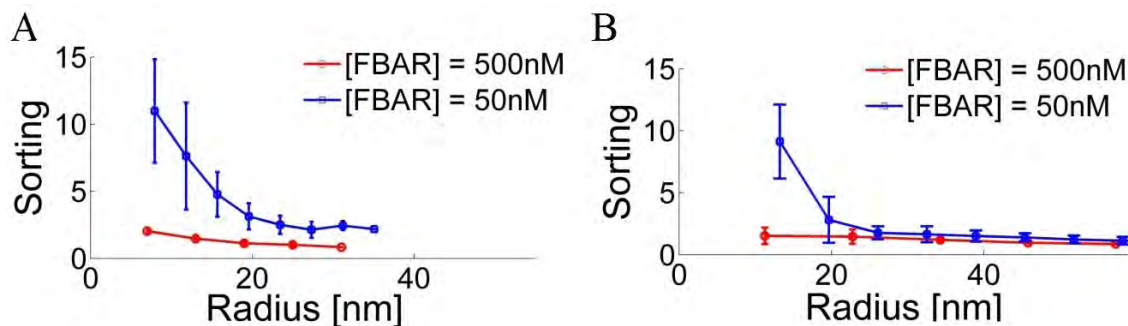


FIGURE 5.3: Sorting of the F-BAR on tubes with different radii' and in different concentrations. The Sorting versus the tube radius for DOPC:DOPG vesicles (A) and brain lipid vesicles (B) in different protein concentration, 50 nM (blue squares) and 500 nM (red circles). 17 GUVs were used to collect the sorting data.

5.1.3 Investigation of the stability of a F-BAR coated tether by optical tweezers

The stability of a F-BAR coated tether was investigated by measuring the tether force. The tether in different concentrations of the F-BAR syndapin 1 elongated (from initial length $5 \mu\text{m}$ to final length $15 \mu\text{m}$) by the quick elongation of the tether ($10 \mu\text{m/s}$). The optical trap was calibrated by monitoring the position of the bead in the trap at 22 kHz using a quadrant photodiode. The power spectrum analysis of the bead's Brownian motion was used to find the spring constant k of the trap (see appendix A). Hence, during experimentation, the tether force was obtained by measuring the displacement of the bead, Δx , from the center of the trap, $F=k\Delta x$.

The experiment was done in various concentrations of F-BAR (0 nM, 50 nM or 500 nM). Figure 5.4A presents a diagram of the force changes (ΔF) versus; during elongation, the tether force increases; see data in 20-21 s in time axis. After elongation, the force decreases to its equilibrium value (time>21 s). The relaxation behavior was measured in three bulk concentrations of the F-BAR, 0 nM (blue), 50 nM (red) and 500 nM (magenta). As seen in Figure 5.4B, the exponential relaxation time increases linearly with the F-BAR concentration: $\tau_{0\text{nM}} = 0.52 \pm 0.01$, $\tau_{50\text{nM}} = 1.20 \pm 0.02$ and $\tau_{500\text{nM}} = 1.71 \pm 0.01$. In the absent of the F-BAR (bare membranes) the relaxation occurs quickly, $\tau_{0\text{nM}} = 0.52\text{s}$, which corresponds with previous observations [92]. In the presence of the F-BAR, relaxation time may increase due to the reorganization of proteins on the membrane.

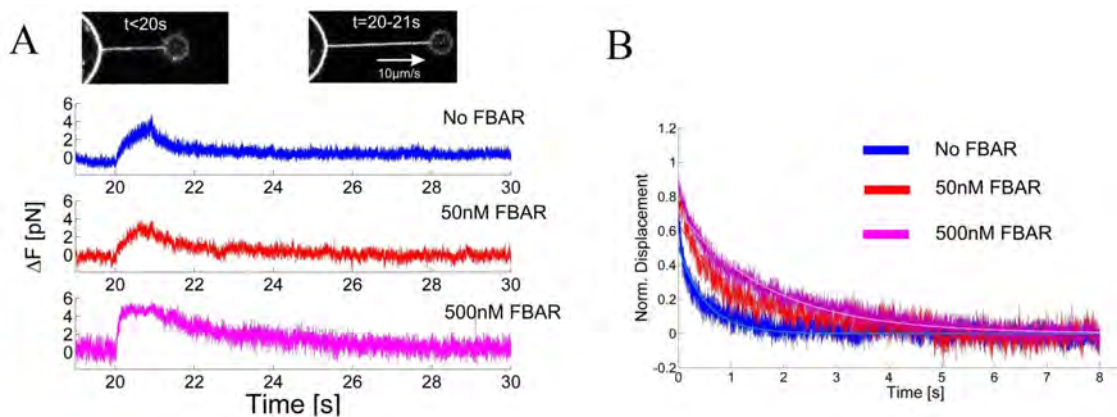


FIGURE 5.4: Relaxation behavior of the tether force after tether length was elongated $10 \mu\text{m}$; A) The tether force behavior versus time during time of elongation ($20 < \text{time} < 21$) and relaxation ($\text{time} > 21$); see inset images. The experiment was done at three concentrations of the F-BAR, 500 nM (magenta), 50 nM (red) and no F-BAR (blue). B) The summarized result of several experiments (8 for 500 nM F-BAR and 6 for both 0 and 50 nM F-BAR) during relaxation time.

5.1.4 The persistence length of F-BAR coated phospholipid nanotubes

The process of creating free end phospholipid nanotubes was explained in chapter 4 as well as the CCF method to calculate their persistence length. Here, the persistence length and the rigidity of the F-BAR coated free-end phospholipid nanotubes was calculated. F-BAR proteins bind to a membrane and form a lattice like structure on its surface [46]; it was expected that this structure would change the rigidity of the membrane. We investigated the persistence length of spontaneous phospholipid nanotubes in the presence of a high concentration of F-BAR syndapin 1 ($3 \mu\text{m}$) and finally the results were compared with the persistence length of bare nanotubes.

Phospholipid nanotubes were created by the swelling method (section 4.2) from POPC: DOPG: TR-DHPE (73:25:2 mol%). In the first step, a semi 2D chamber was made in the absence of the F-BAR to measure the persistence length of the nanotubes (in the unilamellar area, see section 4.3.3 in chapter 4). To determine the tube's radius, the average persistence length of several tubes with a minimum intensity was measured and the result was used in eq. 4.3 to find the proportionally constant α , between the radius of the tubes and their intensity ($r = \alpha I$). In this calculation we used a value of $\kappa = 24 k_B T$ for the bending rigidity of the POPC membrane [93]. Since the radius of the tubes is related linearly to their intensities in unilamellar area, the tube radius can easily be estimated using α . Figure 5.5 shows the diagram of the persistence length of the nanotubes versus their radius. In this diagram, eq. 4.2 has been fitted on experimental data of the bare tubes (blue circles) giving the bending rigidity of the membrane approximately $\kappa = 22 k_B T$, which is in agreement with the bending rigidity of the POPC membrane ($\kappa = 19 k_B T$ in reference [88] and $\kappa = 24 k_B T$ in reference [93]).

To investigate the effect of F-BAR on the tubes' persistence length, they were incubated in a high concentration of the F-BAR in a 2D chamber. The intensity of the tubes was measured in the same assay as the bare tubes and their radius was calculated from their intensity. The red squares in Figure 5.5A represent the persistence length of the F-BAR coated tubes, which has been plotted versus the tubes' radius. Interestingly, the radius of the tubes is smaller compared to bare tubes' radius; the linear fit of eq. 4.2 to the data provides the bending rigidity of the F-BAR coated lipid tubes $\kappa = 95 k_B T$. Hence, syndapin 1 proteins induce more curvature on the tubes. Moreover, their radius decreases while their persistence length increases. Figure 5.5 shows a bare membrane nanotube and a F-BAR coated membrane nanotube (B and C in Figure 5.5 illustrate three consecutive images of fluctuation in different colors were merged). They have the same radius, but the F-BAR coated nanotube has a bigger persistence length (bare tube, $R=24 \text{ nm}$ and $L_p = 1.7 \mu\text{m}$; F-BAR coated tube, $R=22 \text{ nm}$ and $L_p = 4.3 \mu\text{m}$).

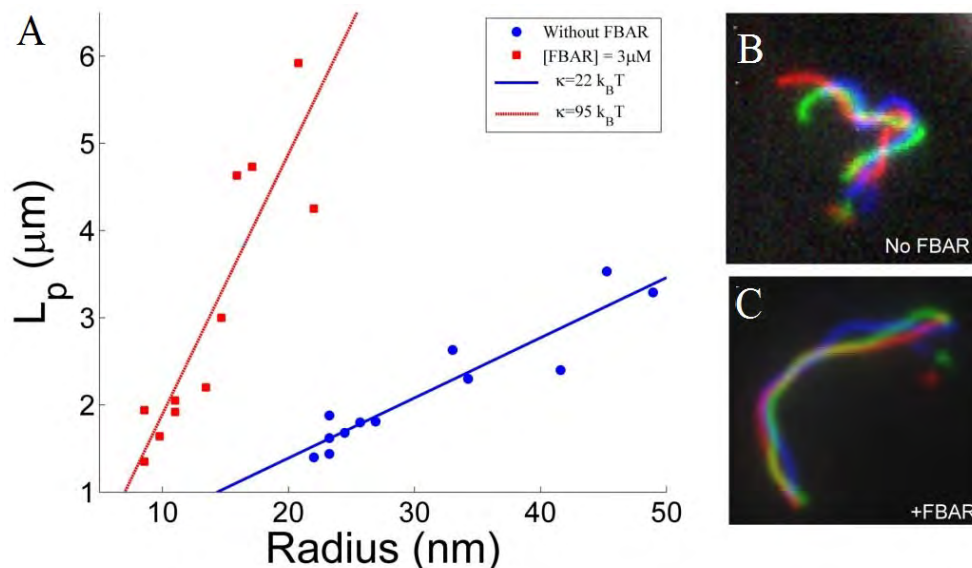


FIGURE 5.5: The F-BAR changes the persistence length and radius of membrane tubes. A) The persistence length diagram of phospholipid nanotubes for the bare membrane tubes (blue circles, 12 tubes) and the F-BAR coated tubes (red squares, 11 tubes). B and C) Three consecutive merged images of a bare lipid tube (B) and a F-BAR coated tube (C) which have a similar size. The F-BAR coated tube is clearly more straight than the bare lipid tube. The images are $13\mu\text{m} \times 13\mu\text{m}$.

5.1.5 Tubulation of the vesicle membrane in the presence of the F-BAR

The tubulation of GUVs' membrane was observed in the presence of F-BAR with a $3\mu\text{M}$ concentration during the experiment and the chamber preparation (Figure 5.6). This observation clearly reveals that the F-BAR domains induce membrane curvature at a high concentration. Tubulation of the membrane in the presence of the BAR domains was investigated in more detail with respect to the Arfaptin and I-BAR domains. This will be discussed in the following sections.

5.2 Arfaptin coated phospholipid nanotubes

Arfaptin domain proteins as well as the F-BAR domain have positive charges on their concave side and have the ability to induce a positive curvature on a membrane. Our research revealed that the tubulation of membranes happens in the presence of a high concentration of Arfaptin (Figure 5.7). In this experiment, GUVs were created by the electroformation method from POPC:DOPS:TR-DHPE (79.5:20:0.5) in 300 mM sucrose. The GUVs' solution was suspended in an isotonic medium, 280 mM sucrose plus 10 mM PBS buffer, and before being delivered to the chamber, incubated in a

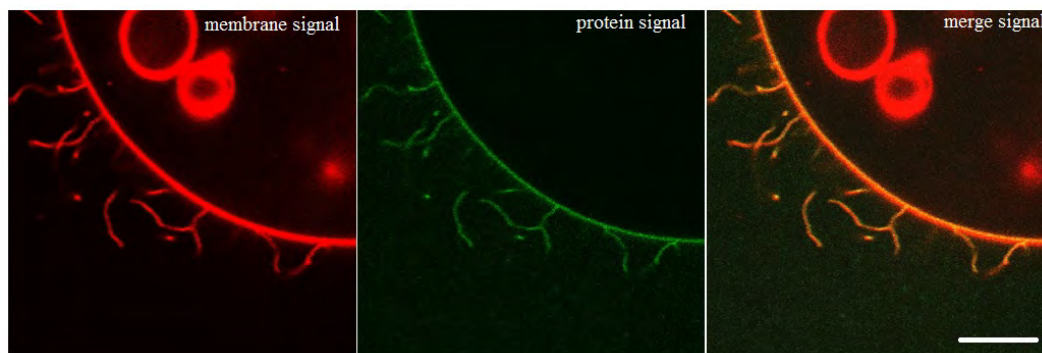


FIGURE 5.6: Tubulation of the membrane: the GUV was incubated in a buffer solution 270 mM sucrose and 15 mM NaCl with 500 nM of F-BAR proteins. Membrane and proteins signals are red and green respectively. The scale bar is $10\mu\text{m}$.

$3\ \mu\text{M}$ concentration of Arfaptin domain proteins. The Arfaptin domains had been labeled with Alex 488, fluorescent dye, with an excitation maximum of 495 nm and an emission of 519 nm. The chamber was made (appendix C) and transferred to the microscope. After several minutes, there were many protein coated vesicles exhibiting tubulation (Figure 5.7). The Arfaptin coated nanotubes around the GUVs have a similar intensity, and hence a similar thickness. They were very flexible and tangled compared with the F-BAR membrane tubulation (see Figure 5.6 and 5.7 for comparison). It can be said that they have a smaller persistence length than bare tubes and F-BAR coated phospholipid nanotubes since Arfaptin coated tubes are thinner and appear more flexible than them. In our Matlab program, the tracking and digitizing of a filament with a bigger persistence length than $1\ \mu\text{m}$ was quite simple. However, with regard to the Arfaptin coated nanotubes, they seem to have the persistence length less than $1\ \mu\text{m}$, because it was not possible to track and find the persistence length form confocal images.

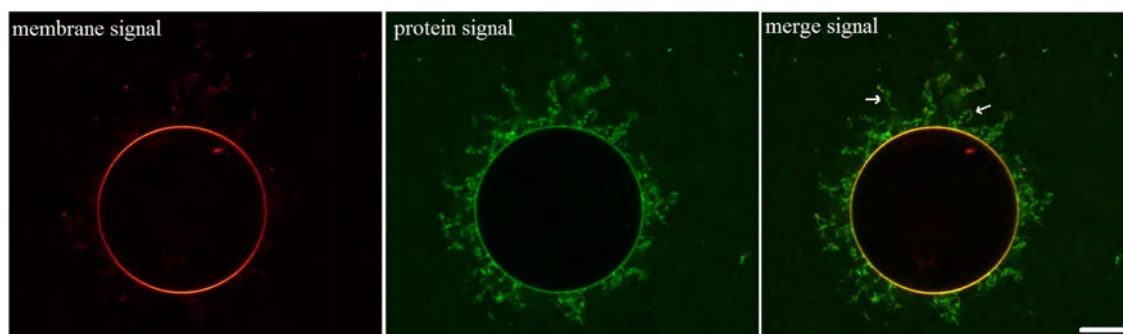


FIGURE 5.7: Tubulation of a typical vesicle membrane: the GUV was incubated in a buffer solution of 280 mM sucrose and 10 mM NaCl with $3\ \mu\text{M}$ Arfaptin proteins. The membrane and protein signals are red and green respectively. The scale bar is $10\mu\text{m}$.

5.3 I-BAR coated phospholipid nanotubes

In contrast to other BAR domains, I-BAR domains have a positive intrinsic curvature. They bind to a membrane with their convex face. They can bind to membranes by either electrostatic interactions such as IRSp53 and IRTKS or additionally by penetrating the amphipathic helix into the membrane such as MIM and ABBA [94]. I-BAR domain proteins regulate the protrusions of filopodia [75, 95] and play an important role in remodeling the membrane in the phagocytosis process [73]. Here, the tubulation dynamics of GUVs were investigated, which were exhibited by binding I-BAR domain proteins (ABBA type) to the vesicle membrane. In particular, the persistence length of the I-BAR coated tubes was measured for the first time. Experimental methods and results will be described in the following subsections.

5.3.1 Tubulation by I-BAR domains can be reversibly controlled by protein concentration

GUVs were made in 300 mM sucrose from DOPC:DOPS:TR-DHPE (79.5:20:0.5). A chamber and micropipette for injecting the I-BAR (or aspiration) was prepared as explained in appendix C. The pipettes were filled with I-BAR proteins with a concentration of 40 μ M and then the tip of a typical micropipette was gently positioned into the chamber, close to an attended GUV; the system was allowed to equilibrate a few minutes before the I-BAR injection.

The I-BAR (ABBA type) was injected by the micropipette around a typical vesicle. During the injection, inwards' I-BAR coated tubes emerged and began to elongate. Figure 5.8 1 shows that the binding between proteins and the vesicle membrane occurred as soon as I-BAR was injected. Tubulation began to form on the injection side of the membrane (left side in Figure 5.8 2) and then spread to the entire surface of the membrane by increasing the concentration of proteins (Figure 5.8 3). When injection was stopped and therefore, concentration of I-BAR around the vesicle had decreased (due to protein diffusion to the other parts of the chamber), tubes began to shrink toward the membrane (Figure 5.8 4,5). This experiment revealed that the tubulation on the membrane depends on the protein concentration and that can be reversibly controlled. I-BAR domains had been labeled with YFP, fluorescent dye, with an excitation maximum of 514 nm and an emission of 527 nm.

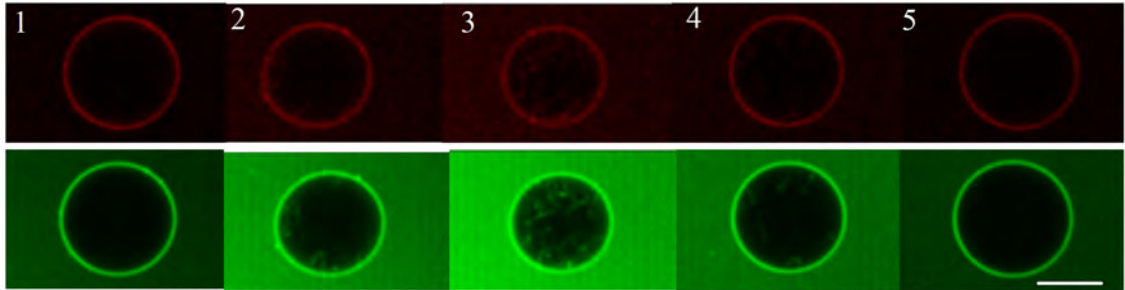


FIGURE 5.8: Tubulation of a typical vesicles' membrane: Red and green signals are membrane and ABBA signals, respectively. Step 1) ABBA injected around the vesicles; there is a good binding between proteins and the membrane. Step 2) ABBA was injected from the left side of the vesicle causing it to tubulate from that side. Step 3) More ABBA was injected and there is maximum degree of tubulation. Step 4 and 5) There was no injection of ABBA and with a decrease of the I-BAR concentration, tubes shrink to the GUV membrane. The scale bar is $10\mu m$.

Figure 5.9 shows the diagram of intensity around and inside a typical vesicle during I-BAR injection. When ABBA concentrations around the vesicle (red points) increased, ABBA coated tubes began to grow toward the inside of the vesicle. Then the intensity of the protein signal was increased at the inside of the vesicle due to the increase of the tubes' amount. The intensity of the inside of the vesicle was measured in two areas, the center circle with $2/3$ of radius of the vesicles (area 1) and the area between area 1 and the membrane (area 2). It can clearly be seen in Figure 5.9 that, at the beginning of injection, tubes are short and only fluctuate in area 2, so the intensity of area 2 increases (green points), however, for area 1 the intensity is almost zero. By increasing ABBA concentration to a maximum amount, the tubes then to elongate further and reach area 1. Subsequently, the intensity of this area 1 (blue points) increases as well as area 2. After halting the injection, the ABBA concentration begins to decrease and the tubes shrink back to the membrane (last image of the vesicle).

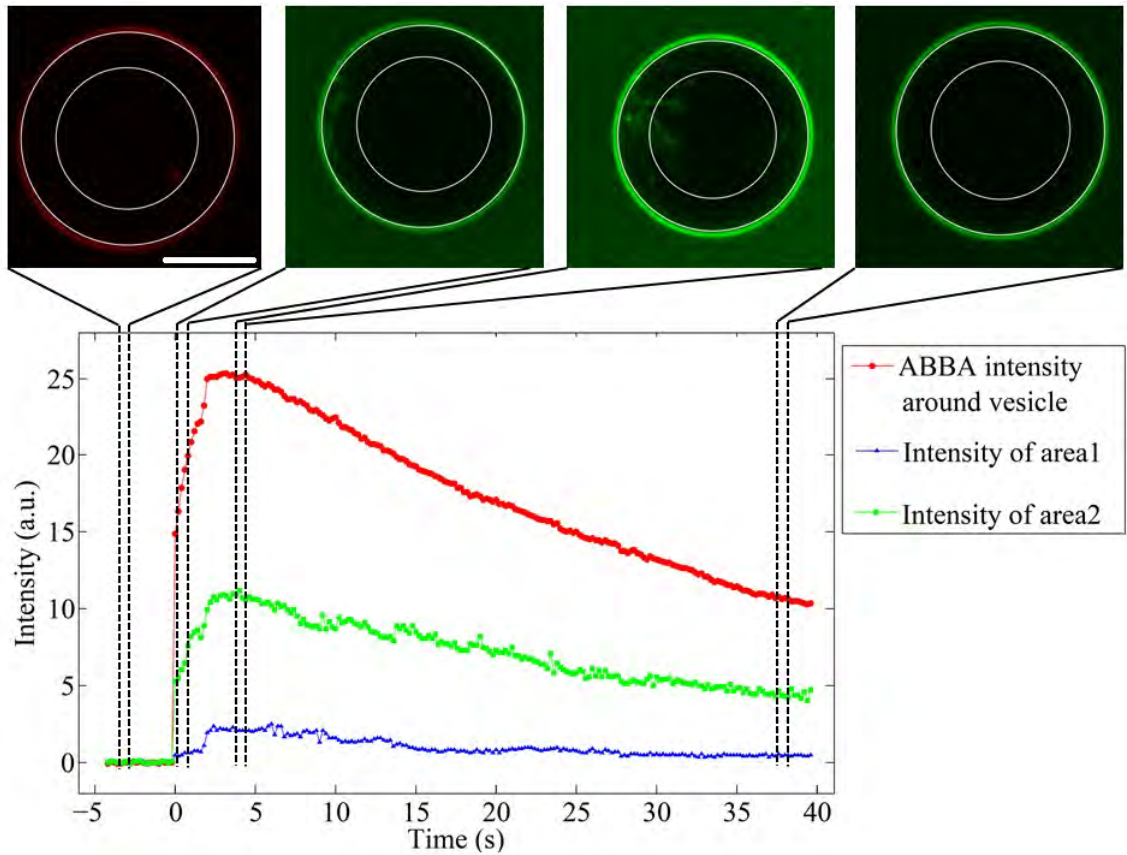


FIGURE 5.9: Tubulation of a vesicle membrane by ABBA domain proteins and the elongation of the created tubes by its concentration. With increasing ABBA concentration around the membrane, tubes are generated and begin to elongate and fill the inside area of the vesicle (area 1 and 2, see text). The tubes are reversible and shrink back to the membrane by decreasing the concentration of proteins. In first the image of the vesicle, there is no injection of ABBA and so then the radius of vesicle was quantified by using the membrane signal. Scale bar is $10 \mu m$

The other important parameter is how much of the membrane area could decrease because of tubulation. For measuring the decreased area, the radius (area) of the vesicle is calculated during the injection of ABBA (tubulation). Figure 5.10 shows the diagram of the vesicle radius vs. time. The radius of the vesicle decreases due to tubulation (an increase of I-BAR concentration around the vesicle) and increases after halting the injection (the shrinking of the tubulation to the membrane). As an example for the vesicle which has been shown in Figure 5.10, the radius of the vesicle reduces from $\sim 12.5 \mu m$ (the first image in Figure 5.9) to $\sim 11 \mu m$ (the third image in Figure 5.9) by tubulation.

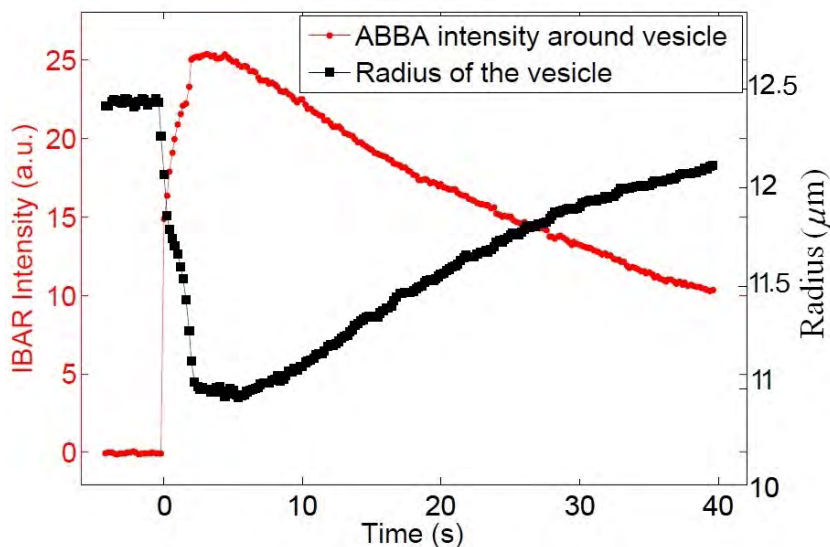


FIGURE 5.10: Increasing ABBA intensity (till $t=5$ s) leads to the tubulation of the vesicle and, as a result, the radius of the vesicle decreases (see vesicle images in Figure 5.9).

5.3.2 Tubulation by I-BAR domains can be reversibly controlled by the membrane surface tension

In the aspiration method, a part of the vesicle is aspirated into the micropipette. As it was explained in Section 2.6 the aspiration pressure on the membrane increases the tension (equation 2.7) and the area of the membrane (equations 2.8 and 2.9). Increasing tension of the membrane could also be induced by the tubulation of the membrane. In the aspiration method a tube with a large radius (the pipette's radius) is aspirated into pipette from the vesicle but in tubulation many of the inward nanotubes are produced by the I-BAR proteins. The question is if it is possible that nanotubes shrink back to the membrane due to aspiration of a tubulated vesicle. Figure 5.11A shows a schematic of a tubulated vesicle by the I-BAR domains and the idea of the reversibility of tubes on the membrane during micropipette aspiration (Figure 5.11B). Therefore the tension can apparently regulate the formation of tubes. This result has important implications to understanding how the membrane tension regulates floppia formation.

The GUVs' chamber was prepared as explained in appendix C in 20mM PBS and 260 mM sucrose with $3 \mu\text{M}$ I-BAR domains. This concentration of I-BAR was enough to tubulate the vesicles. The aspiration glass micropipettes were made in a diameter of $5 \mu\text{m}$ to $10 \mu\text{m}$. The pipettes were then filled with the sample solution containing 2 mg/ml BSA (to prevent adhesion of the membrane lipids to the internal surface of the micropipette) in 20mM PBS and 260 mM sucrose. Then the tip of a typical micropipette was gently positioned into the chamber close to a tubulated GUV and the system was

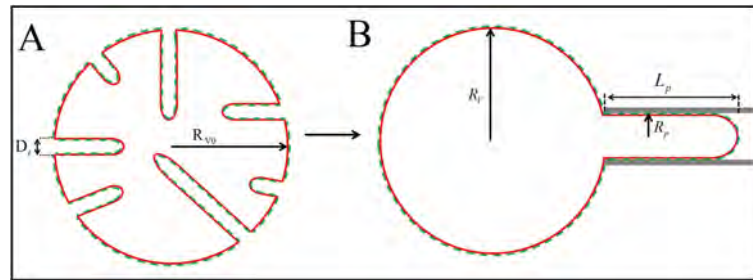


FIGURE 5.11: A schematic of a tubulated vesicle by I-BAR (A) and the reversibility of tubes to the membrane by micropipette aspiration (B).

allowed to reach equilibrium a few minutes before the imaging and aspiration of the GUV. Aspiration of the membrane into the micropipette caused the tubes to shrink back on the membrane (Figure 5.12 1-3). The aspiration length for the disappearing tubes was different depending on how much of the area of the vesicle was tubulated before aspiration. To consider reversibility of the tubes, the aspirated vesicle was pushed out of the micropipette and the vesicle re-tubulated after the extra tension disappeared on the membrane (Figure 5.12 4-6).

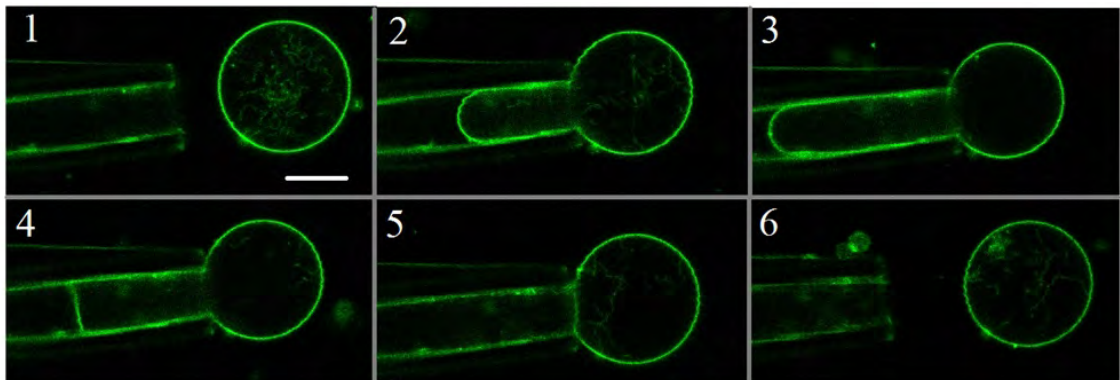


FIGURE 5.12: Micropipette aspiration of a typical tubulated vesicle. Steps 1-3) by aspiration of a vesicle, the tension on the membrane increases and it causes the tubes to shrink back to the membrane. Steps 4-6) The reversibility of tubulation: the vesicle was pumped out of micropipette by reversing the pressure inside the micropipette which decreases the tension on the membrane and allows IBAR to form inward tubes. The scale is $10 \mu m$.

5.3.3 The persistence length of I-BAR coated phospholipid nanotubes

In section 5.1, it was explained how the F-BAR can sense various curvatures on a membrane and bind to membrane nanotubes. We also found the persistence length of F-BAR coated nanotubes. Here, the same method was used to find the persistence length of the I-BAR coated membrane nanotubes. I-BAR domains (ABBA type in our research) bind to vesicles membrane and generate nanotubes in a diameter of 55 nm [94]. The radius of ABBA coated nanotubes is then known ($r \approx 27 \text{ nm}$) and by measuring their persistence lengths, the bending rigidity of I-BAR coated tubes can be calculated (see equation 4.2).

The chamber containing the GUVs was prepared as it was explained in the previous subsection. Subsequently, consecutive images of several GUVs with I-BAR coated nanotubes were taken under confocal microscopy. Tubes in focus were tracked and digitized by using the Matlab program. Then tangent vectors along the nanotube (one vector at each digitized point) were extracted. Figure 5.13 shows a typical tubulated vesicle with many ABBA coated tubes and a tracked line of one of them. In each vesicle, approximately 100-150 tubes were digitized for measuring persistence length. The persistence length was measured for tubes of several vesicles with a result of $L_p \simeq 7.6 \pm 0.2 \mu\text{m}$. By using equation 4.2, the bending rigidity of the ABBA coated nanotubes was found to be approximately $44 k_B T$, which is twice as much compared to a bare membrane. IBAR can therefore mechanically stabilize filopodia to some degree in cooperation with the internal actin.

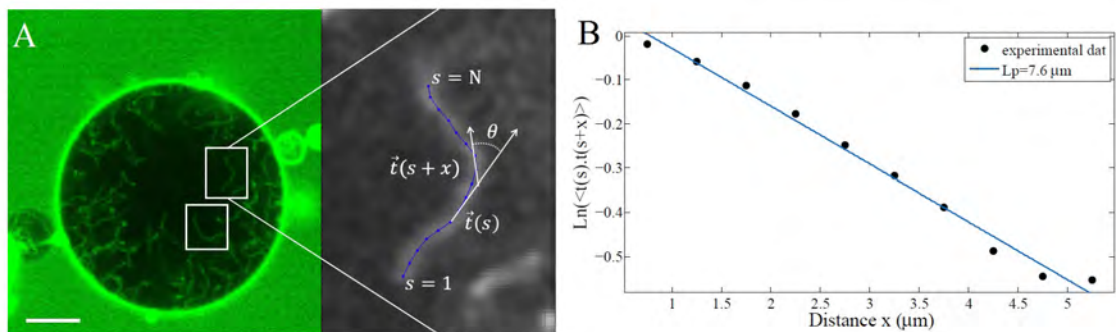


FIGURE 5.13: A) Nanotubes tracking: I-BAR coated nanotubes in focus from consecutive images were digitized to measure the persistence length. Scale bar is $5 \mu\text{m}$. B) The CCF graph of I-BAR (ABBA) coated membrane nanotubes, the slope identifies the persistence length of approximately $7.6 \mu\text{m}$, see equation 4.1.

Confocal microscopic images are not snapshots. Thus, it takes time to scan the length of a tube. Fluorescence snapshot images are usually used to find the persistence length of a filament. However, in our research, confocal images were used. To see how this issue effects our results, spontaneous phospholipids nanotubes were made form POPC

and their persistence length was measured from Hg the lamp snapshots as well as from confocal microscopy images (scan rate 400-500 Hz). Figure 5.14 shows the consecutive images of a typical phospholipid nanotube, which were taken by confocal microscopy (Figure 5.14A) and an EMCCD camera (Figure 5.14B). The nanotube is seen a tiny crinkle in the confocal images. However as shown in CCF diagram (Figure 5.14B), it has not effect on the measurement of the persistence length. This result confirmed that the confocal images can be used to find the persistence length of nanotubes (with our scanning rate to capture confocal images).

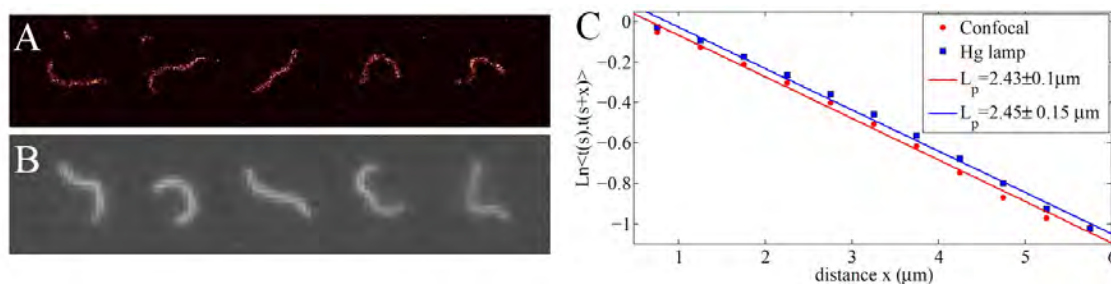


FIGURE 5.14: The consecutive images of a typical phospholipid nanotube which were captured by confocal microscopy (A) and an EMCCD camera (B). C) CCF graph of the persistence of nanotubes which was created from the confocal images (red points) and an EMCCD camera (blue points).

5.3.4 Making inward tubes by optical tweezers without and in presence of I-BAR

Lipid nanotubes (normally called tether) can be extracted from the membrane by applying a point force using optical tweezers. Pulling the tubes outward (tethers) from the vesicle membranes was already used to consider the curvature sensing of BAR domain proteins on the membrane, e.g. F-BAR and N-BAR domains which sense and generate positive curvatures. I-BAR proteins have negative curvatures and induce inward vesicle tubulation. These proteins bind to the nanotubes' membrane from the inside leaflet against the F-BAR and N-BAR domains. Making an inward tube by using optical tweezers has been successfully done recently [96]. Here, for the investigation of I-BAR sensing, an inward tether was pulled into the vesicle membrane. GUVs were prepared in 200 mM sucrose and were delivered to the chamber with 2.5 micrometer beads and a low concentration of salt (10 mM). Optical tweezers were used to push a trapped bead inside the attached vesicle to create the inward tube, however, the force of the optical tweezers was not enough to make the inward tether. To decrease the tether force, GUVs were incubated in 280 mM sorbitol and 10 mM salt. In this situation, in order to balance the osmotic pressure, a volume of water from the inside of the vesicle permeates to the

outside medium and the vesicle becomes floppy resulting in a decrease in the membrane tension. The force to create a tether from a vesicle membrane will decrease linearly with the tension (see equation 2.12a). Thus, it was quite simple to make the inward tube from the floppy vesicles. Figure 5.15 shows a typical experiment to create an inward tube and the tether force during the process.

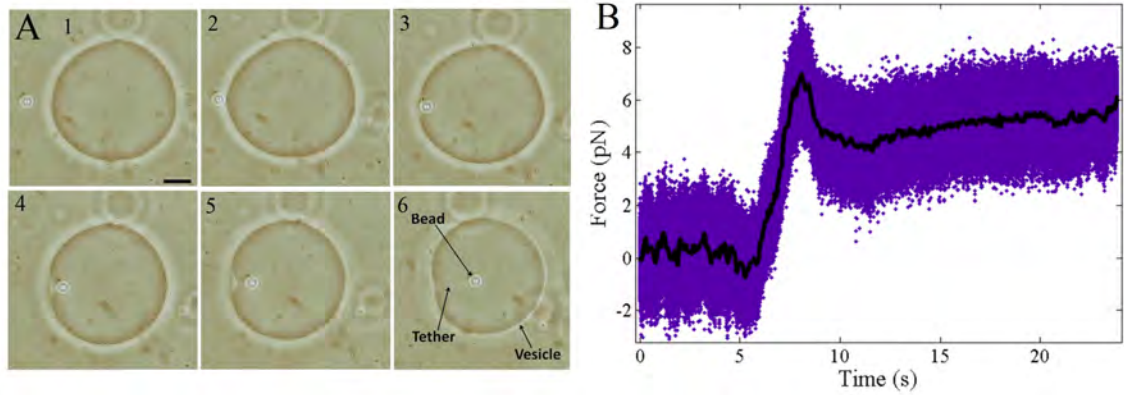


FIGURE 5.15: Inward nanotube (consecutive phase contrast microscopic images): a 2.5 micrometer bead pushed to the inside of the vesicle membrane to make an inward tether. B) The tether force behaviors versus elongation time. The scale bar is $10\mu m$.

Inward tubes which were created from floppy vesicles have a larger radius than ordinary vesicle tethers (Figure 5.16 A). In the second step, approximately $2\mu m$ ABBA domain proteins were added to the chamber and an inward tube was pulled into the proteins' coated vesicle membrane (Figure 5.16). The ABBA coated inward tubes were observed to have a smaller radius compared to tubes without the ABBA. It seems ABBA proteins induce more curvature on inward pulled nanotubes, which create thinner nanotubes as shown in Figure 5.16 B.

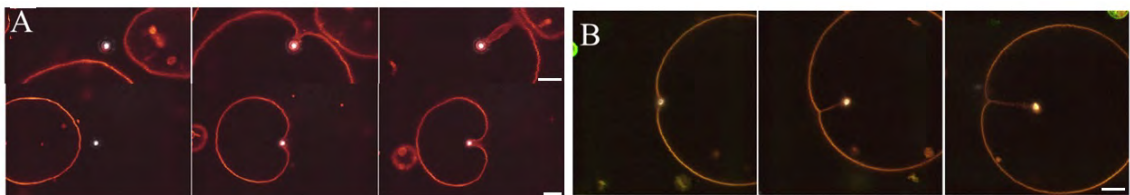


FIGURE 5.16: Inward nanotubes. The inward nanotube pulled by optical tweezers force from bare vesicles (A) and an ABBA coated membrane (B). The scale bar is $10\mu m$.

5.4 Conclusions

Membrane nanotubes with different radii (curvatures) were extracted from the vesicle membranes and the curvature sensitivity of the F-BAR proteins was investigated by measuring the sorting of proteins on the GUVs and tubes. The result revealed the high preference of the F-BAR to bind to thin nanotubes at low protein concentration. The rigidity of the F-BAR coated membrane nanotubes was also measured and calculated by analyzing their persistence length. The smallest radius for bare spontaneous nanotubes is approximately 20 nm whereas F-BAR proteins bind to nanotubes membrane and induce more bending (make them thinner). The smallest radius was measured for the F-BAR coated tubes approximately 10 nm. The tubulation of the vesicle membrane was observed at high concentration of the F-BAR and Arfaptin domains and it was found that Arfaptin coated tubes are more thinner and flexible than F-BAR coated tubes. We also saw that I-BAR domains create inward tubulation of the vesicle membrane depending on I-BAR concentration and that it can be reversibly controlled by changing the external protein concentration. By micropipette aspiration, it was proved that the tension on the I-BAR coated membranes can control the tubulation in a reversible manner. Together these results show that IBAR and membrane tension play together in mechanically regulating membrane protrusion which has important implications for understanding the stability and formation of membrane structures like filopodia.

Chapter 6

Conclusions and outlook

Two aims were formulated for the overall project, which were: to investigate the mechanical properties of phospholipid nanotubes and to measure the effect of BAR domain proteins on lipid nanotubes.

Confocal microscopy together with Hg lamp illumination were used to capture the images of phospholipid nanotubes. The curvatures on the phospholipid nanotubes during thermal fluctuation were seen using images from Mat Lab software. These curvatures were then used to find the persistence length of the phospholipid nanotubes. The nanotubes' radii were calculated by quantifying the magnitude of the tubes persistence length and their intensity under confocal microscopy. For the first time, the linear dependence between the persistence length and tubes' radius was proven. It was also discovered that phospholipid nanotubes are either uni- or multilamellar when formed by spontaneous swelling.

Phospholipid nanotubes with different diameters (or curvatures) were extracted from the vesicle membranes in the presence of F-BAR proteins. Intensity measurements from the protein signal on tubes of controlled radius showed that F-BAR has a high preference for thin nanotubes. The persistence length analysis of the F-BAR coated nanotubes revealed a high bending rigidity in comparison to the bare nanotubes. In addition, with a high concentration of F-BAR proteins, tubulation of the membrane was seen around the vesicles membrane in a similar fashion as for Arfaptin.

The tubulation of the membrane in the presence of I-BAR proteins was investigated. I-BAR contrary to F-BAR and Arfaptin caused tubulation on the inside of vesicle membrane. A linear dependence was discovered between the elongation of tubes and the I-BAR concentration. Furthermore, the micropipette aspiration of the tubulated vesicles proved that tubulation reversibly depends on membrane tension. Finally, the persistence length of the I-BAR coated phospholipid nanotubes was found approximately 2 times bigger than bare membrane nanotubes with the same diameter.

Knowledge of the interaction between membrane nanotubes and BAR domain proteins is useful to understand the role of membrane associated proteins in biological processes, e.g. endocytosis, membrane budding and filopodium formation. The presented results and analytical methods developed here provide an excellent strategy for investigating the mechanical effects of BAR domain proteins (or other membrane binding proteins) on tubular membranes. The results from these experiments will contribute to the understanding of the mechanisms behind the formation of the many tubular shapes found in cells.

Chapter 7

Appendices

7.1 Appendix A

Driving of the equation 4.1

The bending energy of a filament with length L is given by [80]:

$$E_{bend} = \frac{EI}{2} \int_0^L \left(\frac{d\theta}{ds}\right)^2 ds \quad (7.1)$$

where EI is the flexural rigidity of the filament (E and I are Young's modulus and the geometrical moment of inertia of the cross-section of the filament respectively). $\theta(s)$ and s are the tangent angle and the arc length along the filament respectively.

The persistence length is called the competition between the thermal and bending energy, $L_p = \frac{EI}{kT}$. The cosine (tangent) correlation function (CCF) is a mathematical method to characterize the space curves of the filament. CCF is defined as:

$$g(s) = \langle t(0) \cdot t(s) \rangle = \langle \cos\theta(s) \rangle \quad (7.2)$$

where $t(0)$ is a tangent vector in the initial position and s is the distance of the tangent vector $t(s)$ from $t(0)$ (Figure 7.1A). The average is over time during fluctuation, which involves all configurations of the filament.

For small angles ($\theta(s) \ll 1$), eq. 7.2 can be rewritten as [97]:

$$g(s) = \left\langle 1 - \frac{\theta^2(s)}{2} \right\rangle \quad (7.3)$$

All possibilities of the tangent vector orientation in three dimensions can be written as:

$$\langle \theta^2(s) \rangle = \frac{1}{Z} \int_0^{2\pi} d\phi \int_0^\pi \theta^2 \sin\theta e^{(EI/2k_B T s)\theta^2} d\theta \quad (7.4)$$

where

$$Z = \frac{1}{Z} \int_0^{2\pi} d\phi \int_0^\pi \sin\theta e^{(EI/2k_B T s)\theta^2} d\theta \quad (7.5)$$

Equation 7.4 can be rewritten as:

$$\langle \theta^2(s) \rangle = \frac{-2k_B T s}{I} \frac{\partial \ln Z}{\partial E} \quad (7.6)$$

By substitution of θ instead of $\sin\theta$ for small angles and changing variable $u = (EI/2k_B T s)\theta^2$:

$$Z = \frac{2\pi k_B T s}{EI} \int_0^\infty e^{-u} du = \frac{2\pi k_B T s}{EI} \quad (7.7)$$

Hence, by substitution equations 7.6, 7.7 and 7.4 in eq. 7.3:

$$g(s) = 1 - \frac{k_B T}{EI} s = 1 - \frac{s}{L_p} \quad (7.8)$$

In the $s \ll L_p$, it is obtained:

$$g(s) = \exp\left(\frac{-s}{L_p}\right) \quad (7.9)$$

In two dimensions, L_p should be replaced with $2L_p$.

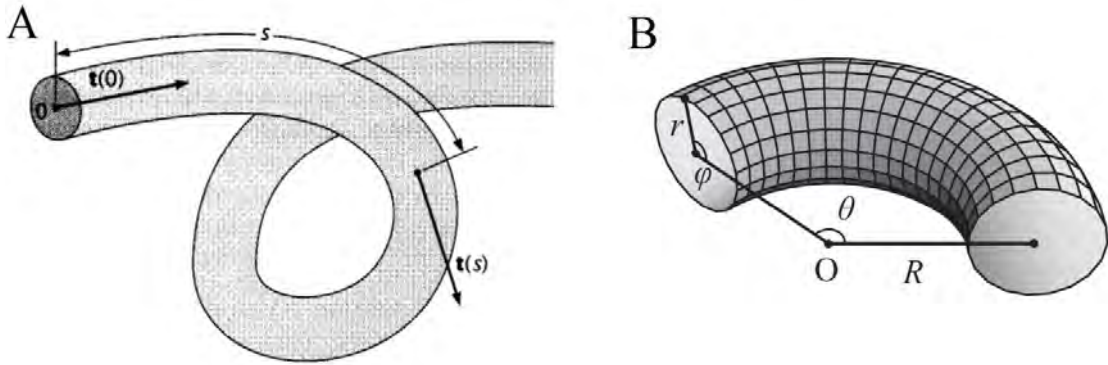


FIGURE 7.1: A) A drawing of a tube with tangent vectors B) A small section of the tube which shows two principal radii of curvatures and bending angles

Driving of the equation 4.2

The bending energy of the membrane with area A and the two principal curvatures of C_1, C_2 are given by the Helfrich energy as:

$$E_H = \frac{\kappa}{2} \oint (C_1 + C_2 + C_0)^2 dA \quad (7.10)$$

In our case the lipid composition in the two leaflets is the same and also there is no difference between the solution of the inside and outside of the vesicle which causes a value of zero for the spontaneous curvature ($C_0 = 0$). Figure 7.1B shows a bend on a nanotube with two principal curvatures. The bending angles are θ and φ . Therefore, C_1 and C_2 are given by:

$$C_1 = \frac{1}{r} \quad (7.11a)$$

$$C_2 = \frac{\cos \varphi}{R + r \cos \varphi} \quad (7.11b)$$

For a small bend, the area element is given as $dA = rd\varphi.(R + r \cos \varphi)d\theta$. Thus, for small angle $\Delta\theta$, the bending energy becomes [48] :

$$\Delta E_H = \frac{\kappa}{2} \frac{2\pi}{r} \frac{1}{\sqrt{1 - r^2 c^2}} \Delta S \quad (7.12)$$

where c is the curvature of the tangent circle on the selected element and $\Delta S = R\Delta\theta$. Taylor series of ΔE_H becomes:

$$\Delta E_H = \frac{\kappa\pi}{r} \Delta S + \frac{r\kappa\pi}{2} \Delta S c^2 + \dots \quad (7.13)$$

The first term is the bending energy for creating tube and the second term is the bending energy of the tube's backbone.

On the other hand, for a filament, the bending energy of the filaments' backbone in two spatial dimensions is given by the persistence length term L_p , as [48]:

$$\Delta E = \frac{K_B T L_p}{4} \Delta S c^2 \quad (7.14)$$

Hence, eq. 4.2 can be obtained by the combination of equations 7.13 and 7.14 :

$$L_P = \frac{2\kappa\pi r}{k_B T} \quad (7.15)$$

7.2 Appendix B

Power spectrum method for calibration of optical tweezers

The position of a bead in trap, $x(t)$, is described well by the Langevin equation [98]:

$$m\ddot{x}(t) + \gamma\dot{x}(t) + kx(t) = F_{therm}(t) \quad (7.16)$$

with m the bead's mass, γ the friction coefficient, and k the trap stiffness. In water, the first term is negligible compared to the other terms. $F_{therm}(t)$ is a random thermal fluctuation force.

A quadrant photodiode (QPD) was used to detect the position of the bead in the trap which the raw data of photodiode ($S(t)$) is in volts. $S(t)$ and $x(t)$ are linearly proportional ($x(t) = \beta S(t)$). The Fourier transform of the voltage signal with time T , can be written as:

$$S(f) = \int_{-\frac{T}{2}}^{\frac{T}{2}} S(t)e^{i2\pi ft} dt \quad (7.17)$$

The power spectrum of the data can be obtained by using eq. 7.16 and 7.17:

$$P(f) = \left\langle \frac{|S(f)|^2}{T} \right\rangle = \frac{k_B T}{2\gamma\pi^2\beta^2(f_c^2 + f^2)} \quad (7.18)$$

where f_c is the corner frequency and is related to the trap stiffness, $f_c = \frac{k}{2\pi\gamma}$.

Figure 7.2 shows a power spectrum of a bead that was used in our experiment.

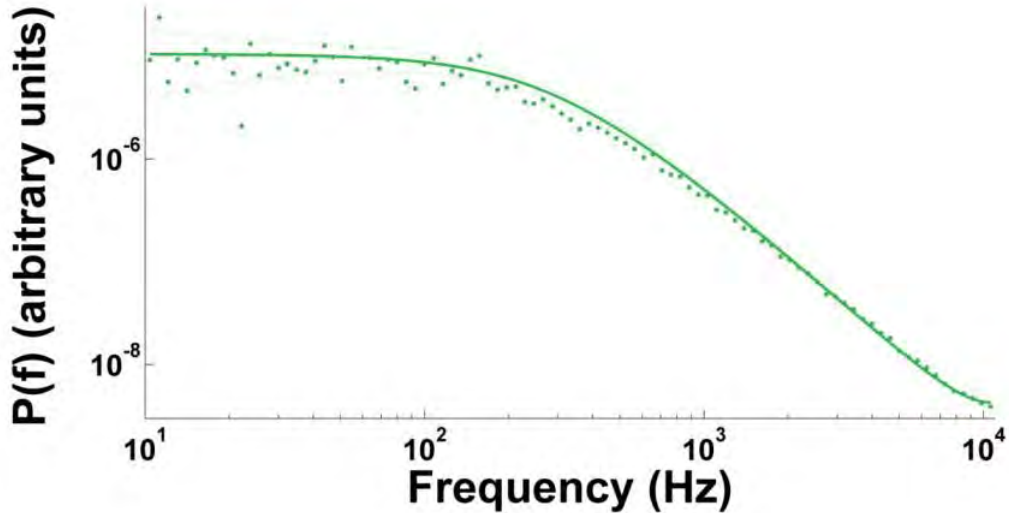


FIGURE 7.2: Power spectrum diagram for calibration of the optical trap. It illustrate the Fourier transformed of photodiode data with a Lorentzian fit on them (see eq. 7.18) giving the corner frequency of $f_c = 261Hz$.

7.3 Appendix C

Preparation of the giant unilamellar vesicles

To make synthetic lipid GUVs, DOPC, DOPG, DSPE-PEG(2000) Biotin, and Texas Red DHPE (molar ratio of 74:25:0.7:0.3) were mixed in chloroform. Hence, by using a Hamilton syringe, 10 μ l of lipid solution was spread on the glass slides' surface, which was coated in indium titanium oxide (ITO). In order to better spread of the highly charged lipid mixture, about 30% volume ratio methanol was used. To evaporate the chloroform and methanol, slides were dried under nitrogen flow for a few seconds. Hence, the slides were placed into a vacuum chamber for 1-2 hours to complete the evaporation of chloroform (and methanol). Finally, giant unilamellar vesicles were prepared by the electroformation method in a 300mM sucrose solution.

Preparation of the chamber for tether pulling and protein injection

A thin, square frame from PDMS was coated on a clean glass slide (25 X 50 mm # 1) and the inside volume of the frame was filled by α - *Casein* solution (2 mg/ml) and allowed to incubate for 15 minutes. Then the volume was successfully washed with 15mM NaCl, 270mM sucrose. Coating the glass with α - *Casein* prevents membrane-glass adhesion. The chamber was closed with a coverglass to allow using the immersion oil condenser (for measurements the trap signal by photodiode). One side of the PDMS was removed to allow the pipette to enter the chamber and the volume was loaded with a vesicle solution.

Glass micropipettes were made using a micropipette puller (P-97 Flaming/Brown Micropipette Puller, Sutter Instruments) and their tip fabricated to a diameter between 5 μ m to 10 μ m using the Micro Forge MF-900, Narishige co. ltd Japan. In the aspiration experiment, a pipette was filled with α - *Casein* solution and washed several times with 15mM NaCl, 270mM sucrose. Then pipette was filled with 15mM NaCl, 270mM sucrose, which was gently pipetted into the chamber.

References

- [1] Bruce Alberts, Alexander Johnson, Julian Lewis, Martin Raff, Keith Roberts, and Peter Walter. *Molecular Biology of the Cell*. Garland Science, 5 edition, November 2007.
- [2] Bruce Alberts, Dennis Bray, Karen Hopkin, Alexander Johnson, Julian Lewis, Martin Raff, Keith Roberts, and Peter Walter. *Essential Cell Biology*. Garland Science, 3 edition, March 2009.
- [3] Jacob N. Israelachvili, D. John Mitchell, and Barry W. Ninham. Theory of self-assembly of hydrocarbon amphiphiles into micelles and bilayers. *J. Chem. Soc., Faraday Trans. 2*, 72:1525–1568, 1976.
- [4] S Lawrence Zipursky Paul Matsudaira David Baltimore Harvey Lodish, Arnold Berk and James Darnell. *Molecular Cell Biology*. W. H. Freeman and company, New York, 6 edition, November 2008.
- [5] A.D. Bangham and R.W. Horne. Negative staining of phospholipids and their structural modification by surface-active agents as observed in the electron microscope. *Journal of Molecular Biology*, 8(5):660 – IN10, 1964.
- [6] Dirk van Swaay and Andrew deMello. Microfluidic methods for forming liposomes. *Lab Chip*, 13:752–767, 2013.
- [7] Luis Bagatolli and P. B. Sunil Kumar. Phase behavior of multicomponent membranes: Experimental and computational techniques. *Soft Matter*, 5:3234–3248, 2009.
- [8] John P. Reeves and Robert M. Dowben. Formation and properties of thin-walled phospholipid vesicles. *Journal of Cellular Physiology*, 73(1):49–60, 1969.
- [9] Miglena I. Angelova and Dimiter S. Dimitrov. Liposome electroformation. *Faraday Discuss. Chem. Soc.*, 81:303–311, 1986.
- [10] Peter Walde and Sosaku Ichikawa. Enzymes inside lipid vesicles: preparation, reactivity and applications. *Biomolecular Engineering*, 18(4):143 – 177, 2001.

-
- [11] Reinhard Lipowsky. The conformation of membranes. *Nature*, 349:475–481, 1991.
- [12] E. Sackmann. Chapter 1 biological membranes architecture and function. In R. Lipowsky and E. Sackmann, editors, *Structure and Dynamics of Membranes*, volume 1 of *Handbook of Biological Physics*, pages 1 – 63. North-Holland, 1995.
- [13] Mun'delanji C. Vestergaard, Masamune Morita, Tsutomu Hamada, and Masahiro Takagi. Membrane fusion and vesicular transformation induced by alzheimer's amyloid beta. *Biochimica et Biophysica Acta (BBA) - Biomembranes*, 1828(4):1314 – 1321, 2013.
- [14] Emmanuel Boucrot and Tomas Kirchhausen. Endosomal recycling controls plasma membrane area during mitosis. *Proceedings of the National Academy of Sciences*, 104(19):7939–7944, 2007.
- [15] Coughlin Margaret Mitchison Timothy J. Mahadevan L. Charras, Guillaume T. Life and times of a cellular bleb. *Biophysical Journal*.
- [16] Natalia Stepanyants, Gavin D. M. Jeffries, Owe Orwar, and Aldo Jesorka. Radial sizing of lipid nanotubes using membrane displacement analysis. *Nano Letters*, 12(3):1372–1378, 2012.
- [17] R.M. Hochmuth, N. Mohandas, and P.L. Blackshear Jr. Measurement of the elastic modulus for red cell membrane using a fluid mechanical technique. *Biophysical Journal*, 13(8):747 – 762, 1973.
- [18] Schroer Trina A. Hirschberg Koret-Zaal Kristien J. M. Lippincott-Schwartz Jennifer Presley John F., Cole Nelson B. Er-to-golgi transport visualized in living cells. *Nature*.
- [19] Sheetz Michael P. Upadhyaya Arpita. Tension in tubulovesicular networks of golgi and endoplasmic reticulum membranes. *Biophysical Journal*, 86:2923–2928, 2004.
- [20] Salmon E.D. Waterman-Storer Clare M. Endoplasmic reticulum membrane tubules are distributed by microtubules in living cells using three distinct mechanisms. *Current Biology*, 8:798–807, 1998.
- [21] Marileen Dogterom, Jacob WJ Kerssemakers, Guillaume Romet-Lemonne, and Marcel E Janson. Force generation by dynamic microtubules. *Current Opinion in Cell Biology*, 17(1):67 – 74, 2005.
- [22] Deborah Kuchnir Fygenson, John F. Marko, and Albert Libchaber. Mechanics of microtubule-based membrane extension. *Phys. Rev. Lett.*, 79:4497–4500, Dec 1997.

- [23] H. Delanoë-Ayari, P. Lenz, J. Brevier, M. Weidenhaupt, M. Vallade, D. Gulino, J. F. Joanny, and D. Riveline. Periodic adhesive fingers between contacting cells. *Phys. Rev. Lett.*, 93:108102, Sep 2004.
- [24] Chabria Mamta Hall Heike Vogel Viola Moller Jens, Luhmann Tessa. Macrophages lift off surface-bound bacteria using a filopodium-lamellipodium hook-and-shovel mechanism. *Sci. Rep.*, 3, 2013.
- [25] Vogel Viola Albuschies Jrg. The role of filopodia in the recognition of nanotopographies. *Sci. Rep.*, 3, 2013.
- [26] Membrane curvature and mechanisms of dynamic cell membrane remodelling. *Nature*, 438:590–596, 2005.
- [27] Hye-Won Shin, Hiroyuki Takatsu, and Kazuhisa Nakayama. Mechanisms of membrane curvature generation in membrane traffic. *Membranes*, 2(1):118–133, 2012.
- [28] Amin Rustom, Rainer Saffrich, Ivanka Markovic, Paul Walther, and Hans-Hermann Gerdes. Nanotubular highways for intercellular organelle transport. *Science*, 303(5660):1007–1010, 2004.
- [29] E Lou, S Fujisawa, A Morozov, A Barlas, Y Romin, Y Dogan, S Gholami, AL Moreira, K Manova-Todorova, and MA Moore. Tunneling nanotubes provide a unique conduit for intercellular transfer of cellular contents in human malignant pleural mesothelioma. *Plos One*, 7(5):e33093, 2012-01-01 00:00:00.0.
- [30] Björn Nefel, Shlomo Nedvetzki, Richard K. P. Benninger, Marco A. Purbhoo, Stefanie Sowinski, Alistair N. Hume, Miguel C. Seabra, Mark A. A. Neil, Paul M. W. French, and Daniel M. Davis. Structurally distinct membrane nanotubes between human macrophages support long-distance vesicular traffic or surfing of bacteria. *The Journal of Immunology*, 177(12):8476–8483, 2006.
- [31] Haijiang Zhang, Shijun Xu, Gavin D.M. Jeffries, Owe Orwar, and Aldo Jesorka. Artificial nanotube connections and transport of molecular cargo between mammalian cells. *Nano Communication Networks*, 4(4):197 – 204, 2013.
- [32] Björn Nefel, Shlomo Nedvetzki, Kumiko Yanagi, and Daniel M. Davis. Cutting edge: Membrane nanotubes connect immune cells. *The Journal of Immunology*, 173(3): 1511–1513, 2004.
- [33] Langevin Christelle Marijanovic Zrinka Caputo Anna Browman Duncan T. Chenouard Nicolas de Chaumont Fabrice Martino Angelo Enninga Jost Olivo-Marin Jean-Christophe Mannel Daniela Zurzolo Chiara Gousset Karine, Schiff Edwin. Prions hijack tunnelling nanotubes for intercellular spread. *Nat Cell Biol*, 11:328–336, 2009.

- [34] Purbhoo Marco A. Chauveau Anne Kohler Karsten Oddos Stephane Eissmann Philipp Brodsky Frances M. Hopkins Colin Onfelt Bjorn Sattentau Quentin Davis Daniel M. Sowinski Stefanie. Jolly Clare, Berninghausen Otto. Membrane nanotubes physically connect t cells over long distances presenting a novel route for hiv-1 transmission. *Nat Cell Biol*, 10:211–219, 2008.
- [35] Michael I. Dorrell, Edith Aguilar, and Martin Friedlander. Retinal vascular development is mediated by endothelial filopodia, a preexisting astrocytic template and specific r-cadherin adhesion. *Investigative Ophthalmology Visual Science*, 43(11): 3500–3510, 2002.
- [36] Toshimi Shimizu, Mitsutoshi Masuda, and Hiroyuki Minamikawa. Supramolecular nanotube architectures based on amphiphilic molecules. *Chemical Reviews*, 105(4): 1401–1444, 2005.
- [37] R.E. Waugh, J. Song, S. Svetina, and B. Zeks. Local and nonlocal curvature elasticity in bilayer membranes by tether formation from lecithin vesicles. *Biophysical Journal*, 61(4):974 – 982, 1992.
- [38] B. Bozic, S. Svetina, B. Zeks, and R.E. Waugh. Role of lamellar membrane structure in tether formation from bilayer vesicles. *Biophysical Journal*, 61(4):963 – 973, 1992.
- [39] Volkmar Heinrich and RichardE. Waugh. A piconewton force transducer and its application to measurement of the bending stiffness of phospholipid membranes. *Annals of Biomedical Engineering*, 24(5):595–605, 1996.
- [40] Gerbrand Koster, Angelo Cacciuto, Imre Derényi, Daan Frenkel, and Marileen Dogterom. Force barriers for membrane tube formation. *Phys. Rev. Lett.*, 94: 068101, Feb 2005.
- [41] Gerbrand Koster, Martijn VanDuijn, Bas Hof, and Marileen Dogterom. Membrane tube formation from giant vesicles by dynamic association of motor proteins. *Proceedings of the National Academy of Sciences*, 100(26):15583–15588, 2003.
- [42] Jonathan West, Andreas Manz, and Petra S. Dittrich. Lipid nanotubule fabrication by microfluidic tweezing. *Langmuir*, 24(13):6754–6758, 2008.
- [43] Kumari Priti Sinha, Siddharth Gadkari, and Rochish M. Thaokar. Electric field induced pearling instability in cylindrical vesicles. *Soft Matter*, 9:7274–7293, 2013.
- [44] Josemar A Castillo, Daniel M Narciso, and Mark A Hayes. Bionanotubule formation from surface-attached liposomes using electric fields. *Langmuir : the ACS journal of surfaces and colloids*, 25(1):391396, January 2009.

- [45] Ernesto E. Ambroggio, James Sillibourne, Bruno Antonny, Jean-Baptiste Manneville, and Bruno Goud. Arf1 and membrane curvature cooperate to recruit arfaptin2 to liposomes. *PLoS ONE*, 8(4):e62963, 04 2013.
- [46] De Camilli Pietro Frost Adam, Unger Vinzenz M. The bar domain superfamily: Membrane-molding macromolecules. *Cell*, 137:191–196, 2009.
- [47] Shiro Suetsugu, Kiminori Toyooka, and Yosuke Senju. Subcellular membrane curvature mediated by the {BAR} domain superfamily proteins. *Seminars in Cell Developmental Biology*, 21(4):340 – 349, 2010.
- [48] Akihisa Yamamoto and Masatoshi Ichikawa. Direct measurement of single soft lipid nanotubes: Nanoscale information extracted in a noninvasive manner. *Phys. Rev. E*, 86:061905, Dec 2012.
- [49] Natalia Stepanyants, Haijiang Zhang, Tatsiana Lobovkina, Paul Dommersnes, Gavin D. M. Jeffries, Aldo Jesorka, and Owe Orwar. Spontaneous shape transformation of free-floating lipid membrane nanotubes. *Soft Matter*, 9:5155–5159, 2013.
- [50] Deuling, H.J. and Helfrich, W. The curvature elasticity of fluid membranes : A catalogue of vesicle shapes. *J. Phys. France*, 37(11):1335–1345, 1976.
- [51] I. Deryni, G. Koster, M.M. van Duijn, A. Czvek, M. Dogterom, and J. Prost. Membrane nanotubes. In Heiner Linke and Alf Mnsson, editors, *Controlled Nanoscale Motion*, volume 711 of *Lecture Notes in Physics*, pages 141–159. Springer Berlin Heidelberg, 2007.
- [52] Ulrich Schwarz and Gerhard Gompper. Bicontinuous surfaces in self-assembling amphiphilic systems. In Klaus Mecke and Dietrich Stoyan, editors, *Morphology of Condensed Matter*, volume 600 of *Lecture Notes in Physics*, pages 107–151. Springer Berlin Heidelberg, 2002.
- [53] D.P. Siegel and M.M. Kozlov. The gaussian curvature elastic modulus of n-monomethylated dioleoylphosphatidylethanolamine: Relevance to membrane fusion and lipid phase behavior. *Biophysical Journal*, 87(1):366 – 374, 2004.
- [54] Rumiana Dimova. Recent developments in the field of bending rigidity measurements on membranes. *Advances in Colloid and Interface Science*, 208(0):225 – 234, 2014. Special issue in honour of Wolfgang Helfrich.
- [55] Brochard, F. and Lennon, J.F. Frequency spectrum of the flicker phenomenon in erythrocytes. *J. Phys. France*, 36(11):1035–1047, 1975.

- [56] E. Evans and W. Rawicz. Entropy-driven tension and bending elasticity in condensed-fluid membranes. *Phys. Rev. Lett.*, 64:2094–2097, Apr 1990.
- [57] E.A. Evans. Bending elastic modulus of red blood cell membrane derived from buckling instability in micropipet aspiration tests. *Biophysical Journal*, 43(1):27 – 30, 1983.
- [58] Rumiana Dimova, Said Aranda, Natalya Bezlyepkina, Vesselin Nikolov, Karin A Riske, and Reinhard Lipowsky. A practical guide to giant vesicles. probing the membrane nanoregime via optical microscopy. *Journal of Physics: Condensed Matter*, 18(28):S1151, 2006.
- [59] W. Rawicz, K.C. Olbrich, T. McIntosh, D. Needham, and E. Evans. Effect of chain length and unsaturation on elasticity of lipid bilayers. *Biophysical Journal*, 79(1): 328 – 339, 2000.
- [60] Hung V. Ly, David E. Block, and Marjorie L. Longo. Interfacial tension effect of ethanol on lipid bilayer rigidity, stability, and area/molecule:a micropipet aspiration approach. *Langmuir*, 18(23):8988–8995, 2002.
- [61] Imre Derényi, Frank Jülicher, and Jacques Prost. Formation and interaction of membrane tubes. *Phys. Rev. Lett.*, 88:238101, May 2002.
- [62] Justin N. Walker P. A. Rittinger K. Gamblin S. J. Smerdon S. J. Tarricone C., Xiao B. The structural basis of arfaptin-mediated cross-talk between rac and arf signalling pathways. *Nature*, 411, 2001.
- [63] Brian J. Peter, Helen M. Kent, Ian G. Mills, Yvonne Vallis, P. Jonathan G. Butler, Philip R. Evans, and Harvey T. McMahon. Bar domains as sensors of membrane curvature: The amphiphysin bar structure. *Science*, 303(5657):495–499, 2004.
- [64] Guangyu Zhu, Jia Chen, Jay Liu, Joseph S Brunzelle, Bo Huang, Nancy Wakeham, Simon Terzyan, Xuemei Li, Zihe Rao, Guangpu Li, and Xuejun C Zhang. Structure of the appl1 bar-ph domain and characterization of its interaction with rab5. *The EMBO Journal*, 26(14):3484–3493, 2007.
- [65] Winfried Weissenhorn. Crystal structure of the endophilin-a1 {BAR} domain. *Journal of Molecular Biology*, 351(3):653 – 661, 2005.
- [66] Britta Qualmann, Dennis Koch, and Michael Manfred Kessels. Let’s go bananas: revisiting the endocytic bar code. *The EMBO Journal*, 30(17):3501–3515, 2011.
- [67] Toshiki Itoh, Kai S. Erdmann, Aurelien Roux, Bianca Habermann, Hauke Werner, and Pietro De Camilli. Dynamin and the actin cytoskeleton cooperatively regulate

- plasma membrane invagination by {BAR} and f-bar proteins. *Developmental Cell*, 9(6):791 – 804, 2005.
- [68] Atsushi Shimada, Hideaki Niwa, Kazuya Tsujita, Shiro Suetsugu, Koji Nitta, Kyoko Hanawa-Suetsugu, Ryogo Akasaka, Yuri Nishino, Mitsutoshi Toyama, Lirong Chen, Zhi-Jie Liu, Bi-Cheng Wang, Masaki Yamamoto, Takaho Terada, Atsuo Miyazawa, Akiko Tanaka, Sumio Sugano, Mikako Shirouzu, Kuniaki Nagayama, Tadaomi Takenawa, and Shigeyuki Yokoyama. Curved efc/f-bar-domain dimers are joined end to end into a filament for membrane invagination in endocytosis. *Cell*, 129(4):761 – 772, 2007.
- [69] Ford Marijn G.J. Hegde Balachandra G. Daumke Oliver Butler P. Jonathan G. Mittal Rohit Langen Ralf Evans Philip R. McMahon Harvey T. Henne William Mike, Kent Helen M. Structure and analysis of fcho2 f-bar domain: A dimerizing and membrane recruitment module that effects membrane curvature. *Structure*, 15: 839–852, 2007.
- [70] Adam Frost, Rushika Perera, Aurlien Roux, Krasimir Spasov, Olivier Destaing, Edward H. Egelman, Pietro De Camilli, and Vinzenz M. Unger. Structural basis of membrane invagination by f-bar domains. *Cell*, 132(5):807 – 817, 2008.
- [71] Sung Haeng Lee, Frederic Kerff, David Chereau, Francois Ferron, Alexandra Klug, and Roberto Dominguez. Structural basis for the actin-binding function of missing-in-metastasis. *Structure*, 15(2):145 – 155, 2007.
- [72] Akiko Yamagishi, Michitaka Masuda, Takashi Ohki, Hirofumi Onishi, and Naoki Mochizuki. A novel actin bundling/filopodium-forming domain conserved in insulin receptor tyrosine kinase substrate p53 and missing in metastasis protein. *Journal of Biological Chemistry*, 279(15):14929–14936, 2004.
- [73] Joern Linkner, Gregor Witte, Hongxia Zhao, Alexander Junemann, Benjamin Nordholz, Petra Runge-Wollmann, Pekka Lappalainen, and Jan Faix. The inverse bar-domain protein ibara drives membrane remodelling to control osmoregulation, phagocytosis and cytokinesis. *Journal of Cell Science*, 2014.
- [74] Pieta K. Mattila, Anette Pykkinen, Juha Saarikangas, Ville O. Paavilainen, Helena Vihinen, Eija Jokitalo, and Pekka Lappalainen. Missing-in-metastasis and irsp53 deform pi(4,5)p2-rich membranes by an inverse bar domainlike mechanism. *The Journal of Cell Biology*, 176(7):953–964, 2007.
- [75] Lappalainen Pekka Mattila Pieta K. Filopodia: molecular architecture and cellular functions. *Nat Rev Mol Cell Biol*, 9:446–454, 2008.

- [76] Veronika Kralj-Igli, Gregor Gomek, Janja Majhenc, Vesna Arrigler, and Saa Svetina. Myelin-like protrusions of giant phospholipid vesicles prepared by electroformation. *Colloids and Surfaces A: Physicochemical and Engineering Aspects*, 181(13):315 – 318, 2001.
- [77] Yu-Cheng Lin, Keng-Shiang Huang, Jen-Ta Chiang, Chih-Hui Yang, and Tzung-Heng Lai. Manipulating self-assembled phospholipid microtubes using microfluidic technology. *Sensors and Actuators B: Chemical*, 117(2):464 – 471, 2006.
- [78] F. Campelo and A. Hernández-Machado. Model for curvature-driven pearling instability in membranes. *Phys. Rev. Lett.*, 99:088101, Aug 2007.
- [79] Ilan Tsafir, Dror Sagi, Tamar Arzi, Marie-Alice Guedeau-Boudeville, Vidar Frette, Daniel Kandel, and Joel Stavans. Pearling instabilities of membrane tubes with anchored polymers. *Phys. Rev. Lett.*, 86:1138–1141, Feb 2001.
- [80] Clifford P. Brangwynne, Gijsje H. Koenderink, Ed Barry, Zvonimir Dogic, Frederick C. MacKintosh, and David A. Weitz. Bending dynamics of fluctuating biopolymers probed by automated high-resolution filament tracking. *Biophysical Journal*, 93(1):346 – 359, 2007.
- [81] F Gittes, B Mickey, J Nettleton, and J Howard. Flexural rigidity of microtubules and actin filaments measured from thermal fluctuations in shape. *The Journal of Cell Biology*, 120(4):923–934, 1993.
- [82] Paul J. Hagerman. Flexibility of dna. *Annual Review of Biophysics and Biophysical Chemistry*, 17(1):265–286, 1988.
- [83] Shen Tian Huang Xiaolei Yusuf Eddy Vavylonis Dimitrios Smith Matthew B., Li Hongsheng. Segmentation and tracking of cytoskeletal filaments using open active contours. *Biophysical Journal*, 100(3):445a, 2011.
- [84] H. Felgner, R. Frank, and M. Schliwa. Flexural rigidity of microtubules measured with the use of optical tweezers. *Journal of Cell Science*, 109(2):509–516, 1996.
- [85] Paul J. Hagerman. Flexibility of dna. *Annual Review of Biophysics and Biophysical Chemistry*, 17:265–286, 1988.
- [86] A. Ott, M. Magnasco, A. Simon, and A. Libchaber. Measurement of the persistence length of polymerized actin using fluorescence microscopy. *Phys. Rev. E*, 48:R1642–R1645, Sep 1993.
- [87] S Nader S Reihani, Shahid A Mir, Andrew C Richardson, and Lene B Oddershede. Significant improvement of optical traps by tuning standard water immersion objectives. *Journal of Optics*, 13(10):105301, 2011.

- [88] Laura R. Arriaga, Iván López-Montero, Guillermo Orts-Gil, Bela Farago, Thomas Hellweg, and Francisco Monroy. Fluctuation dynamics of spherical vesicles: Frustration of regular bulk dissipation into subdiffusive relaxation. *Phys. Rev. E*, 80: 031908, Sep 2009.
- [89] Ana J. Garca-Sez, Salvatore Chiantia, Jess Salgado, and Petra Schwille. Pore formation by a bax-derived peptide: Effect on the line tension of the membrane probed by afm. *Biophysical Journal*, 93(1):103 – 112, 2007.
- [90] Cascades of transient pores in giant vesicles: Line tension and transport. *Biophysical Journal*, 84(3):1734 – 1749, 2003.
- [91] Benoit Sorre, Andrew Callan-Jones, Jean-Baptiste Manneville, Pierre Nassoy, Jean-Francois Joanny, Jacques Prost, Bruno Goud, and Patricia Bassereau. Curvature-driven lipid sorting needs proximity to a demixing point and is aided by proteins. *Proceedings of the National Academy of Sciences*, 2009.
- [92] Hernan Zhou, Beatriz Burrola Gabilondo, Wolfgang Losert, and Willem van de Water. Stretching and relaxation of vesicles. *Phys. Rev. E*, 83:011905, Jan 2011.
- [93] Hlne Bouvrais, Philippe Mlard, Tanja Pott, Knud J. Jensen, Jesper Brask, and John H. Ipsen. Softening of {POPC} membranes by magainin. *Biophysical Chemistry*, 137(1):7 – 12, 2008.
- [94] Juha Saarikangas, Hongxia Zhao, Anette Pykkinen, Pasi Laurinmki, Pieta K. Mattila, Paavo K.J. Kinnunen, Sarah J. Butcher, and Pekka Lappalainen. Molecular mechanisms of membrane deformation by i-bar domain proteins. *Current Biology*, 19(2):95 – 107, 2009.
- [95] Vaggi F, Disanza A, Milanese F, Di Fiore PP, Menna E, Matteoli M, Gov NS, Scita G, and Ciliberto A. The eps8/irsp53/vasp network differentially controls actin capping and bundling in filopodia formation. *PLoS Comput Biol*, 7(7):e1002088, 2011.
- [96] Raktim Dasgupta and Rumiana Dimova. Inward and outward membrane tubes pulled from giant vesicles. *Journal of Physics D: Applied Physics*, 47(28):282001, 2014.
- [97] Rob Phillips, Jane Kondev, and Julie Theriot. *Physical biology of the cell*. Garland Science, 2009.
- [98] Henrik Flyvbjerg Kirstine Berg-Srensen Poul Martin Hansen, Iva Marija Tolic-Nrrelykke. tweezercalib 2.1: Faster version of matlab package for precise calibration of optical tweezers. *Computer Physics Communications*, 175(8):572 – 573, 2006.

Chapter 8

Articles

- FBAR syndapin 1 recognizes and stabilizes highly curved tubular membranes in a concentration dependent manner
- Fluorescent quantification of size and lamellarity of membrane nanotubes



FBAR Syndapin 1 recognizes and stabilizes highly curved tubular membranes in a concentration dependent manner

Pradeep Ramesh¹, Younes F. Baroji^{1,2}, S. Nader S. Reihani^{1,3}, Dimitrios Stamou^{4,5}, Lene B. Oddershede^{1,5} & Poul Martin Bendix¹

¹Niels Bohr Institute, University of Copenhagen, Blegdamsvej 17, 2100 Copenhagen, Denmark, ²Department of Physics, Institute for Advanced Studies in Basic Sciences (IASBS), Zanjan 45137-66731, Iran, ³Department of Physics, Sharif University of Technology, PO BOX 11365-9161 Tehran, Iran, ⁴Bionanotechnology and Nanomedicine Laboratory, Department of Chemistry, Nano-Science Center, University of Copenhagen, Universitetsparken 5, 2100 Copenhagen, Denmark, ⁵Lundbeck Foundation Center of Excellence for Biomembranes in Nanomedicine.

Syndapin 1 FBAR, a member of the Bin-amphiphysin-Rvs (BAR) domain protein family, is known to induce membrane curvature and is an essential component in biological processes like endocytosis and formation and growth of neurites. We quantify the curvature sensing of FBAR on reconstituted porcine brain lipid vesicles and show that it senses membrane curvature at low density whereas it induces and reinforces tube stiffness at higher density. FBAR strongly up-concentrates on the high curvature tubes pulled out of Giant Unilamellar lipid Vesicles (GUVs), this sorting behavior is strongly amplified at low protein densities. Interestingly, FBAR from syndapin 1 has a large affinity for tubular membranes with curvatures larger than its own intrinsic concave curvature. Finally, we studied the effect of FBAR on membrane relaxation kinetics with high temporal resolution and found that the protein increases relaxation time of the tube holding force in a density-dependent fashion.

Proteins containing BAR domains that can either sense or generate curvature on phospholipid membranes are associated with cellular sites where severe bending of membranes takes place. Working in tandem with a panoply of other host proteins, BAR domain proteins appear to play a crucial role in cellular cargo trafficking through coordinated membrane and cytoskeletal remodeling¹⁻³. Consequently, they influence a vast array of physiological activities ranging from T-tubule formation in muscle cells to neuromorphogenesis¹. In addition, their malfunction is implicated in diseases such as bladder carcinoma, Alzheimer's, and Huntington's, as well as cancer progression⁴.

Bar domains belonging to a variety of proteins have been shown to detect membrane morphologies that have a tubular or spherical shape⁵⁻¹³. In an experimental assay where a membrane tube is pulled out of a GUV the membrane bound proteins are allowed to freely diffuse between the low curvature compartment (the GUV) and the highly-curved tube, thus mimicking the curvature landscape and connected membrane structures displayed in cells. Proteins containing NBAR domains were shown to up-concentrate on tubular membranes with curvatures that strongly correlated with the BAR domain's high intrinsic curvature^{9,11,13,14}. Besides having a concave side, with cationic residues that bind to negatively charged membranes, NBAR domains are also equipped with N-terminal hydrophobic helices which insert into membranes upon binding. These N-terminal helices are implicated in membrane deformation² and were found to sense membrane curvature in liposomal assays⁷.

FBAR domains, however, are less curved than NBAR domains, and a variety of proteins containing FBAR domains are commonly associated with a range of biological processes where membrane remodeling takes place^{1,3,15,16}. The molecular domain curvature differs among the various known species of FBARs with differences in both the degree and the dimensionality of the curvature³. In addition, electron micrographs of FBAR domains highlight their ability to self-arrange in an assortment of lattice configurations¹⁷, thus enabling them to aggregate on membranes whose curvatures are higher than the concave curvature of the FBAR domain itself¹⁶. Interestingly, the FBAR domain of syndapin 1 has a distinctly unique shape when compared to other types of bar domains.

SUBJECT AREAS:
MEMBRANE BIOPHYSICS
ENDOCYTOSIS
MOLECULAR NEUROSCIENCE
NANOSCALE BIOPHYSICS

Received
31 January 2013

Accepted
14 March 2013

Published
28 March 2013

Correspondence and requests for materials should be addressed to P.M.B. (bendix@nbi.dk)



Besides having a shallow curvature on its concave side, the tips of the FBAR domain also point away from the central (long) axis of the protein, giving it a characteristic tilde-shape¹⁶. Due to this pronounced two dimensional curvature, syndapin 1 can constrict membranes into tubules having a range of curvatures¹⁶ thus giving it an important role in a host of biological functions. Unlike NBAR, syndapin 1 contains two wedge loops that can insert into the hydrophobic region of the bilayer which seem to be critical for its tube forming ability¹⁸.

Sensing of membrane curvatures by the FCHo2 FBAR domain was reported in both a single liposome assay and in a bulk assay with conflicting results^{7,19}. The shallow molecular curvature of the FBAR domain's concave side does not necessarily dictate its sensing behavior, since it could bind at an oblique angle to the tube axis¹⁶, or binding could be dominated by membrane insertions of hydrophobic residues displayed on the concave side of the BAR domain^{5,7}.

To quantify syndapin's curvature sensing behavior, we pulled a membrane nanotube, with controlled diameter, out of a GUV using an optical trap while simultaneously imaging the protein density on the tube and the GUV by confocal fluorescence microscopy. Interestingly, we found an increased sensing of membrane curvature even when the membrane curvature exceeded the protein's intrinsic curvature. By performing force spectroscopy using a photodiode detection system with high temporal resolution of 45 μ s, we measured the relaxation behavior of the tube holding force in response to a rapid elongation of the tube. We demonstrate that binding of syndapin affects the relaxation behavior of the pulled tube after rapid elongation, hence, the BAR domains have a mechanical effect on the tube, even at relatively low FBAR concentrations. This conclusion was supported by conducting fluctuation analysis of the thermal motion of free membrane tubes showing that tubes formed in presence of FBAR domains were thinner but still stiffer than spontaneously formed membrane tubes without proteins bound.

Results

Curvature assay. We used an SH3 mutant FBAR domain of syndapin 1 which efficiently binds and deforms membranes but is not autoinhibited by the SH3 domain²⁰. The curvature preference of the protein was investigated using membrane nanotubes of variable radii that were pulled out of GUVs held by a suction pipette (see Fig. 1a). The suction pressure was used to regulate the membrane tension thus controlling tube radius²¹. By measuring the tube/GUV intensity ratio versus aspiration pressure we obtained a calibration curve (see Fig. S1 and eq. S1–S2). This ratio was then used in all

subsequent measurements to deduce the tube radius from the tube/GUV intensity ratio using a curvature insensitive membrane dye.

The length of the aspirated membrane tongue inside the pipette is proportional to the applied suction pressure and the GUV acts as a reservoir of lipids and proteins. We performed experiments with both artificial lipid mixtures (DOPC:DOPG 3:1) as well as with GUVs made from porcine brain lipid extracts. Fig. 1b shows an overlay of the membrane (red) and protein (white) channels and illustrates syndapin's strong preference for high curvatures (small tube radii) on tubes made from brain lipid extracts. To illustrate the relative tube/GUV intensities of the membrane and protein channel, the intensities of the two respective channels are plotted in Fig. 1c,d as surface plots. The membrane signal of the tube is slightly above background (Fig. 1d), as opposed to the tube's protein signal, which is equivalent to that on the GUV (Fig. 1c), thus showing that the protein has a strong preference for the tube.

Upon gentle aspiration of GUVs decorated with FBAR, membrane tethers were pulled by translating the GUV and micropipette away from the optically trapped particle using a piezo-electric stage controller. The pulling force and the suction system were allowed to briefly equilibrate before initiating confocal acquisition of the membrane and protein channels. Aspiration pressure was then slowly varied, thus effecting a change in tube diameter according to the well-known Laplace relation (see supplementary information, eq. S1–S2). In this manner, we were able to explore a physiologically relevant range of tube diameters, and explicitly quantify protein sorting between the tube and the GUV reservoir as a function of tube diameter and bound density.

Syndapin 1 senses curvature on artificial and brain lipid GUVs. To quantitatively evaluate the sensing characteristics of the FBAR of syndapin 1 we measured the relative density of FBAR on tubes of a range of radii as a function of bulk protein concentration. The protein density on tubes is measured relative to the density on the GUVs and is expressed as a *Sorting* number, according to eq. 1, where *Sorting* = 2 means that the density is two-fold higher on the tube than on the GUV. *Sorting* is defined as

$$\text{Sorting} = \frac{1}{PCF} \frac{(I_{\text{protein}}/I_{\text{membrane}})_{\text{tube}}}{(I_{\text{protein}}/I_{\text{membrane}})_{\text{GUV}}}, \quad (1)$$

where *PCF* is a polarization dependent correction factor which arises due to the polarization dependence of the membrane incorporated fluorophore²². The bound protein density is itself contingent on a host of factors, namely bulk salt and protein concentration, as well as

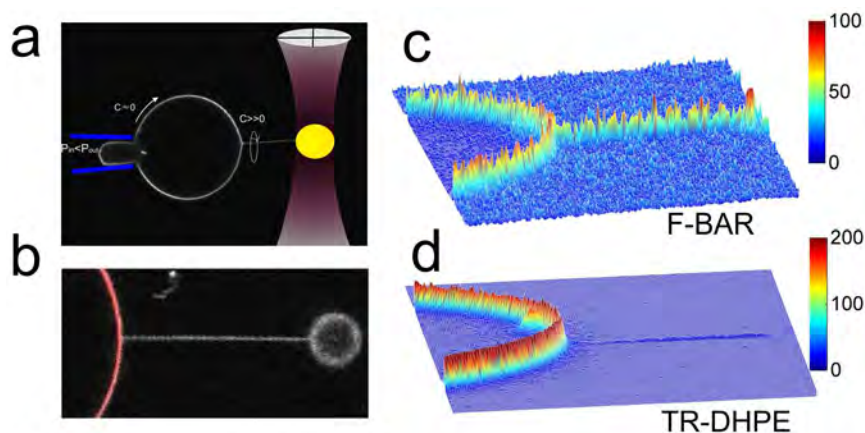


Figure 1 | Assay for testing the curvature preference of syndapin 1. (a) A high curvature brain lipid tube is extracted from a Giant Unilamellar Vesicle (GUV) using optical tweezers. The figure is a composite of a raw data image of the GUV and drawings of the pipette, optical tweezers and the photodiode detection system. (b) Fluorescence intensity is collected from two channels: the membrane channel (red) and the fluorescent FBAR channel (white). The image is an overlay of these two channels showing a significant up-concentration of FBAR on the highly curved tube. (c) and (d) show intensity plots of the FBAR and the TR-DHPE membrane dye, respectively, for a segment of the GUV and the tube.



membrane composition, to name a few parameters that can be macroscopically tuned. The sorting versus radius for the artificial mixture is plotted in Fig. 2a and clearly shows a high affinity of FBAR for thin tubes. Also, partitioning of the proteins for the tube was strongly dependent on the bulk concentration of FBAR. For 50 nM FBAR we measured up to 10–15 fold higher density on the tubes whereas for 500 nM FBAR the sorting was severely attenuated to approximately 2–3. This sorting behavior was measured for both the synthetic mixture in Fig. 2a as well as for the more natural composition of the brain lipid system, Fig. 2b. Similar density dependent sorting was observed for NBAR proteins on the same kind of GUV/tube system made of similar synthetic lipid mixture as shown in Fig. 2a^{11,13} and was attributed to crowding effects at high density.

It is evident from Fig. 2 that the result of changing the membrane composition is not dramatic. However, this is not trivial as the brain lipid mixture and may contain additional lipid species, such as phosphoinositides and other negatively charged lipids that facilitate binding of the FBAR domain to the membrane. Hence, experiments can be performed even at high ionic strength on brain lipid extracts. We did observe a similar sorting profile near physiological salt concentrations using brain lipid GUVs (see Supplementary Information, Fig. S2). Our observation that syndapin 1 is able to sense high curvatures with strong affinities even at near physiological salt concentrations (100 mM) suggests that curvature sensing is indeed a very pronounced and fundamental property of this protein.

Notably, in experiments with high protein concentration (500 nM) in bulk but with lipid mixtures that have lower charge density, and hence a very low affinity of FBAR for the GUV membrane, we observed high density on the tube relative to the GUV (see Fig. S3 and movie 1). This experiment shows that even at high solution concentrations the sorting efficiency can be high as long as the density on the membrane is kept low to avoid effects of crowding.

As a control for the curvature sensing of another protein, we added fluorescently labeled streptavidin (STP) to the GUVs and subsequently formed membrane tubes from the streptavidin coated GUVs⁷, see Fig. S4 for two examples. Strong sensing was not observed for high curvature tubes, $R = 18$ nm, neither for $[STP] = 500$ nM nor for $[STP] = 10$ nM. Only residual up-concentrations of 1.9 and 1.5 of streptavidin on the tubes were measured for these two concentrations.

BAR domains have been reported to oligomerize into ordered lattices on tubes^{16,23}. We do not expect any such effects at the low

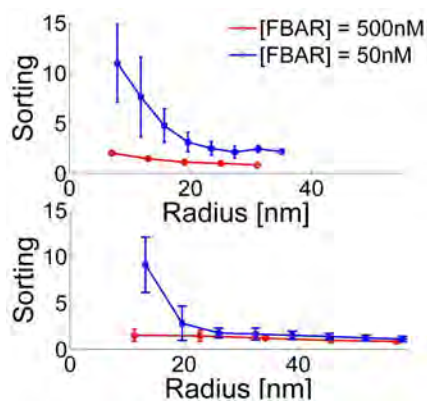


Figure 2 | FBAR sorting depends on membrane curvature and protein concentration. (a) FBAR binding to tubes made of a synthetic lipid mixture (25 mol% DOPG and 74 mol% DOPC). (b) Curvature sensing on tubes of brain lipid extracts. In both (a) and (b) the sorting is measured at protein concentrations of 50 nM (blue squares) and 500 nM (red circles). Data were collected from 17 GUVs in 11 experiments. Error bars denote the standard deviations of the data points within the bin intervals.

concentration where we observe the strongest sensing, since the molecular density on the membrane is low. To assess the mobility of the membrane bound protein at an initial 500 nM solution concentration, we performed fluorescence recovery after photobleaching (FRAP) experiments on both the GUV and the tube, see Fig. S5a and b. The FBAR domains on the GUV rapidly recovered to the initial unbleached value Fig. S5b (green circles), whereas the recovery on the tube (blue diamonds) was slower and only partial within the timescale of the experiment. The protein on the membrane tube diffused to recover the bleached area with a diffusion coefficient of $D = 0.6 \mu\text{m}^2/\text{s}$, as shown in Fig. S5c. This provides an upper limit for the mobility on the tube since we cannot exclude the possible exchange of protein with the solution phase. However, we see that the recovery proceeds from the GUV reservoir towards the trapped particle thus confirming diffusive mixing with the GUV. We therefore only expect minimal exchange with the solution phase on the timescale of the FRAP experiment. Despite the protein mobility, we still observe a mechanical effect due to the protein on the bilayer when the membrane tension is suddenly decreased as shown in Fig. S6. A decrease in aspiration pressure does not immediately increase the tube diameter. Instead, the excess area results in an increase of the tube length, and the tube bends out of the focal plane of the

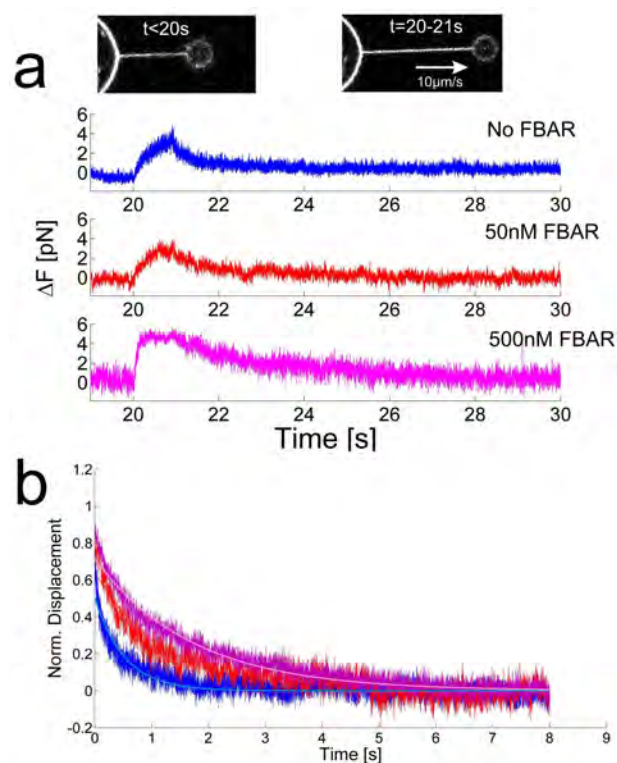


Figure 3 | Relaxation kinetics of tube restoring force after a $10 \mu\text{m}$ step elongation in the presence or absence of FBAR. The elongation is performed at $10 \mu\text{m}/\text{s}$ and the position of the particle is recorded with 45 μs time resolution. (a) Force versus time relaxation behavior of the force ΔF shown for three different concentrations of FBAR. Prior to elongation of the tether the force, F , equals the equilibrium holding force, F_h , of the short tether and $\Delta F = F - F_h = 0$. After elongation ΔF at different protein concentrations relaxes back to zero. Inset, images of GUV and tube before and after elongation (images are contrast enhanced for visibility). (b) Superimposed average relaxation behavior of a number of experiments. Experiments are performed at 500 nM (magenta, average of 8 experiments), 50 nM (red curve, average of 6 experiments) and in absence of FBAR (blue curve, average of 8 experiments). The exponential relaxation time, τ , increases with FBAR concentration with $\tau_{0 \text{ nM}} = 0.52 \pm 0.01$ s, $\tau_{50 \text{ nM}} = 1.20 \pm 0.02$ s, $\tau_{500 \text{ nM}} = 1.71 \pm 0.01$ s.



microscope (Fig. S6). This strongly implies that the protein influences the curvature elasticity of the bilayer.

Membrane relaxation depends on protein concentration. The mechanical effect of syndapin 1 on the membrane was investigated by performing a fast elongation of the tube while subsequently measuring the relaxation behavior of the force to equilibrium, see Fig. 3a. The bulk protein concentration in these experiments was held constant at 0 nM, 50 nM or 500 nM and we quantified the stabilizing effect of the protein through the decay constant of the force relaxation.

To assess the fast relaxation kinetics of elongated tethers in the presence or absence of FBAR, we measured the force, F , exerted by the optical trap during and after the rapid tether elongation, as shown in Fig. 3. The position of the particle and the force, F , was continuously monitored at 22 kHz using a photodiode detection scheme^{24,25}. The optical trap was calibrated to find the spring constant κ by characterizing the harmonic trapping potential, using power spectral analysis of the particle's Brownian motion in the trap²⁶, see Fig. S7. The force, F , was then obtained as the displacement of the trapped particle from the trap center, Δx , times the trapping constant κ , $F = \kappa \Delta x$. The particle was brought into contact with the GUV, a short tube of 5 μm was pulled slowly, and subsequently the tube length was then rapidly extended by 10 μm at a velocity of 10 $\mu\text{m/s}$.

Figures 3a and 3b summarize the results of the force kinetics experiments. The effect of FBAR on tube relaxation kinetics can be quantified as the relaxation rates of the decaying force or displacement which are $\tau_{0 \text{ nM}} = 0.52 \pm 0.01 \text{ s}$, $\tau_{50 \text{ nM}} = 1.20 \pm 0.02 \text{ s}$, and $\tau_{500 \text{ nM}} = 1.71 \pm 0.01 \text{ s}$ respectively, see Fig. 3b. The relaxation of the force in the absence of FBAR occurs within hundreds of milliseconds, consistent with relaxation dynamics in lipid bilayers^{27,28}. In the presence of FBAR, the relaxation time increases in a concentration dependent manner. The increased relaxation, which can be observed at a concentration of 50 nM (see Fig. 3) may reflect reorganization of the protein on the tube which occurs slower at higher concentrations when the proteins are in a crowded environment. The increased relaxation times at concentrations as low as 50 nM shows that FBAR from syndapin 1 has a mechanical effect on tubes at concentrations well below 8 μM at which tubulating activity of the protein was observed¹⁶.

Syndapin 1 stiffens tubes at high density. At higher FBAR concentrations one might expect to see an increased rigidity of the tube caused by the onset of intermolecular contacts between adjacent FBAR dimers along the tube surface as supported by previous findings of FBAR lattice formation using electron microscopy¹⁶. Oligomerization of BAR domains on tubes can influence the rigidity of tubes by forming a lattice like structure on the tube surface. The laterally contiguous protein shell can significantly stiffen the tube in the case of strong intermolecular contacts as observed on NBAR and FBP17 FBAR domains¹⁷.

Based on crystallography, it has been suggested that FBAR from syndapin 1 forms rather weak intermolecular interactions on tubes formed in presence of high concentrations of syndapin 1¹⁶. We tested this by comparing the persistence lengths of tubes containing syndapin 1 with lipid tubes containing no protein. Tubes composed of 25 mol% DOPG and 73 mol% POPC and 2 mol% TR-DHPE were formed by incubation of high concentrations of syndapin 1 with GUVs. Tubes containing no protein were simply formed by gentle hydration of a lipid film that is normally used to form GUVs, but also spontaneously forms tubes^{29,30}. To keep the tubes within the focal plane of the microscope, the tube assay was conducted inside a quasi-two dimensional chamber with a height of ca. 2–5 μm that was deduced from laser reflection at the water/glass interfaces³¹.

The persistence length, L_p , of lipid tubes is a function of the membrane bending rigidity, κ , and tube radius, R ³²,

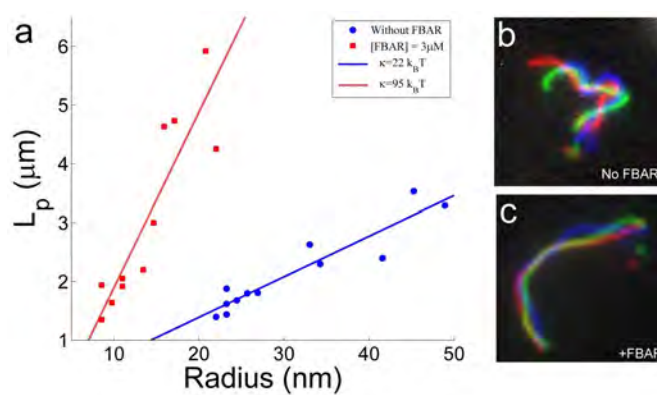


Figure 4 | Membrane tubes decorated with FBAR are stiffer than tubes without FBAR. (a) The persistence length for tubes formed at high concentrations of FBAR (red squares, 11 tubes) and bare tubes (blue circles, 12 tubes) formed by gentle hydration. (b + c) Examples of tubes having similar sizes but different stiffness as a result of binding by FBAR. The colors represent different time points separated by 884 ms. (b) No FBAR, $R = 24 \text{ nm}$ and $L_p = 1.7 \mu\text{m}$. (c) Incubated with 3 μM FBAR, $R = 22 \text{ nm}$ and $L_p = 4.3 \mu\text{m}$. The images are 13 $\mu\text{m} \times 13 \mu\text{m}$.

$$L_p = \frac{\pi R \kappa}{k_B T}, \quad (2)$$

where $\kappa = 24 k_B T$ is the bending rigidity for POPC membranes³³. We used this expression to calibrate the tube radius. Unilamellarity of tubes can be assumed when tubes are formed by adding syndapin 1 to GUVs since these tubes are formed from mostly unilamellar vesicle, therefore, the intensity scales linearly with the tube radius. Tubes formed spontaneously by gentle hydration can be multilamellar which would add uncertainty to the size determination. According to eq. 2, unilamellar tubes having a persistence length of $\sim 1\text{--}2 \mu\text{m}$ would have radii of $\sim 20\text{--}30 \text{ nm}$, see blue line in Fig. 4a. If these tubes were multilamellar it would imply that the tubes were even thinner since otherwise the persistence lengths would be larger than $\sim 1\text{--}2 \mu\text{m}$. We consider it unlikely that tubes formed spontaneously would both have radii below 20 nm and be multilamellar due to the high energy of bending of multilayered membranes. We measured the persistence lengths of several tubes having similar intensity, and hence similar thicknesses, thus providing an estimate of the radius, R , of the tube. Since the intensity scales linearly with radius, we could infer the radius for any tube by measuring the intensity of the membrane dye.

Consistent with the theoretical prediction of eq. 2, we measured a linear dependence of L_p on R for POPC-DOPG membrane tubes, as shown in Fig. 4 (blue circles). Using linear regression we obtained a bending rigidity of the membrane of $\kappa = 22 k_B T$ that is consistent with the value of $\kappa = 24 k_B T$ as measured for POPC membranes³³.

The red squares in Fig. 4 denote the persistence length of FBAR tubes of various diameters. By linear fitting of eq. 2 to the data, we find that the bending rigidity of the tubular surface has increased by nearly five fold to $\kappa = 95 k_B T$. Hence tubes formed in presence of syndapin 1 are clearly stiffer than bare lipid tubes. The effect of FBAR on tube stiffness is illustrated in Fig. 4b and Fig. 4c in which two tubes having similar sizes are plotted at three different time points represented by three different colors. The tube in Fig. 4b contains no syndapin 1 and shows strong deflections. The tube in Fig. 4c, formed in presence of 3 μM syndapin 1, however, appears much more straight.

Discussion

Knowledge about the mechanical effect and curvature sensing ability of pascin 1/syndapin 1 is limited. Previous work has shown that



syndapin 1, unlike other proteins containing NBAR or other types of FBAR domain, does not form tubes having specific diameters that correlate with the intrinsic BAR domain curvature^{16,20}. A remarkable feature of syndapin 1 is its ability to generate a range of curvatures going well above its own intrinsic concave curvature. In cells, syndapin 1 has been associated with narrow tubes at late stages of endocytosis through its interactions with mechanoenzymes such as dynamin which is known to bind to full length syndapin and relieve it from its SH3-clamped configuration²⁰.

We show here that the sensing of membrane curvature by syndapin 1 persists for curvatures above its intrinsic radius of curvature (~ 21 nm³⁴) of its concave face, see Fig. 2 and Fig. S8. The sorting efficiency of FBAR continues to increase with curvature down to a tube diameter of 10–15 nm (Fig. 2). Previous work has revealed that FBAR of syndapin 1 exhibits a pronounced two dimensional curvature, allowing the domain to adopt various configurations on tubes depending on the tube radius¹⁶. Syndapin 1 exhibits a lateral curvature with the tip regions bent away from the central body by as much as 61°¹⁶, which could explain its affinity for a range of curvatures including curvatures higher than the curvature of the concave face of the BAR, see Fig. S8. Moreover, syndapin 1 contains two wedge loops that are essential for the tubulating activity of the protein and could influence its sensing ability by the favored insertion of the hydrophobic loops into highly curved membranes. Sensing of another less curved FBAR (FCHo2) was reported to be enriched on small lipid vesicles, with radii down to 50 nm, by a factor of ~ 30 . This effect was attributed to sensing by the hydrophobic part and not to the shape of the BAR domain⁷. The wedge loops on syndapin 1 are located near the distal ends of the, almost straight, central part of the protein (see Fig. S8a)¹⁶. Binding at an oblique angle would increase the alignment between the central part of the protein with the axis of the tube. This would lead to greater proximity between the membrane and the wedge loops, and therefore more efficient insertion of the loops into the membrane. The enrichment we measured on tubes reached 10–15 times the density on the GUV and occurred at radii down to 10–15 nm, see Fig. 2. Tubular systems pulled out of GUVs differ from lipid vesicles by having two different principal curvatures, a nonzero curvature along the azimuthal direction, and zero curvature along the tube, whereas the principal curvature of lipid vesicles are equal which could affect the curvature sensing of proteins. Also, tubes extracted from GUVs are in diffusive contact with a zero curvature membrane reservoir (GUV) thus allowing the proteins to redistribute between regions having different membrane curvature thus mimicking the membrane structures observed in endocytosis and the golgi network.

Similar results for curvature sensing, as observed here, have been obtained with NBAR domains from amphiphysin by using a similar tube/GUV assay^{11,13,14}. The binding of NBAR was strongly curvature dependent at low protein concentrations and was strongly attenuated at higher densities. In ref.11 the highest sorting ratio exceeded 80 at low protein density and equaled approximately 15 at higher densities. We observed a similar strong density dependence of the sorting behavior in Fig. 2a,b where the protein concentration in solution was changed by a factor of 10. NBARs are highly curved domains with a radius of curvature of ca. 11 nm and contain N-terminal α -helices that insert into bilayers; these are two factors that could make NBAR a more efficient curvature sensor of highly curved membranes compared to the FBAR domain of syndapin 1.

Mechanical effects imposed by BAR proteins on membrane tubes have been shown for NBARs and other FBAR domain proteins^{11,17}. Notably, tubes formed by the FBAR FBP17 were measured to have a persistence length of 142 μ m, much stiffer than the helical coat formed by dynamin which has $L_p = 37$ μ m¹⁷. NBARs were measured to have much shorter persistence lengths of ca. 10 μ m¹⁷. However, despite the importance of the tube diameter in these measurements, no correlation with tube diameter was given in the above references.

We measured a persistence length ranging from ca. 1.5 μ m to 6 μ m for tube radii between 10 nm and 25 nm, see Fig. 4a. Comparing the measured persistence lengths, in presence of FBAR, with persistence lengths of tubes in absence of FBAR we get a 5-fold increase in the tube stiffness which we attribute to the protein coat constituted by syndapin 1. This relatively weak stiffening by syndapin FBAR when compared to other FBARs and NBAR reported in Ref. 17 indicates that FBARs from syndapin 1 adopt a more labile higher order molecular arrangements on tubes as suggested in Ref. 16.

The mechanical effect of syndapin 1 was also quantified at lower concentrations (50 nM and 500 nM) by performing step elongation experiments and by measuring the kinetic force response in the holding force, as shown in Fig. 3. We observed an increase in relaxation time in presence of FBAR when compared to protein free tubes reflecting a change in the elastic response of the GUV/tube system. It is evident from Fig. 3 that the proteins act to stabilize the tube and make it less elastic. This mechanical effect is even present at 50 nM FBAR (Fig. 3, red curves). The dynamic increase in the membrane tension caused by rapid elongation relaxes within hundreds of milliseconds (see Fig. 3a), whereas the relaxation in the presence of protein is significantly slower, as seen in Fig. 3b,c. This slow down of relaxation with increasing concentrations of protein shows that crowding effects could restrict reorganization of the protein on the tube. The time dependent change in the holding force reflects the effect of the protein on the bending energy, κ , of the bilayer as can be seen from eq. S3 and eq. S4 in Supplementary Information. The stiffening of the tubes measured in Fig. 4 on the other hand reflects lateral stiffening of the tube due to the dense coat of protein on the tube surface and could originate from weak lateral interactions between the FBAR domains as reported in¹⁶. The time dependent change in the tube restoring force after step elongation is similar to what has been observed for other curvature generating proteins like amphiphysin NBAR¹⁴, but is in striking contrast to the behavior observed for dynamin which showed an abrupt force change only after forming a continuous scaffolding shell around the lipid tubule extending from the GUV to the trapped particle⁹.

FBARs of syndapin 1 were found to sense membrane curvatures higher than its own intrinsic curvature both on tubes formed from synthetic lipid mixtures and on tubes formed from brain lipid extracts. Up-concentration of FBAR on the tube relative to the GUV was strongly density dependent with partitioning between low and high curvatures being amplified at lower FBAR densities. Moreover, syndapin 1 was shown to mechanically perturb the membrane tube in a concentration dependent manner, as was measured by force relaxation measurements where the force decay was measured during a step elongation of the tether. Finally, by analyzing the thermal fluctuations of free tubes suspended in a 2D chamber, we measure a five-fold increase in the persistence length of tubes containing FBAR, implying that FBAR has the ability to form lateral intermolecular contacts along tubular structures that stiffen membrane tubes.

Methods

A syndapin 1 SH3 mutant Q396R/E397R, labeled with GFP, was kindly donated by Volker Hauke (Laboratory for Membrane Biochemistry & Molecular Cell Biology, Freie Universität Berlin) and stored in a salt buffer (20 mM HEPES, 150 mM NaCl, pH 7.4). Details about the mutant and the purification process are given in Ref. 20. Details of the materials used are given in Supplementary Information.

Giant unilamellar vesicles (GUVs). GUVs were prepared by electroformation using indium titanium coated slides on which the film was spread and subsequently hydrated. See Supplementary information for more details on the procedure for GUV formation and on formation of tubes.

The experimental Setup is described in Supplementary Information and the principle behind the optical trapping and calibration system is given in^{24,26,35}.

Step elongation experiments. A program was written in Labview (National Instruments) to control the piezo stage to perform a sequence of controlled



movements at different velocities while acquiring data from the photodiode. Initially, the stage was moved at 1 $\mu\text{m/s}$ to form a tether of 5 μm , subsequently we performed two rapid pulls separated by 40 s. Each pull was performed at 10 $\mu\text{m/s}$. During the whole experiment the position of the particle was recorded by the quadrant photodiode at a 45 μs time resolution.

Data analysis. All image analysis was performed in Matlab (The MathWorks, Natick, MA). Vesicle fluorescence intensities for each channel were calculated by thresholding the images using the background level plus one standard deviation of the noise as the threshold. The integrated intensity of all pixels falling above the threshold for the GUV and the tube, respectively, were quantified for both the protein and membrane channel and the relevant ratios were quantified as described in the paper. A polarization correction factor (PCF)²² was found by measuring the residual *Sorting* at tube diameters of $R \sim 100$ nm (where membrane curvature effects should be negligible) and was used to normalize the *Sorting* in all experiments. Tube persistence lengths were analyzed by a custom made Matlab program using the method described in Ref. 36.

Sample preparation. The experimental chamber for tube pulling is described in Supplementary Information. To measure the shape of freely floating tubes we made quasi-2D chambers with a height of ca. 3–5 μm as measured by laser reflection at the glass water interfaces. After coating two clean glass surfaces with α -casein we added 1 μL of solution, containing tubes, onto one glass and subsequently placed the other glass on top without any spacer. The spreading of the droplet forms a hydration layer on the glass and is sufficient for creating a thin 2D layer of a few micrometers.

Further details of the materials and methods for preparing micropipettes and the sample chamber are given in Supplemental information.

- Dharmalingam, E. *et al.* F-BAR proteins of the syndapin family shape the plasma membrane and are crucial for neuromorphogenesis. *J Neurosci* **29**, 13315–13327 (2009).
- McMahon, H. T. & Gallop, J. L. Membrane curvature and mechanisms of dynamic cell membrane remodelling. *Nature* **438**, 590–596 (2005).
- Rao, Y. & Haucke, V. Membrane shaping by the Bin/amphiphysin/Rvs (BAR) domain protein superfamily. *Cell Mol Life Sci* **68**, 3983–3993 (2011).
- Chen, Y., Aardema, J., Misra, A. & Corey, S. J. BAR proteins in cancer and blood disorders. *Int J Biochem Mol Biol* **3**, 198–208 (2012).
- Antonny, B. Mechanisms of membrane curvature sensing. *Annu Rev Biochem* **80**, 101–123 (2011).
- Baumgart, T., Capraro, B. R., Zhu, C. & Das, S. L. Thermodynamics and mechanics of membrane curvature generation and sensing by proteins and lipids. *Annu Rev Phys Chem* **62**, 483–506 (2011).
- Bhatia, V. K. *et al.* Amphipathic motifs in BAR domains are essential for membrane curvature sensing. *EMBO J* **28**, 3303–3314 (2009).
- Peter, B. J. *et al.* BAR domains as sensors of membrane curvature: the amphiphysin BAR structure. *Science* **303**, 495–499 (2004).
- Roux, A. *et al.* Membrane curvature controls dynamin polymerization. *Proc Natl Acad Sci U S A* **107**, 4141–4146 (2010).
- Singh, P., Mahata, P., Baumgart, T. & Das, S. L. Curvature sorting of proteins on a cylindrical lipid membrane tether connected to a reservoir. *Phys Rev E Stat Nonlin Soft Matter Phys* **85**, 051906 (2012).
- Sorre, B. *et al.* Nature of curvature coupling of amphiphysin with membranes depends on its bound density. *Proc Natl Acad Sci U S A* **109**, 173–178 (2012).
- Tian, A. & Baumgart, T. Sorting of lipids and proteins in membrane curvature gradients. *Biophys J* **96**, 2676–2688 (2009).
- Zhu, C., Das, S. L. & Baumgart, T. Nonlinear sorting, curvature generation, and crowding of endophilin N-BAR on tubular membranes. *Biophys J* **102**, 1837–1845 (2012).
- Heinrich, M. C. *et al.* Quantifying Membrane Curvature Generation of *Drosophila* Amphiphysin N-BAR Domains. *J Phys Chem Lett* **1**, 3401–3406 (2010).
- Qualmann, B., Roos, J., DiGregorio, P. J. & Kelly, R. B. Syndapin I, a synaptic dynamin-binding protein that associates with the neural Wiskott-Aldrich syndrome protein. *Mol Biol Cell* **10**, 501–513 (1999).
- Wang, Q. *et al.* Molecular mechanism of membrane constriction and tubulation mediated by the F-BAR protein Pacsin/Syndapin. *Proc Natl Acad Sci U S A* **106**, 12700–12705 (2009).
- Frost, A. *et al.* Structural basis of membrane invagination by F-BAR domains. *Cell* **132**, 807–817 (2008).
- Bai, X., Meng, G., Luo, M. & Zheng, X. Rigidity of wedge loop in PACSIN 3 protein is a key factor in dictating diameters of tubules. *J Biol Chem* **287**, 22387–22396 (2012).
- Henne, W. M. *et al.* Structure and analysis of FCHO2 F-BAR domain: a dimerizing and membrane recruitment module that effects membrane curvature. *Structure* **15**, 839–852 (2007).
- Rao, Y. *et al.* Molecular basis for SH3 domain regulation of F-BAR-mediated membrane deformation. *Proc Natl Acad Sci U S A* **107**, 8213–8218 (2010).
- Hochmuth, R. M. & Evans, E. A. Extensional flow of erythrocyte membrane from cell body to elastic tether. I. Analysis. *Biophys J* **39**, 71–81 (1982).
- Sorre, B. *et al.* Curvature-driven lipid sorting needs proximity to a demixing point and is aided by proteins. *Proc Natl Acad Sci U S A* **106**, 5622–5626 (2009).
- Kessels, M. M. & Qualmann, B. Syndapin oligomers interconnect the machineries for endocytic vesicle formation and actin polymerization. *J Biol Chem* **281**, 13285–13299 (2006).
- Hansen, P. M., Bhatia, V. K., Harrit, N. & Oddershede, L. Expanding the optical trapping range of gold nanoparticles. *Nano Lett* **5**, 1937–1942 (2005).
- Bendix, P. M. & Oddershede, L. B. Expanding the optical trapping range of lipid vesicles to the nanoscale. *Nano Lett* **11**, 5431–5437 (2011).
- Hansen, P. M., Tolic-Nørrelykke, I. M., Flyvbjerg, H. & Berg-Sørensen, K. Tweezercalib 2.1: Faster version of MatLab package for precise calibration of optical tweezers. *Comp Phys Comm* **175**, 572–573 (2006).
- Zhou, H., Gabilondo, B. B., Losert, W. & van de Water, W. Stretching and relaxation of vesicles. *Phys Rev E Stat Nonlin Soft Matter Phys* **83**, 011905 (2011).
- van Osdol, W. W., Johnson, M. L., Ye, Q. & Biltonen, R. L. Relaxation dynamics of the gel to liquid-crystalline transition of phosphatidylcholine bilayers. Effects of chainlength and vesicle size. *Biophys J* **59**, 775–785 (1991).
- Angelova, M. I. & Dimitrov, D. S. Liposome Electroformation. *Faraday Discuss Chem Soc* **81**, 303–311 (1986).
- Akashi, K., Miyata, H., Itoh, H. & Kinoshita, K., Jr. Preparation of giant liposomes in physiological conditions and their characterization under an optical microscope. *Biophys J* **71**, 3242–3250 (1996).
- Reihani, S. N. S., Mir, S. A., Richardson, A. C. & Oddershede, L. B. Significant improvement of optical traps by tuning standard water immersion objectives. *J. Opt.* **13**, 1–6 (2011).
- Derenyi, I., Julicher, F. & Prost, J. Formation and interaction of membrane tubes. *Phys Rev Lett* **88**, 238101 (2002).
- Bouvrain, H. *et al.* Softening of POPC membranes by magainin. *Biophys Chem* **137**, 7–12 (2008).
- Edeling, M. A. *et al.* Structural requirements for PACSIN/Syndapin operation during zebrafish embryonic notochord development. *PLoS One* **4**, e8150 (2009).
- Richardson, A. C., Reihani, N. & Oddershede, L. B. Combining confocal microscopy with precise force-measuring optical tweezers. *SPIE Proc* **6326**, 28–38 (2006).
- Ott, A., Magnasco, M., Simon, A. & Libchaber, A. Measurement of the persistence length of polymerized actin using fluorescence microscopy. *Phys Rev E* **48**, R1642–R1645 (1993).

Acknowledgements

The work was funded by the Danish-American Fulbright Commission (Grantee ID 34111300), The Carlsberg Foundation, the Villum Foundation, and a University of Copenhagen Center of Excellence: MolPhysX. We thank Volker Hauke (Laboratory for Membrane Biochemistry & Molecular Cell Biology, Freie Universität Berlin) for providing us with F-BAR constructs.

Author contributions

L.B.O. and P.M.B. designed the research. P.R., Y.F.B., S.N.S.R. and P.M.B. carried out experiments. P.R., L.B.O. and P.M.B. wrote the main manuscript text. P.R. and P.M.B. analyzed the sorting data. Y.F.B. measured and analyzed the tube persistence lengths. S.N.S.R. wrote labview software for kinetic pulling experiments. D.S. contributed with reagents. All authors reviewed the manuscript.

Additional information

Supplementary information accompanies this paper at <http://www.nature.com/scientificreports>

Competing financial interests: The authors declare no competing financial interests.

License: This work is licensed under a Creative Commons Attribution-NonCommercial-NoDerivs 3.0 Unported License. To view a copy of this license, visit <http://creativecommons.org/licenses/by-nc-nd/3.0/>

How to cite this article: Ramesh, P. *et al.* FBAR Syndapin 1 recognizes and stabilizes highly curved tubular membranes in a concentration dependent manner. *Sci. Rep.* **3**, 1565; DOI:10.1038/srep01565 (2013).

Supplementary Information

Title: FBAR Syndapin 1 recognizes and stabilizes highly curved tubular membranes in a concentration dependent manner

Authors: Pradeep Ramesh¹, Younes F. Baroji^{1,2}, S. Nader S. Reihani^{1,3}, Dimitrios Stamou^{4,5}, Lene Broeng Oddershede^{1,5}, Poul Martin Bendix^{1,*}.

¹Niels Bohr Institute, University of Copenhagen 2100 Copenhagen, Denmark. ²Department of Physics, Institute for Advanced Studies in Basic Sciences (IASBS), Zanjan 45137-66731, Iran. ³Department of Physics, Sharif University of Technology, PO BOX 11365-9161 Tehran, Iran. ⁴Bionanotechnology and Nanomedicine Laboratory, Department of Chemistry, Nano-Science Center, University of Copenhagen, Universitetsparken 5, 2100 Copenhagen, Denmark. ⁵Lundbeck Foundation Center of Excellence Biomembranes in Nanomedicine. *Corresponding author

SI Materials and Methods

Materials. 1,2-dioleoyl-*sn*-glycero-3-phosphocholine (DOPC), 1,2-dioleoyl-*sn*-glycero-3-phospho-(1'-*rac*-glycerol) (DOPG), and 1,2-distearoyl-*sn*-glycero-3-phosphoethanolamine-N-[biotinyl(polyethylene glycol)-2000] (DSPE-PEG(2000) Biotin), 1-palmitoyl-2-oleoyl-*sn*-glycero-3-phosphocholine (POPC), as well as Porcine Brain Lipid extract (Polar), were obtained from Avanti Polar Lipids. Texas Red[®] 1,2-dihexadecanoyl-*sn*-glycero-3-phosphoethanolamine, triethylammonium salt (Texas Red[®] DHPE) was obtained from Invitrogen and dephosphorylated α -Casein from bovine milk was obtained from Sigma-Aldrich. A GFP labeled syndapin 1 SH3 mutant Q396R/E397R, was kindly donated by Volker Hauke (Laboratory for Membrane Biochemistry & Molecular Cell Biology, Freie Universität Berlin) and stored in a salt buffer (20mM HEPES, 150mM NaCl, pH 7.4). Details about the mutant and the purification process are given in (1). Streptavidin coated microspheres (diameter = 4.95 μ m) were purchased from Bangs Laboratories.

Giant Unilamellar Vesicles (GUVs). GUVs were prepared as follows: lipids, consisting of DOPC, DOPG, DSPE-PEG(2000) Biotin, and Texas Red DHPE, were mixed in chloroform and brought to a final concentration of 1mM, according to a molar ratio of 74% PC, 25% PG, 0.7% PEG-Biotin, and 0.3% Texas Red. Brain Lipid GUVs were prepared as follows: 80 μ l of Porcine Brain Lipids were mixed with 14 μ l of DSPE-PEG(2000) Biotin (1 mg/ml) and 6 μ l of Texas Red DHPE (1 mg/ml) in 900 μ l of Chloroform. 10 μ l of lipid solution was then spotted onto indium titanium oxide (ITO)-coated glass slides using a Hamilton syringe and subsequently dried under nitrogen flow for a few seconds. To assist spreading of the highly charged lipid mixture it was found useful to add 30% of methanol to the lipid mixture prior to spreading on the ITO glass. The slides were then placed in a vacuum chamber and allowed to dry for 1h at room temperature. Vesicles were then prepared using electroformation in a 300mM sucrose solution.

Tube persistence lengths Tubes were formed by mixing GUVs and FBARs at a concentration of 3 μ M FBAR. Tubes without FBAR were formed by gentle hydration which is known to result in formation of GUVs and tubes (2, 3). Tubes formed by this method are not very stable and tube diameter will increase over time and round up if stored for days. We found that POPC was better suited for spontaneous tube formation than DOPC; therefore we used POPC in all experiments involving measurements of persistence lengths. The tubes were first imaged using confocal microscopy to obtain the fluorescent image of the tube with low background intensity for size measurement. Subsequently, the fluctuations of the tubes were visualized using a fluorescent lamp and a cooled EMCCD camera (Ixon, Andor) with 56ms time resolution and 162.5nm pixel size.

Sample Preparation. The experimental chamber for tube pulling was fabricated as follows: a thin, square frame was excised from PDMS and lightly coated with vacuum grease to facilitate adhesion to a clean glass slide (25 X 50 mm #1). In force measurements where the quadrant photodiode was used the chamber had to be closed with a top coverglass to allow immersion oil condenser to be used. For these experiments we used a horse-shoe shaped chamber where one of the sides on the square PDMS frame was removed to allow the pipette to enter the chamber. 200 μ l of α -Casein solution (2 mg/ml) was then added to the volume and allowed to incubate for 15 minutes. The chamber was then successively washed with buffer (15mM NaCl, 270mM Sucrose), upon which GUVs incubated with a set concentrations of FBAR syndapin 1 were then gently pipetted into the chamber. Streptavidin coated microspheres (diameter=4.95 μ m) were added to the chamber just before transferring the sample to the microscope and the system was allowed to equilibrate over a period of 10 minutes before imaging.

Glass micropipettes were fabricated using a micropipette puller (P-97 Flaming/Brown Micropipette Puller, Sutter Instruments) and microforged to a diameter of 5 μ m to 10 μ m using Micro Forge MF-900, Narishige co. ltd Japan. The pipettes were back-filled with coating solution (2 mg/ml α -Casein in 15mM NaCl and 270 mM Sucrose) to prevent irreversible adhesion of membrane lipids to bare glass.

Tube radius measurements

Tube radii were calculated from the measured membrane tension, σ , and the bending rigidity, κ , of the membrane as given in eq. S1.

$$R_{tube} = \sqrt{\frac{\kappa}{2\sigma}} \quad \text{eq.S1}$$

The membrane tension is found by measuring the aspiration pressure ΔP , the pipette radius, R_p , and the radius of the GUV, R_{GUV} , used in the aspiration experiments and by applying eq. S2.

$$\sigma = \Delta P \frac{R_p}{2(1 - R_p / R_{GUV})} \quad \text{eq. S2}$$

where ΔP is the difference in pressure inside and outside the micropipette measured using a differential pressure transducer, DP103 Validyne Engineering, CA. For each pressure we measured the tube/GUV intensity ratio for the membrane incorporated dye TR-DHPE. The measured relation between the tube radius and the tube/GUV intensity ratio is plotted in Fig. S1. The slope of the curve in Fig. S1 is used in the experiments to find the tube radius from the fluorescently measured tube/GUV ratio.

Tube holding force

The equilibrium force needed to hold the tube is determined from the membrane tension, σ , and the bending rigidity κ ,

$$f = 2\pi\sqrt{2\sigma\kappa}. \quad \text{eq. S3}$$

For proteins having tubulating activity eq. S3 is modified to yield (4),

$$f = 2\pi\sqrt{2\sigma\kappa + \kappa^2 C_s^2} - 2\pi\kappa C_s \quad \text{eq. S4}$$

Where C_s is the spontaneous curvature adopted by the tube in presence of the protein.

Mobility of the protein on the tube

A part of the tube or GUV was bleached by significantly increasing the laser power and the subsequently recovery of the bleached region was quantified as a function of time, see Fig. S5C. The diffusion constant was found by applying a model for diffusion in one-dimension (5) describing the recovered fraction, R , as a function of time

$$R(t) = \frac{1}{L} \int_{x_1}^{x_2} dx \left\{ 1 - \frac{1}{2} \left[\operatorname{erf} \left(\frac{s-x+L}{2\sqrt{Dt}} \right) + \operatorname{erf} \left(\frac{s+x+L}{2\sqrt{Dt}} \right) \right] \right\} \quad \text{eq. S5}$$

where D is the diffusion coefficient, $L = x_2 - x_1$ is the length of the bleached tube segment, s is the distance to the source which in this case is the GUV reservoir and erf is the error function. The model assumes a reflecting boundary condition at the position of the trapped bead at which the diffusing molecules are reflected at the end of the tether (5). Nonlinear least square fitting was used to fit eq. 5 to the data presented in Fig. 5C, by using D as a fitting parameter, giving $D = 0.6 \mu\text{m}^2/\text{s}$.

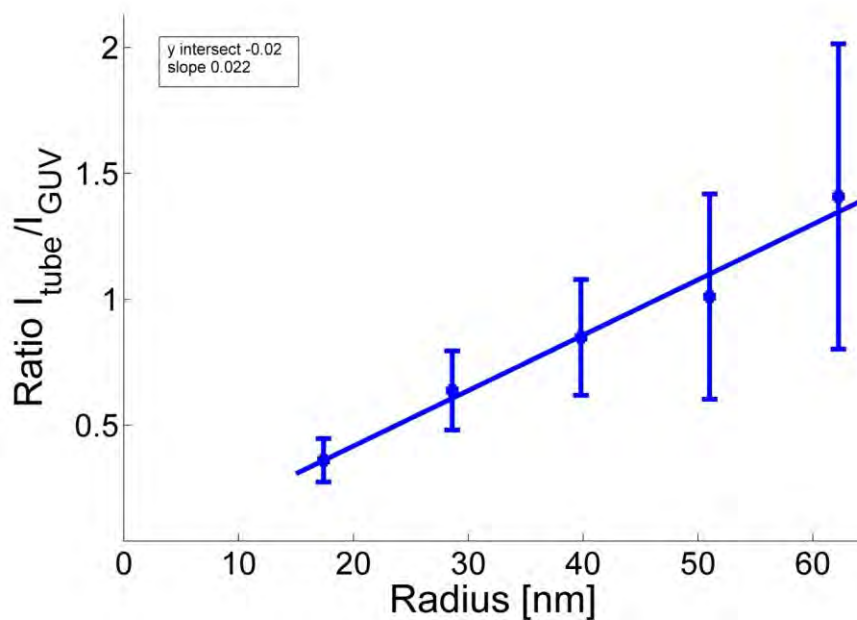


Figure S1 Calibration of tube/GUV intensity ratio versus tube radius. By varying the suction pressure different tube radii were obtained, see eq. S1-S2 (6, 7). Data were collected from 8 vesicles and errorbars denote the standard deviation of the data points in each bin. The straight line fit goes approximately through zero (-0.02), indicating essentially no partitioning of the lipid marker (TR-DHPE).

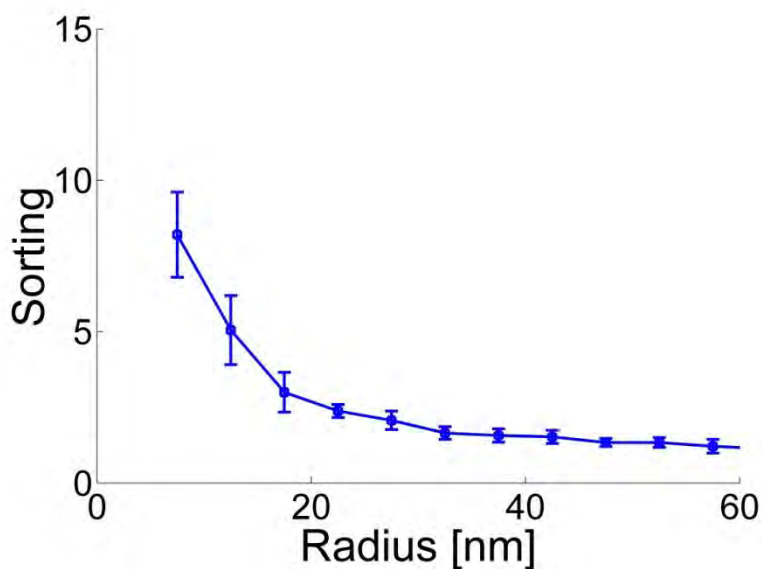


Figure S2 Membrane curvature sorting of FBAR on brain lipid tubes at high electrolyte concentration, $[\text{NaCl}] = 100\text{mM}$. The protein density is almost 10 fold higher on the smallest tubes relative to flat membranes. Since binding of FBAR to model membrane mixtures at high

salt concentrations is inefficient, similar experiments could not be carried out with membranes made from 25 mol% DOPG and 74 mol% DOPC. The graph represents a collection of three experiments.

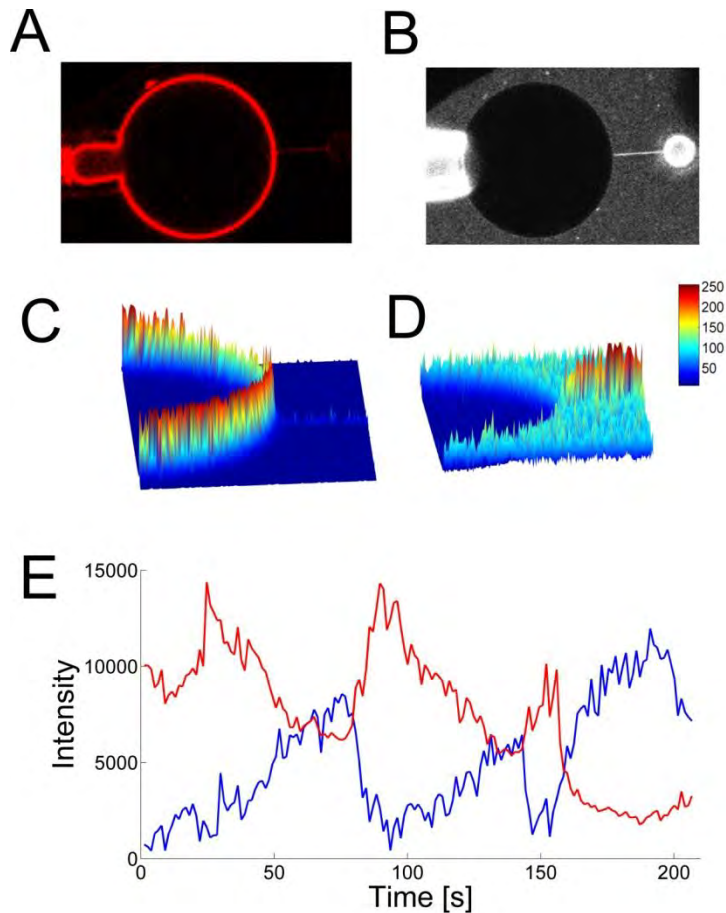


Figure S3 Membrane curvature sensing at low FBAR density. The membrane composition is 84% DOPC, 15 % DOPG and the salt concentration was kept low at 24mM. (A) Image of the GUV membrane, contrast has been enhanced to make the tube more visible. (B) Pulling of a membrane tube shows up-concentration of FBAR on the tether relative to the GUV. (C+D) Surface plots of the images in (A) and (B) showing significant up-concentration of FBAR on the tube relative to the GUV membrane. (E) Membrane tube intensity and FBAR intensity plotted over time while the aspiration pressure and hence the tube diameter is varied over time. Red curve represents the membrane intensity (TR-DHPE) that is proportional to the tube diameter. Blue line represents the signal from the FBAR (labeled with GFP) and is proportional to the protein density. The protein density is seen to be anti-correlated with the tube diameter clearly demonstrating strong sensing of the membrane curvature by FBAR.

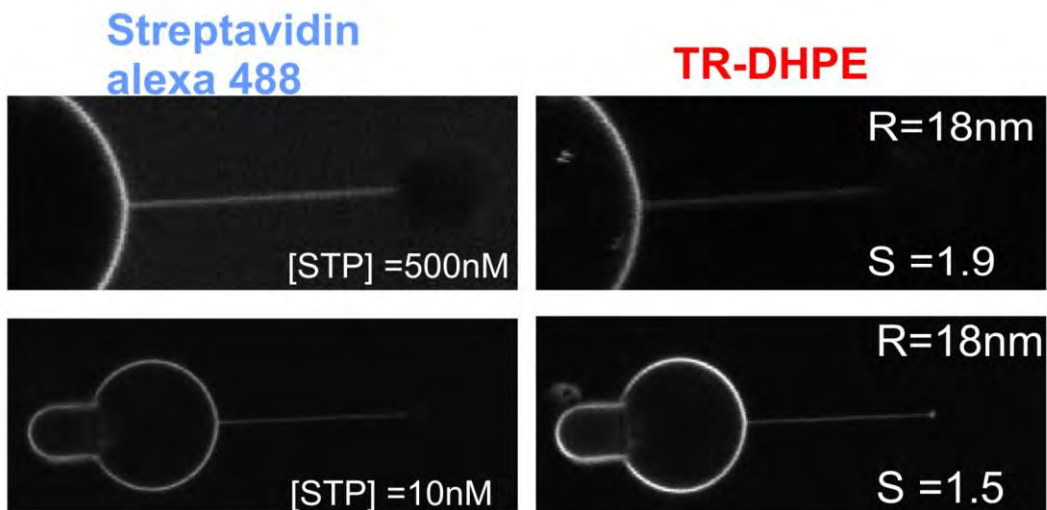


Figure S4 Control experiment showing that streptavidin binding to biotin linkers displayed on the membrane surface does not strongly sense curvature. Streptavidin is labeled with Alexa Fluor⁴⁸⁸ and the bilayer is labeled with 0.3 mol% TR-DHPE and contains 0.7mol% Biotin-PEG2000-DSPE. Streptavidin binds to the biotin linkers on the GUVs surface and hence competes with the streptavidin binding of the trapped particles to the GUVs that are needed to pull out membrane tubes. As a consequence tethers detached more frequently than in FBAR experiments but we obtained several images from tethers that were stable for tens of seconds.

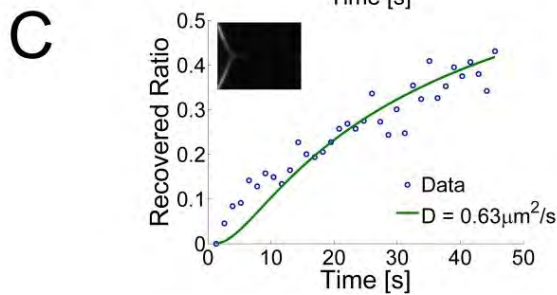
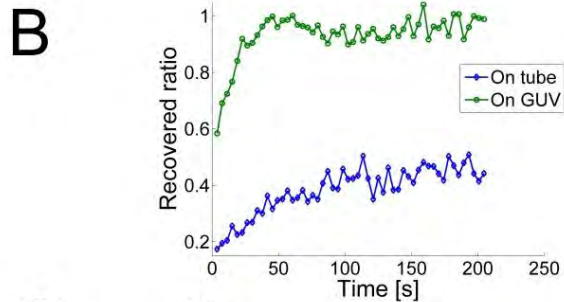
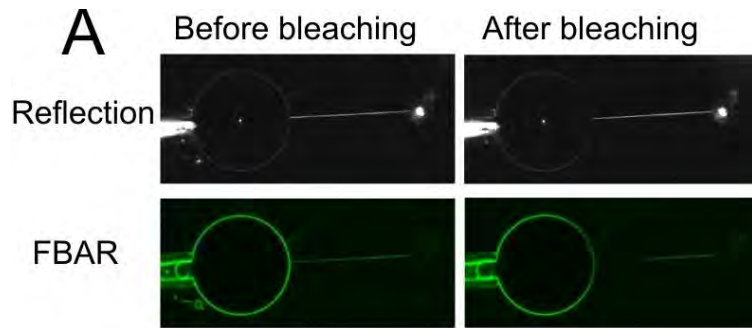


Figure S5 FRAP experiments demonstrating the mobility of FBAR at the same concentrations as used in the sensing experiments (500nM). (A) Images of the GUv and tether before (left images) and after bleaching (right images). The black and white images are recorded in reflection mode to ensure that the bleached portion of the tether remains in focus during the experiment. The colored images are fluorescence images of Syndapin FBAR. The junction between the GUv and the tether is bleached. (B) Recovery on the tube (blue diamonds) and on the GUv (green circles) at 500nM FBAR bulk concentration. (C) Recovery of fluorescent intensity after bleaching on the tube. The recovery trace was fitted to a one-dimensional diffusion model described by eq. S5 yielding a diffusion coefficient of $D=0.63\mu\text{m}^2/\text{s}$. Inset shows the gradient along the bleached tube (contrast enhanced).

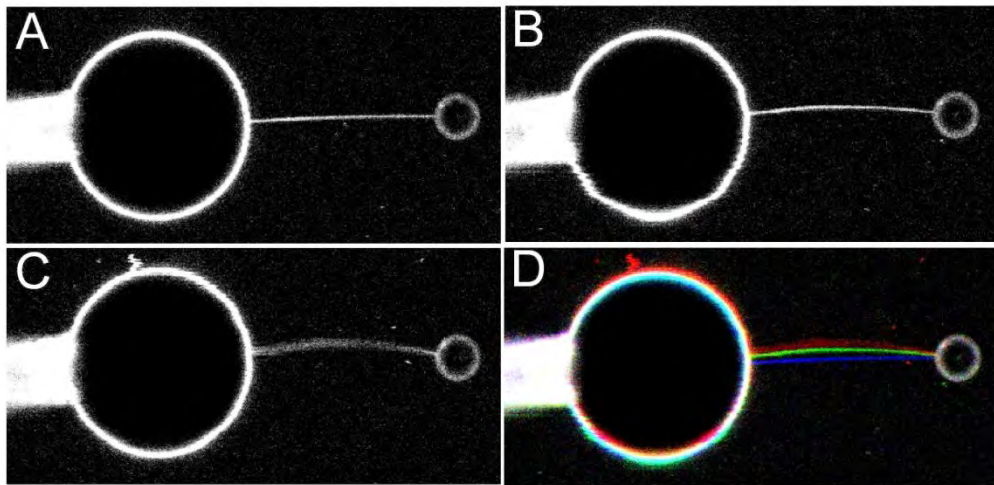


Figure S6 FBAR changes the curvature elasticity of the lipid tube. (A) After aspiration of the GUV into the micropipette a tube is pulled and entirely located within the focal imaging plane. (B) The aspiration pressure is lowered and the aspirated membrane area flows back into the GUV and the tube leading to an elongation of the tube. (C) The aspiration pressure is further decreased, the tether further elongates and goes out of the imaging focus plane. (D) Color overlay of the images in A (blue), B (green) and C (red). All intensities originate from the fluorescently labeled FBAR and have been contrast enhanced for visibility.

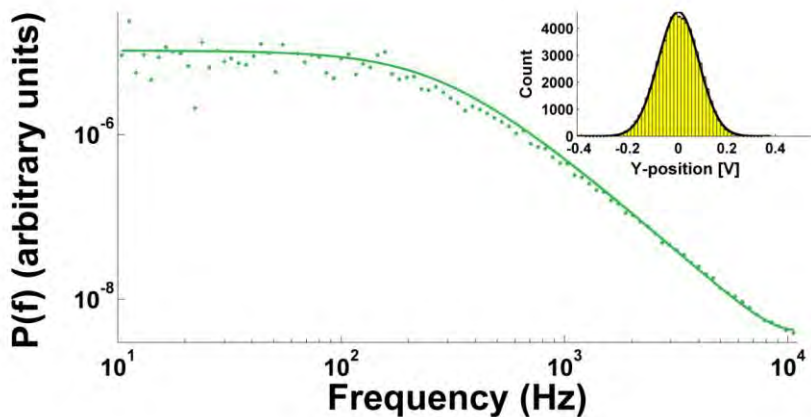


Figure S7. Calibration of the optical trap using powerspectral calibration. A timeseries of 3s is Fourier transformed and the power spectrum is fitted to a Lorentzian with the cornerfrequency, f_c , as a fitting parameter. The figure shows the calibration of one of the beads used for the experiments shown in Fig. 3, yielding $f_c = 261.1 \pm 6.1$ Hz. Full line shows the

Lorentzian fit. The trap was calibrated before attachment of the particle to the membrane. The inset shows the Gaussian position distribution reflecting the harmonic trapping potential.

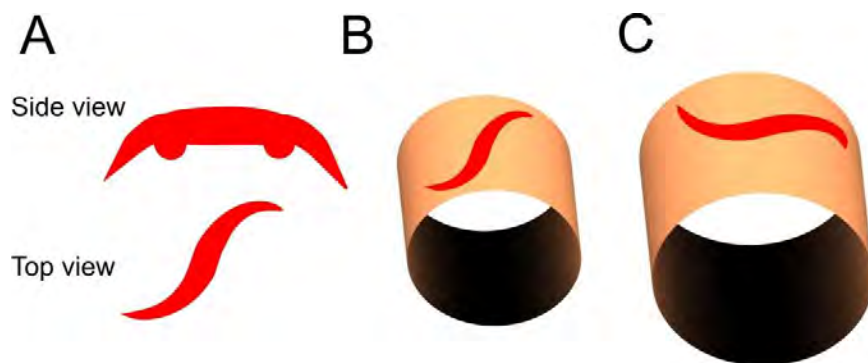


Figure S8 The shape of syndapin 1 FBAR fits well to tubes having high membrane curvature. (A) Schematics of the two dimensional curvature of syndapin 1. The concave curvature is seen from the side as well as the two hydrophobic wedge loops that are positioned at the end of the central part of the protein near the tip regions. The tip regions are also bent away from the central part of the protein with an angle of ca. 61° (8) giving the protein a pronounced two dimensional curvature.

Legend for Video 1

Video showing the up-concentration of FBAR on the tube shown in Fig. S3. The lipid composition in this experiment has low charge density (15% DOPG) which leads to low density of protein on the GUV (below the background). However, the protein still binds to the tube when the tube diameter decreases. The tube diameter is varied, as shown in Fig. S3, by varying the aspiration pressure.

References

- 1) Rao Y, *et al.* (2010) Molecular basis for SH3 domain regulation of F-BAR-mediated membrane deformation. *Proc Natl Acad Sci U S A* 107(18):8213-8218.
- 2) Angelova MI & Dimitrov DS (1986) Liposome Electroformation. *Faraday Discuss Chem Soc* 81:303-311.
- 3) Akashi K, Miyata H, Itoh H, & Kinosita K, Jr. (1996) Preparation of giant liposomes in physiological conditions and their characterization under an optical microscope. *Biophys J* 71(6):3242-3250.

- 4) Heinrich MC, *et al.* (2010) Quantifying Membrane Curvature Generation of Drosophila Amphiphysin N-BAR Domains. *J Phys Chem Lett* 1:3401-3406.
- 5) Zhu C, Das SL, & Baumgart T (2012) Nonlinear sorting, curvature generation, and crowding of endophilin N-BAR on tubular membranes. *Biophys J* 102(8):1837-1845.
- 6) Hochmuth RM & Evans EA (1982) Extensional flow of erythrocyte membrane from cell body to elastic tether. I. Analysis. *Biophys J* 39(1):71-81.
- 7) Kwok R & Evans E (1981) Thermoelasticity of large lecithin bilayer vesicles. *Biophys J* 35(3):637-652.
- 8) Wang Q, *et al.* (2009) Molecular mechanism of membrane constriction and tubulation mediated by the F-BAR protein Pacsin/Syndapin. *Proc Natl Acad Sci U S A* 106(31):12700-12705.

Fluorescent quantification of size and lamellarity of membrane nanotubes

Younes F. Baroji · Lene B. Oddershede ·
Seyed Nader Seyed Reihani · Poul M. Bendix

Received: 22 April 2014 / Revised: 28 August 2014 / Accepted: 8 September 2014 / Published online: 26 September 2014
© European Biophysical Societies' Association 2014

Abstract Membrane nanotubes, ubiquitous in cellular systems, adopt a spectrum of curvatures and shapes that are dictated by their intrinsic physical characteristics as well as their interactions with the local cellular environment. A high bending flexibility is needed in the crowded cytoplasm where tubes often need to bend significantly in the axial direction at sub-micron length scales. We find the stiffness of spontaneously formed membrane nanotubes by measuring the persistence length of reconstituted membrane nanotubes freely suspended in solution and imaged by fluorescence microscopy. By quantifying the tube diameter we demonstrate for the first time that the persistence length scales linearly with radius. Although most tubes are uni-lamellar, the predicted linear scaling between tube radius and persistence length allows us to identify tubes that spontaneously form as multilamellar structures upon hydration. We provide the first experimental evidence that

illumination of lipid fluorophores can have a profound effect on the lipid bilayer which we sensitively detect as a continuous change in the tube persistence length with time. The novel assay and methodology here presented has potential for quantification of the structural reinforcement of membrane tubes by scaffolding proteins.

Keywords Persistence length · Membrane nanotube · Fluorescence · Confocal microscopy · Lamellarity · Vesicle

Introduction

Cells contain complex networks of highly curved tubular membranes important for cellular transport and compartmentalization (Sciaky et al. 1997; Voeltz et al. 2006). Extracellular lipid tubes also function as inter-cellular communication channels called Tunneling Nanotubes (TNTs) (Iglič et al. 2007; Rustom et al. 2004) that are used by cells to convey specific chemical signals or even as transport channels for larger cargos like liposomes, viruses or organelles (Gerdes and Carvalho 2008) between cells. Shorter tubular structures are also abundant in cells, e.g., as transient neck regions connecting spherical membranes with the plasma membrane in fusion intermediates (Chen and Scheller 2001) or in invaginations like endocytosis (Hurley and Hanson 2010). In pathogenesis, tubular membranes, called invadopodia, are essential structures for the invasiveness and metastatic potential of cancer cells (Kabaso et al. 2011). These very essential functions of lipid nanotubes in life make it highly desirable to understand their basic biophysical properties.

To better understand the role of membrane tubes in cells and their interplay with membrane associated proteins and chemicals, different model membrane systems

Electronic supplementary material The online version of this article (doi:10.1007/s00249-014-0989-2) contains supplementary material, which is available to authorized users.

Y. F. Baroji · L. B. Oddershede · S. N. Seyed Reihani (✉) ·
P. M. Bendix (✉)
Niels Bohr Institute, University of Copenhagen,
Blegdamsvej 17, 2100 Copenhagen, Denmark
e-mail: sreihani@physics.sharif.edu

P. M. Bendix
e-mail: bendix@nbi.dk

Y. F. Baroji
Department of Physics, Institute for Advanced Studies in Basic
Sciences (IASBS), Zanjan 45137-66731, Iran

S. N. Seyed Reihani
Department of Physics, Sharif University of Technology,
Tehran 11365-9161, Iran

have been used. Molecular motors can be efficiently used to create membrane tubes out of lipid reservoirs (Koster et al. 2003; Shaklee et al. 2008) but another assay that gives a higher degree of control over the tube radius are membrane tubes pulled out of Giant Unilamellar lipid Vesicles (GUVs) using optical tweezers (Cuvelier et al. 2005; Heinrich and Waugh 1996). The control over tube radius (typically between 10 and 100 nm) by regulating the membrane tension makes this assay ideal for quantifying the affinity of proteins for tubes of different diameter as recently demonstrated for the FBAR domain of Syndapin 1 (Ramesh et al. 2013) or for investigating the effect of cholesterol on the Nano-mechanical properties of membranes (Khatibzadeh et al. 2012). One shortcoming of the tether-pulled-from-vesicle assay is the need for applying tension to the membrane in the formation of the tube and the permanent connectivity of the tube to the GUV. Due to this fixation of the tube it is not straight forward to extract interesting information about physical properties of the tube like the persistence length which gives insight into the mechanical properties of the tube. In particular, the persistence length is assumed to yield important information regarding lateral contacts between scaffolding proteins and hence of the protein mediated reinforcement of the membrane tube, as has been shown theoretically (Cui et al. 2013) and experimentally (Frost et al. 2008; Ramesh et al. 2013).

In some very specific cases, it is possible to produce lipid nanotubes with predefined radius by molecular sculpting or templating processes (Kameta et al. 2011). These can be used in drug delivery applications as they are harmless to the body and resistant to microbial attack (Zhou 2008). However, to design the optimal drug delivery container, it is essential to know how the stiffness and strength of membrane tubes relate to their diameter but so far only a few attempts to do so exist (Zhao et al. 2006, 2008).

The persistence length (L_p) of a biopolymer or tube describes the length scale over which it appears straight with respect to thermal fluctuations. L_p depends both on material properties and geometry and is a widely used measure to characterize the mechanical properties of a flexible biopolymer or tube. Therefore, much effort has been put into extracting the persistence length of biopolymers such as actin filaments (~17 μm) (Le Goff et al. 2002; Ott et al. 1993) microtubules (several millimeters) (Gittes et al. 1993), and single-wall carbon nanotubes (26–138 μm depending on diameter of the nanotube) (Fakhri et al. 2009). However, in most studies concerning membrane tubes the persistence length is critically affected by the lamellarity and diameter of the tube, hence information regarding the number of lamella and size of the tube is important if, e.g. the effect of protein binding on the tube stiffness is studied.

Here we present a novel assay for distinguishing uni- and multilamellarity of Phospholipid Nanotubes (PNTs) by correlating their fluorescent intensity with their thermal shape fluctuations while freely suspended in a quasi-two dimensional (2D) space. Our tracking and persistence length finding method is an extension of the method used to find the persistence length of actin filaments (Ott et al. 1993). In addition, by observing the fluorescently labeled membrane tubes in confocal fluorescence microscopy we obtain an accurate value of the fluorophore intensity which scales linearly with tube diameter if within the focal depth and if the tube is unilamellar (Sorre et al. 2012; Stepanyants et al. 2012; Tian and Baumgart 2009). Our analysis confirms the predicted theoretical scaling relation between persistence length and tube radius. We also use the experimentally obtained information to distinguish between unilamellar and multilamellar PNTs. The lamellarity of a PNT is important as it influences the physical properties of the PNT and most likely also the interaction between PNTs and curvature sensing or inducing proteins. Importantly, we find that fluorescent illumination influences the rigidity of PNTs and larger tubular vesicles which form by spontaneous longitudinal shrinking and radial swelling of PNTs.

Phospholipids nanotubes and tubular vesicles

Material

The non-labeled lipids “1-palmitoyl-2-oleoyl-sn-glycero-3-phosphocholine” (POPC) and fluorescent labeled phospholipids 1,2-dihexadecanoyl-*sn*-glycero-3-phosphoethanolamine, triethylammonium salt (Texas Red DHPE) were purchased from Avanti Polar Lipids and Invitrogen, respectively. Dephosphorylated α -Casein from bovine milk used for coating of the sample chamber was purchased from Sigma–Aldrich.

Phospholipid nanotube formation

A phospholipid stock solution was made from POPC and TR-DHPE (98:2 mol%) in concentration of 10 g L⁻¹ in chloroform. 50 μL of this solution was dried out at the bottom of a glass vial in vacuum forming a lipid film on the glass. Subsequently, the lipid film was hydrated with 300 μL of milli-Q water at room temperature for 5 h. Finally, 1 μL from 50 times diluted solution was sandwiched between a cleaned coverslip and a microscope slide which were coated with α -Casein solution (2 mg mL⁻¹) prior to use in order to prevent adhesion of PNTs to the glass surfaces. The chamber was sealed-off with vacuum grease to prevent drying of the sample. A schematic of the sample is shown in Fig. 1a.

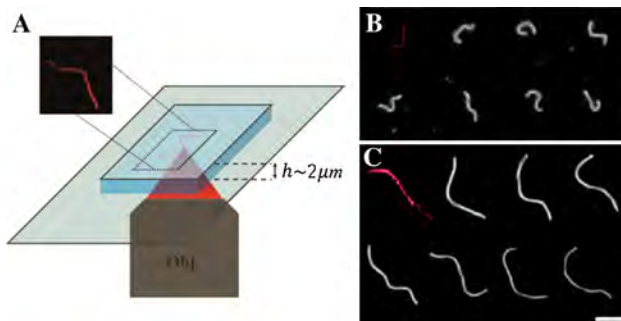


Fig. 1 Assay for imaging fluorescently labeled PNTs. **a** A schematic of the chamber and an image of typical tube that has been captured by confocal microscopy (see also Video 1 in Supplemental Material). **b, c** Seven consecutive images of two different PNTs are displaying a clear difference in intensity levels. The first image in the top left corner of both **b** and **c** is a confocal image used for intensity calibration; the other images were obtained by the EMCCD. A chamber depth of 2–3 μm constrains the PNTs to move in two dimensions and forces them to stay approximately within the focus during the experiment. Each snapshot is separated by 5 s (order of images is from *left to right*, then *top to bottom*). Scale bar is 5 μm

Imaging

Fluorescently marked PNTs were imaged using a confocal microscope (SP5, Leica) where the fluorophores could be excited either by the confocal lasers or by a Hg lamp. A water immersion objective (Leica HCX, PL APO, 63 \times , NA = 1.2 Water Corr CS) was used to minimize spherical aberration while imaging at deeper positions in the sample. A cooled EMCCD camera (Ixon, Andor) was used to record the fluorescent images from Hg excitation. This allowed for a much higher time resolution than the confocal imaging, leading to less time delay between pixels of each frame and hence less blurring of the tether image. Seven consecutive images of two different tubes are shown in Fig. 1b and c, respectively.

The difference in intensity level between the two tubes is proportional to the difference in tube diameter. Pixel size calibration was performed by moving a stuck bead by a piezo stage with steps of 500 nm in the lateral direction while recording its image. One pixel in the EMCCD corresponds to 162.5 nm. The confocal scanning yielded a better axial resolution ($\sim 0.5 \mu\text{m}$), minimizing stray light from out-of-focus; therefore, confocal imaging was used for determining the intensity of each tether. Throughout all experiments the confocal settings were kept constant such that the fluorescence from individual tethers could be directly compared. EMCCD recording allowed for simultaneous recording of all pixels in the image contrary to sequential confocal scanning. Hence, the EMCCD recording of Hg excited fluorophores was used for determining the shape of the tube and hence its persistence

length. In a typical experiment, first a confocal image of the tube was acquired (to determine the intensity of the tube) and then a series of ~ 200 EMCCD images were recorded (to determine its persistence length). An infrared laser (Spectra-Physics J20-BL106Q) coupled into the optical pathway of the microscope was used for thickness measurement of the sample chamber. By measuring the axial distance between reflections of the laser from glass-water interfaces at both sides of the sample chamber and accounting for the focus shift of the laser at larger depths (Reihani et al. 2011) the thickness of the sample chamber was measured to be 2–3 μm allowing for quasi-two dimensional movement of the nanotubes between the surfaces.

Analysis of PNT images

To determine the shape of the filament at different time steps one has to fit a curved line along the tube, a so-called skeleton of the tube. The selection of points along the skeleton is referred to as digitization of the tube. Our digitization method builds upon the method presented by Ott et al. (1993) for the digitization procedure we developed a MATLAB program which works as follows: After defining the start position of the nanotube by a click on the image, the program draws a circle with a radius of 3–8 pixels (depending on rigidity of the filament) centered at the starting point (as shown in Fig. 2a). The highest average intensity value along the arc is used to determine the tube elongation direction. The cross section between the most intense part of the arc and the tube defines the second point along the tube. A second circle with same radius is drawn and the procedure is repeated. Connection of the resulting points produces a line, the “crude skeleton” (Fig. 2b). In order to improve the spatial resolution, the program plots an intensity profile perpendicular to the crude skeleton at each pixel. A Gaussian fit to the intensity profiles defines the most-likely center position of the tube with sub-pixel resolution, the skeleton (Fig. 2c). With this method there is no need to convert the image into binary format, thus no part of original data is lost. As a final step, in order to digitize the skeleton, the program plots circles with predefined radii along the skeleton. Intersection of the plotted circles with the skeleton defines the Digitized Points (DP) along the skeleton which are used for persistence length calculations (Fig. 2d, e).

Formation of tubular vesicles

PNTs are not stable and most of them shrink to liposomes or tubular structure in several hours. Initially, after a semi-two dimensional chamber with tubes had been prepared, the majority of the lipid tubes were several microns, up to

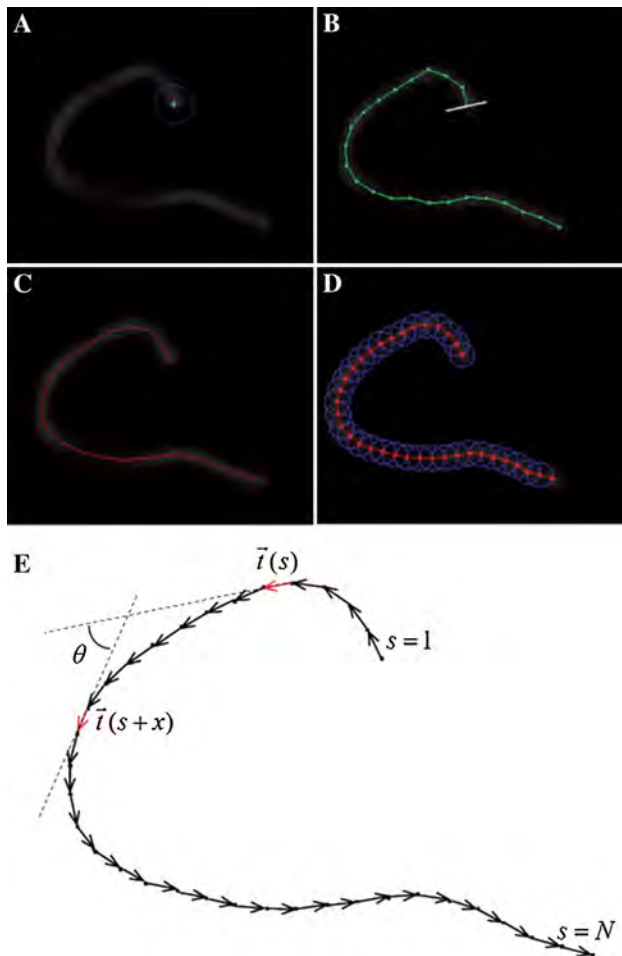


Fig. 2 Illustration of nanotube tracking and digitizing procedure. **a** A circle is drawn with its center at the end of one PNT. The intersection between the arc and the filament determines the center of the next circle. **b** Connection of the circle centers gives the crude skeleton of the PNT. **c** The maximum of the intensity profiles perpendicular to the tube defines the tube skeleton with sub-pixel resolution. **d** The tube is digitized along the skeleton at equal spacing. **e** Tangent vectors on filament

tens of micros, long and their radii were smaller than the resolution limit of light microscopy. But after a while they started to shrink longitudinally and radially expand. Most of the thin tubes, especially the longest ones, shrank and converted to tubular vesicles (see Video 2) with a diameter larger than the diffraction limit (250 nm), hence, the diameter could be estimated from the confocal images. This observation is in accordance with prior observations (Kralj-Iglić et al. 2001; Paredes-Quijada et al. 2009). An example of several tubes transforming from PNTs to tubular vesicles is shown in Fig. S1. In the current work we define a tubular vesicle as a tubular structure where its two membranes could be optically distinguished. The tubular vesicles used in this work have radii approximately between 150 and 600 nm and contour lengths between 3 and 30 μm .

Results and discussion

Quantification of persistence length of PNTs

To measure persistence lengths of PNTs, we located a PNT with both ends free and acquired first a confocal image and then a series of EMCCD images of the tube. Figure 3a show cross-sections of intensities for confocal images of typical PNTs shown in the inset of Fig. 3a. Clearly tube 2 (upper inset) is thicker than tube 1 (lower inset). After digitization of the nanotube skeleton, tangent vectors along the nanotube (one vector at each DP) were extracted. The persistence length of the nanotube, L_p , is related to the correlation of the tangent vectors along the arc, $t(s)$, in the following manner (Fig. 2e) (Dio and Edwards 1986):

$$\langle t(s) \cdot t(s+x) \rangle = \exp\left(\frac{-x}{2L_p}\right) \quad (1)$$

where $\langle \rangle$ where denotes averaging with respect to s . The logarithm of the correlation of tangent vectors along the two tubes shown in Fig. 3a is shown in Fig. 3b as function of separation, x , along the arc. The persistence lengths are derived from the slope of this graph and have values of (2.36 ± 0.08) and (8.32 ± 0.07) μm for the thin and thick tube, respectively.

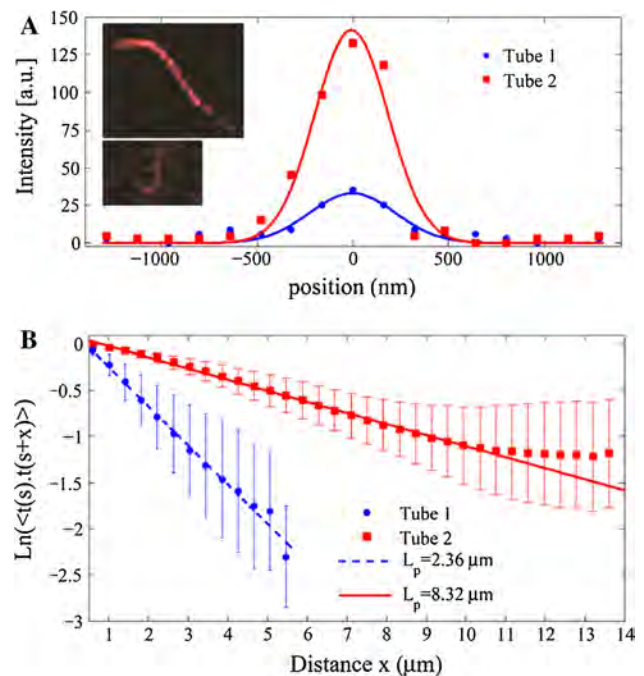


Fig. 3 Quantification of tube persistence length. **a** Intensity profiles across two typical PNTs, insets show confocal images of the tubes. **b** Natural logarithm of the correlation of the PNT tangent vectors along the arc, see Eq. (1). The persistence length of the more intense tube 2 is 8.32 ± 0.07 μm which is significantly larger than that of tube 1, 2.36 ± 0.08 μm

The logarithmic correlation shown in Fig. 3b scales linearly with x for most separation distances. However, for large x there is a deviation from linearity which is caused by the fact that the average is done over a smaller number of data points. Figure S2 shows how the logarithm of the tangent vector correlation changes with number of frames analyzed. The larger the number of frames analyzed, the longer the linear range. In the data analysis only the linear region was used to extract the value of the PNT persistence length.

Nanotube radius

For all analyzed PNTs we measured their persistence length and determined the intensity across the tube (as shown in Fig. 3a). The relation between the persistence length and the maximum intensity across the tube, I_{\max} , for 64 individual tubes is shown in Fig. 4a. The scaling between L_p and intensity is linear for small intensity levels and becomes increasingly scattered for larger tube intensities.

The persistence length of a nanotube is related to its radius, r , by (Derényi et al. 2002; Yamamoto and Ichikawa 2012):

$$L_p = \frac{2\kappa\pi r}{k_B T} \tag{2}$$

where κ and k_B denote the bending rigidity and Boltzmann’s constant, respectively. If the tube diameter is smaller than the confocal imaging depth and if the tube is unilamellar, then:

$$r = \alpha I_{\max} \tag{3}$$

where α is a proportionality constant. This gives:

$$L_p = \frac{2\kappa\pi\alpha I_{\max}}{k_B T} \tag{4}$$

Therefore, for a unilamellar lipid nanotube we expect a linear dependence between the persistence length and the maximum intensity of the tube. We note that TR-DHPE has been shown not to have a preference for certain curvatures (Tian and Baumgart 2009; Ramesh et al. 2013) and therefore we can assume that intensity scales linearly with the thickness of the tube. As it can be seen from Fig. 4 for intensities below ~ 70 a.u. L_p does scale linearly with I_{\max} . In fact, this linear correlation can be extended such that it goes through all the lower data points. The data points well fitted by this line should therefore originate from unilamellar tubes and the data points located above the line probably originate from multilamellar tubes. Also, one can recognize a minimum intensity (~ 30 a.u.) for the nanotubes.

For tubes having walls composed of two or three bilayers we expect the bending rigidity, κ , in Eq. (4) to scale with the total wall thickness, h , as (Rawicz et al. 2000).

$$\kappa = \frac{K_A h^2}{24} \tag{5}$$

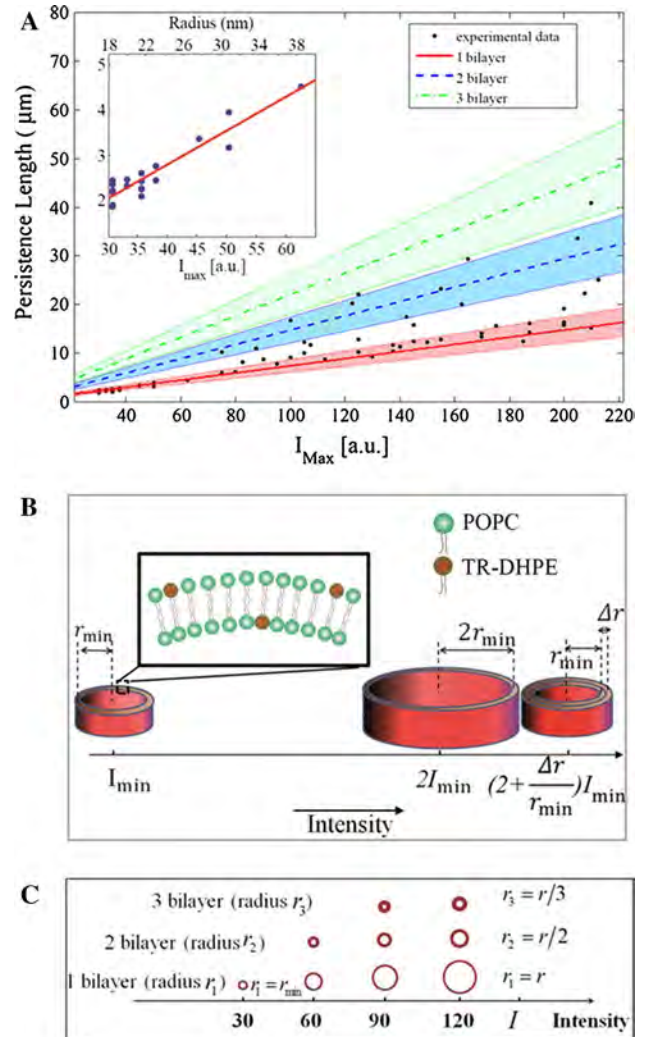


Fig. 4 Quantification of PNT radius and lamellarity. **a** Persistence lengths of PNTs versus the maximum intensity across the tube. The solid red line, dashed blue line and dashed green line correspond to the expected scaling for single, double and trilamellar tubes, respectively (see text). The color shaded regions are relative errors extrapolated from the first data points with $I < 70$. Inset, linear fit of Eq. (5) through data points originating from unilamellar tubes with $I_{\max} < 70$ a.u. The slope directly yields a conversion factor between I_{\max} and tube radius, which is used to create the upper axis of the graph giving values of tube radii. **b** Illustration of the effect of multilamellarity on the fluorescent intensity from a PNT. If the smallest unilamellar PNT has an intensity of I_{\min} , the intensity of a multilamellar PNT starts from $(2 + \Delta r/r_{\min})I_{\min}$, where Δr is the thickness of a lipid bilayer thus explaining the absence of multilamellarity for the tubes having lowest intensity. **c** The scattering of data points in (a) could be due to different combinations of radii and lamellarity which can give similar intensity signals as depicted schematically

where K_A is the area compression modulus. Assuming that 2 bilayers correspond to one bilayer of double thickness we get the following relation for the bending rigidity:

$$\kappa_1 = \kappa \text{ One bilayer}$$

$\kappa_2 = 4\kappa$ Two bilayers

$\kappa_3 = 9\kappa$ Three bilayers

The radius scales with intensity, I , for tubes with 1, 2 or 3 bilayers as $r_1 = \alpha I$, $r_2 = 1/2 \alpha I$, $r_3 = 1/3 \alpha I$ as depicted in Fig. 4c.

Inserting these expressions into Eq. (2) we get for the persistence length for tubes with n bilayers.

$$L_{P_n} = \frac{n2\pi\kappa\alpha}{K_B T} I. \quad (6)$$

Equation (6) is plotted in Fig. 4a together with the data. The data are plotted together with solid and dashed lines corresponding to 1 (solid red), and 2 (dashed blue) and 3 (dashed green) bilayers, respectively. We note that the scattered data points do not follow the blue or green dashed lines but they are rather randomly scattered between the red solid and blue dashed line in Fig. 4a. We thus conclude that we are not only dealing with two closely spaced bilayers but also thinner tubes existing within thicker tubes. Another contribution to the scattering could arise from different combinations of tube radii and lamellarity giving the same intensity, as depicted in Fig. 4b and c. Finally, the measurement error contributes to some scattering [error in measuring intensity of tubes (± 1) and persistence length (~ 5 – 15 %)].

The scattering of the data points in Fig. 4a for intensities larger than 70 could also originate from inhomogeneity of the lipid mixing among different tubes resulting in different intensities from similar tubes. However, due to the large number of fluorescent molecules in each tube ($>10^4$) we do not expect significant statistical fluctuations in the density of fluorophores between different tubes. To confirm this we also measured the intensity from the GUVs that were originally connected with the tubes during electroformation. As shown in Fig. S4 we find the intensities to be centered on values corresponding to distinct number of lamellae which strongly indicates a homogeneous mixing of the lipids. The contribution of the experimental noise to the scattering observed in Fig. 4 was ~ 5 % as revealed by intensity profiles along tube segments that were entirely in focus, see Fig. S5. The intensity profiles plotted in Fig. S5 also clearly reveal that tubes having distinctive intensities can have similar persistence length, thus strongly suggesting the presence of multilamellarity for thick tubes in Fig. 4. Finally, we note that the membrane dye TR-DHPE has been shown to exhibit self-quenching at high concentrations. At 2 mol % as used here we could expect some degree of self-quenching but this will not affect the tube measurements since the quenching will be constant for all tubes given that the density of dyes among the tubes is constant.

For a lipid nanotube the balance between the bending energy of a tube and the surface energy of the corresponding flat membrane area yields a minimum radius, r_{\min} , below which spontaneous tube formation is unfavorable. The bending energy of a tube is given by $E_{\text{bend}} = \kappa n L r^{-1}$ with L and r being the length and the radius of the tube, respectively. The edge energy is given by $E_{\text{edge}} = 2\gamma(2\pi r + L)$ where γ denotes the edge tension of the membrane. For a long and slender tube, the first term of E_{edge} can be neglected. Equating E_{bend} and E_{edge} and solving for r gives the minimum radius of a stable tube; $r_{\min} = \pi\kappa(2\gamma)^{-1}$. For POPC with $\kappa = 19 k_B T$ (Arriaga et al. 2009) and $\gamma = 6 \pm 0.3$ pN (García-Sález et al. 2007) the theoretical minimum radius would be $r_{\min} = 20.4 \pm 1.1$ nm. In order to estimate the minimum radius of nanotubes from experimental results one should note that as visualized in Fig. 4b, the intensity of a PNT with a double bilayer must be larger than twice the minimum intensity because the radius of the outer bilayer must be larger than that of the inner layer. Therefore, it is quite certain that all tubes with I_{max} below ~ 70 a.u. are single bilayer nanotubes. The linear fit shown as a red line in Fig. 4a to data points with I_{max} below ~ 70 returns a value of $\alpha = 0.616 \pm 0.04$. This value can be used to calculate the radius of a unilamellar tube from the measured value of I_{max} through Eq. (3). The resulting tube radii are given in the upper horizontal axis of Fig. 4a inset. Note that the data show minimum radius of 18 nm for PNTs which is in good agreement with the theoretically predicted value.

The persistence length can also be cast in terms of Young's modulus, E , and the moment of inertia, I , describing the tube geometry: $L_p = EI$ and $I = 0.25\pi(r_o^4 - r_i^4)$ where r_o denotes the outer radius and r_i the inner radius of the tube, respectively. When one bilayer is added on a unilamellar PNT, its outer radius increases by (at least) the thickness of the bilayer while its inner radius remains unchanged. The quadratic dependence of the persistence length on the outer radius of the PNT predicts that the increase in the number of bilayers would rapidly increase the persistence length of the PNT. This explains the scattering of the data points for the tubes presented in Fig. 4a.

Effect of fluorescent illumination on tube stiffness

Illumination of fluorescently labeled lipid bilayers has been associated with morphological changes of tubes (Stepanyants et al. 2013) or shrinking of the bilayer area of GUVs (Karatekin et al. 2003; Sandre et al. 1999). We also considered the effect of fluorescent excitation light on the PNTs after long time exposure. During time the PNTs change aspect ratio as they become shorter and thicker (as explained in “Material”), the PNTs evolve into tubular vesicles whose

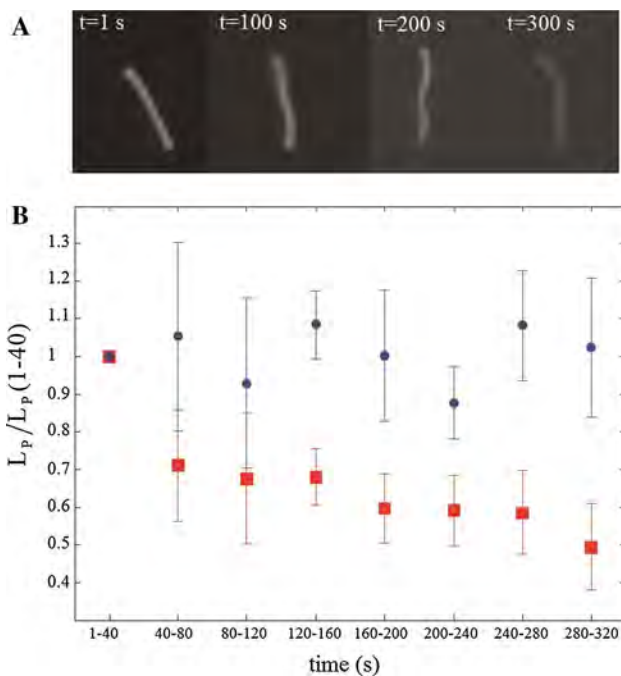


Fig. 5 Effect of illumination on persistence lengths of PNTs and tubular vesicles. **a** A typical tubular vesicle becomes more flexible under illumination with time. The decay in intensity in subsequent frames is due to bleaching. **b** Normalized persistence lengths of PNTs (red squares) and tubular vesicles (blue circles) as a function of illumination time. PNTs are resistant under illumination but tubular vesicles become softer. Error bars represent the standard deviation of 7 PNTs and 7 tubular vesicles, respectively

two bilayers can be optically distinguished. This process takes hours and is shown in Fig. S1. Seven PNTs and seven tubular vesicles were illuminated with a fluorescent lamp for about 5 min and during this time consecutive images of them were captured by a camera. The persistence lengths of each tube during this time were calculated with 40 s sequential steps (Fig. 5). Interestingly, the effect of illumination on the tube persistence length is different on PNTs and tubular vesicles. The persistence lengths of PNTs were constant during the illumination period (blue circle points in Fig. 5), however, for tubular vesicles, the persistence lengths decreased during illumination (red square points in Fig. 5). The decrease in persistence lengths of the tubular vesicles was associated with a gradual increase in the total contour length showing that the tubes radially contract and elongate during intense illumination, see Fig. S3. However, the slight increase in length is in most cases below ~12 % during the period of illumination which cannot alone explain the large decrease in the measured persistence lengths. The consequences of strong illumination has been shown to result in loss of lipid material and an associated increase in bilayer tension (Karatekin et al. 2003). Although the mechanism behind this effect was not resolved we can

expect a similar loss of lipid material in our experiments. For the thinner tubes (PNTs) we did not detect a change in the persistence length during the 5 min of illumination (blue circle points in Fig. 5). The PNTs, used in this work, have diameters ranging from 18 to 100 nm and consequently the lipid bilayer is already strongly curved around the tubular axis. As the bending energy stored in the lipid bilayer scales with r^{-1} a radial shrinking of PNTs would result in a much higher energy increase than for tubular vesicles. This probably explains why relatively uncurved tubular vesicles can become thinner and more flexible upon irradiation whereas highly curved PNTs with diameters of a few tens of nanometers keep a constant diameter and hence a constant persistence length.

Conclusion

We devised a novel fluorescence based method for quantifying the persistence length, diameter and lamellarity of phospholipid nanotubes (PNTs). The values of persistence lengths, L_p , of PNTs ranged from 1 to 40 μm and the radii, r , ranged from 18 to 100 nm. These values are in accordance with previous work on PNTs (Yamamoto and Ichikawa 2012). However, we also found that several of the PNTs, in particular the larger ones, were in fact not unilamellar but multilamellar. This lamellarity of a PNT has huge implications for its physical properties as well as for its interaction with proteins. As several PNTs are multilamellar, the theoretical relation between r and L_p was modified to represent tubes with several bilayers by modeling the multilayer as a bilayer with increased thickness. Values of L_p from PNTs coated by scaffolding proteins have been reported to vary between 9 and 142 μm (Frost et al. 2008; Ramesh et al. 2013). However, our results show that a change in tube radius or the possibility of multilamellarity does have huge influence on L_p and should be considered when investigating the mechanical reinforcement of membrane tubes by scaffolding proteins. Importantly, we also provide the first experimental evidence of the effect of fluorescent illumination on the rigidity of PNTs and tubular vesicles revealing that only tubular vesicles become increasingly flexible due to illumination whereas the much thinner PNTs maintain their rigidity during illumination.

Acknowledgments The authors acknowledge financial support from MolPhysX excellence center at the University of Copenhagen and from the Villum Kann Rasmussen Foundation.

References

Arriaga LR, López-Montero I, Orts-Gil G, Farago B, Hellweg T, Monroy F (2009) Fluctuation dynamics of spherical vesicles:

- frustration of regular bulk dissipation into subdiffusive relaxation. *Phys Rev E* 80(3):031908
- Chen YA, Scheller RH (2001) SNARE-mediated membrane fusion. *Nat Rev Mol Cell Biol* 2(2):98–106
- Cui H, Mim C, Vázquez Francisco X, Lyman E, Unger Vinzenz M, Voth Gregory A (2013) Understanding the role of amphipathic helices in N-BAR domain driven membrane remodeling. *Biophys J* 104(2):404–411
- Cuvelier D, Derényi I, Bassereau P, Nassoy P (2005) Coalescence of membrane tethers: experiments, theory, and applications. *Biophys J* 88(4):2714–2726
- Derényi I, Jülicher F, Prost J (2002) Formation and interaction of membrane tubes. *Phys Rev E* 88(23):238101
- Dio M, Edwards SF (1986) The theory of polymer dynamics. The Clarendon Press, Oxford University Press, New York, pp 316–317
- Fakhri N, Tsybouski DA, Cognet L, Weisman RB, Pasquali M (2009) Diameter-dependent bending dynamics of single-walled carbon nanotubes in liquids. *PNAS* 106(34):14219–14223
- Frost A, Perera R, Roux A, Spasov K, Destaing O, Egelman EH, De Camilli P, Unger VM (2008) Structural basis of membrane invagination by F-BAR domains. *Cell* 132(5):807–817
- García-Sáez AJ, Chiantia S, Salgado J, Schwille P (2007) Pore formation by a Bax-derived peptide: effect on the line tension of the membrane probed by AFM. *Biophys J* 93(1):103–112
- Gerdes H-H, Carvalho RN (2008) Intercellular transfer mediated by tunneling nanotubes. *Curr Opin Cell Biol* 20(4):470–475
- Gittes F, Mickey B, Nettleton J, Howard J (1993) Flexural rigidity of microtubules and actin filaments measured from thermal fluctuations in shape. *J Cell Biol* 120(4):923–934
- Heinrich V, Waugh R (1996) A piconewton force transducer and its application to measurement of the bending stiffness of phospholipid membranes. *Ann Biomed Eng* 24(5):595–605
- Hurley JH, Hanson PI (2010) Membrane budding and scission by the ESCRT machinery: it's all in the neck. *Nat Rev Mol Cell Biol* 11(8):556–566
- Iglič A, Lokar M, Babnik B, Slivnik T, Veranič P, Hägerstrand H, Kralj-Iglič V (2007) Possible role of flexible red blood cell membrane nanodomains in the growth and stability of membrane nanotubes. *Blood Cells Mol Dis* 39(1):14–23
- Kabaso D, Lokar M, Kralj-Iglič V, Veranič P, Iglič A (2011) Temperature and cholera toxin B are factors that influence formation of membrane nanotubes in RT4 and T24 urothelial cancer cell lines. *Int J Nanomed* 6:495–509
- Kameta N, Minamikawa H, Masuda M (2011) Supramolecular organic nanotubes: how to utilize the inner nanospace and the outer space. *Soft Matter* 7(10):4539–4561
- Karatekin E, Sandre O, Guitouni H, Borghi N, Puech P-H, Brochard-Wyart F (2003) Cascades of transient pores in giant vesicles: line tension and transport. *Biophys J* 84(3):1734–1749
- Khatibzadeh N, Gupta S, Farrell B, Brownell WE, Anvari B (2012) Effects of cholesterol on nano-mechanical properties of the living cell plasma membrane. *Soft Matter* 8(32):8350–8360
- Koster G, VanDuijn M, Hofs B, Dogterom M (2003) Membrane tube formation from giant vesicles by dynamic association of motor proteins. *PNAS* 100(26):15583–15588
- Kralj-Iglič V, Gomišček G, Majhenc J, Arrigler V, Svetina S (2001) Myelin-like protrusions of giant phospholipid vesicles prepared by electroformation. *Colloids Surf A* 181(1–3):315–318
- Le Goff L, Hallatschek O, Frey E, Amblard F (2002) Tracer studies on F-Actin fluctuations. *Phys Rev E* 89(25):258101
- Ott A, Magnasco M, Simon A, Libchaber A (1993) Measurement of the persistence length of polymerized actin using fluorescence microscopy. *Phys Rev E* 48(3):R1642–R1645
- Paredes-Quijada G, Aranda-Espinoza H, Maldonado A (2009) Shapes and coiling of mixed phospholipid vesicles. *Lipids* 44(3):283–289
- Ramesh P, Baroji YF, Reihani SNS, Stamou D, Oddershede LB, Bendix PM (2013) FBAR syndapin 1 recognizes and stabilizes highly curved tubular membranes in a concentration dependent manner. *Sci Rep* 3:1565
- Rawicz W, Olbrich KC, McIntosh T, Needham D, Evans E (2000) Effect of chain length and unsaturation on elasticity of lipid bilayers. *Biophys J* 79:328–339
- Reihani SNS, Mir SA, Richardson AC, Oddershede LB (2011) Significant improvement of optical traps by tuning standard water immersion objectives. *J Opt* 13(10):105301
- Rustom A, Saffrich R, Markovic I, Walther P, Gerdes H-H (2004) Nanotubular highways for intercellular organelle transport. *Science* 303(5660):1007–1010
- Sandre O, Moreaux L, Brochard-Wyart F (1999) Dynamics of transient pores in stretched vesicles. *PNAS* 96(19):10591–10596
- Sciaky N, Presley J, Smith C, Zaal KJM, Cole N, Moreira JE, Terasaki M, Siggia E, Lippincott-Schwartz J (1997) Golgi tubule traffic and the effects of brefeldin A visualized in living cells. *J Cell Biol* 139(5):1137–1155
- Shaklee PM, Idema T, Koster G, Storm C, Schmidt T, Dogterom M (2008) Bidirectional membrane tube dynamics driven by nonprocessive motors. *PNAS* 105(23):7993–7997
- Sorre B, Callan-Jones A, Manzi J, Goud B, Prost J, Bassereau P, Roux A (2012) Nature of curvature coupling of amphiphysin with membranes depends on its bound density. *PNAS* 109(1):173–178
- Stepanyants N, Jeffries GDM, Orwar O, Jesorka A (2012) Radial sizing of lipid nanotubes using membrane displacement analysis. *Nano Lett* 12(3):1372–1378
- Stepanyants N, Zhang H, Lobovkina T, Dommersnes P, Jeffries GDM, Jesorka A, Orwar O (2013) Spontaneous shape transformation of free-floating lipid membrane nanotubes. *Soft Matter* 9(21):5155–5159. doi:10.1039/c3sm50429h
- Tian A, Baumgart T (2009) Sorting of lipids and proteins in membrane curvature gradients. *Biophys J* 96(7):2676–2688
- Voeltz GK, Prinz WA, Shibata Y, Rist JM, Rapoport TA (2006) A class of membrane proteins shaping the tubular endoplasmic reticulum. *Cell* 124(3):573–586
- Yamamoto A, Ichikawa M (2012) Direct measurement of single soft lipid nanotubes: nanoscale information extracted in a noninvasive manner. *Phys Rev E* 86(6):061905
- Zhao Y, Mahajan N, Fang J (2006) Bending and radial deformation of lipid tubules on self-assembled thiol monolayers. *J Phys Chem B* 110(44):22060–22063
- Zhao Y, Tamhane K, Zhang X, An L, Fang J (2008) Radial elasticity of self-assembled lipid tubules. *ACS Nano* 2(7):1466–1472
- Zhou Y (2008) Nanotubes: a new carrier for drug delivery systems. *Open Nanosci J* 2:1–5

Supporting Information

Quantification of persistence length reveals size and lamellarity of membrane nanotubes

Younes F. Baroji, Lene B. Oddershede, S. Nader S. Reihani*, and Poul M. Bendix*

Y.F. Baroji, L. B. Oddershede, S. N.S. Reihani, P.M. Bendix
Niels Bohr Institute, University of Copenhagen, Blegdamsvej 17, 2100 Copenhagen, Denmark

Y.F. Baroji
Department of Physics, Institute for Advanced Studies in Basic Sciences (IASBS), Zanjan
45137-66731, Iran

S. N.S. Reihani
Department of Physics, Sharif University of Technology, Teheran 11365- 9161, Iran

[*] Corresponding authors: sreihani@physics.sharif.edu and bendix@nbi.dk

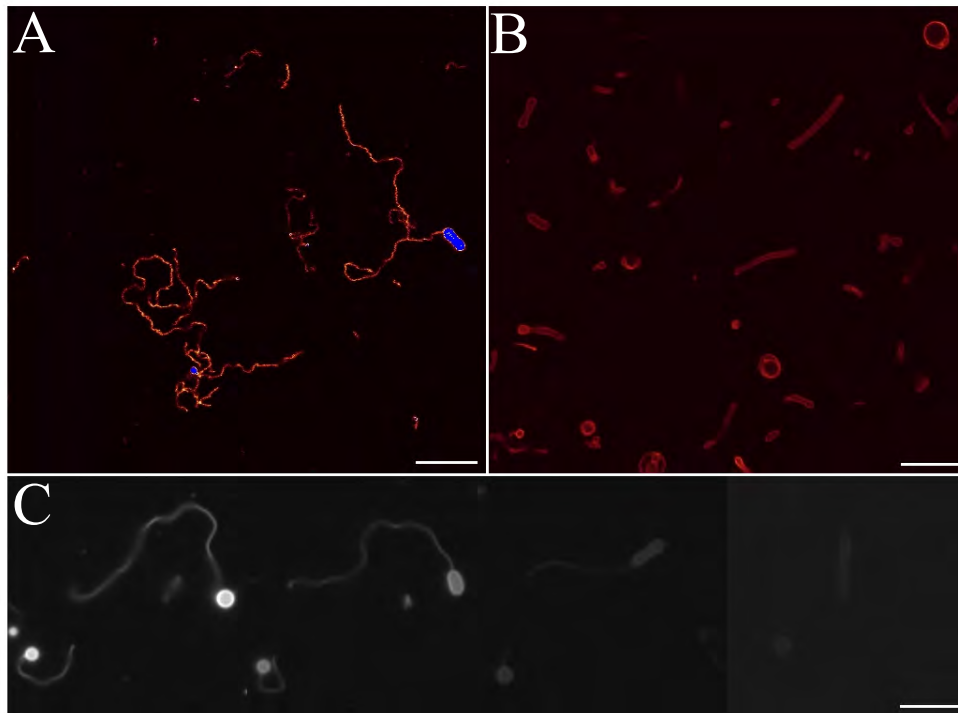


Fig. S1 Spontaneous transformation of PNTs into tubular vesicles. A) Confocal image of PNTs confined in a semi two dimensional chamber. B) After four hours there are many tubular vesicles. C) Consecutive fluorescence images of longitudinal shrinking of PNTs into tubular vesicles and liposome. This change takes several minutes. Scale bar is 10 μm .

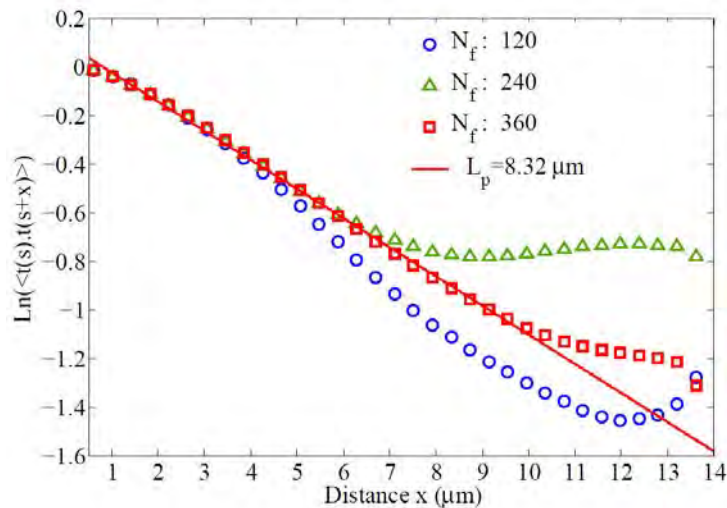


Fig. S2 Logarithm of correlation between the PNT tangent vectors versus separation distance for different numbers of analyzed frames. Data is from the tube shown in Fig. 1C. The number of frames, N_f , used are 120, 240 and 360 frames, respectively. The larger the number of frames, the longer the linear region.

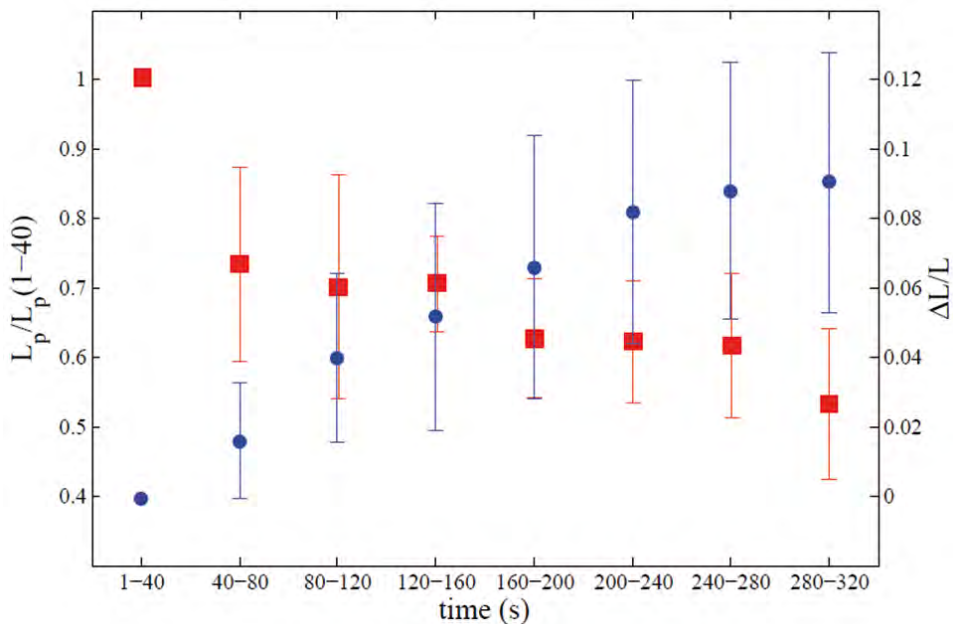


Fig. S3 Effect of illumination on the relative length and on the persistence length of tubular vesicles. Left axis: Normalized persistence lengths of tubular vesicles versus exposure time (red square). Right axis: Relative change of the length of tubular vesicles (blue points).

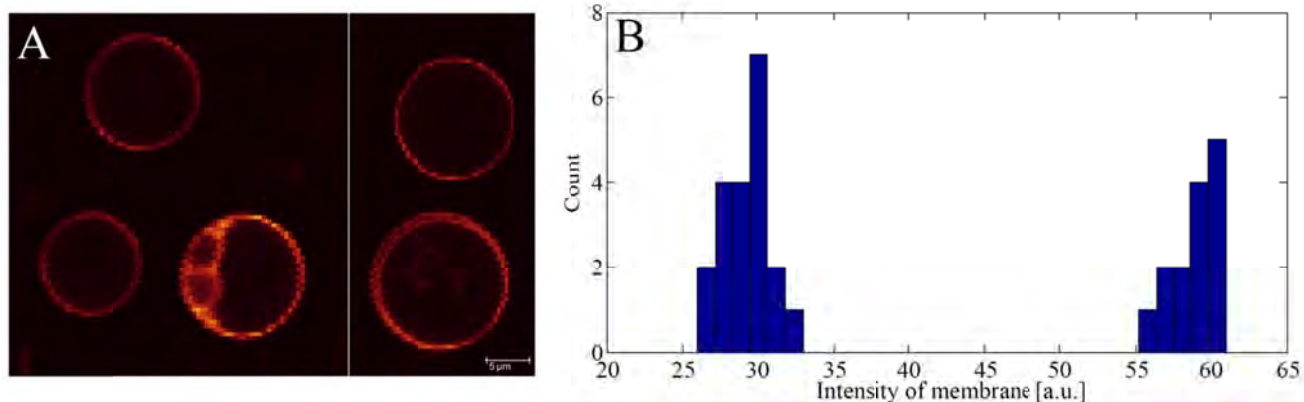


Figure S4 Fluorophores in GUVs are homogeneously distributed. (A) Examples of unilamellar and bilamellar GUVs labeled with 2mol% TR-DHPE and composed of 98mol% POPC. (B) Lamellarity is clearly reflected in the intensity distribution from a number of GUVs. Only around 10% of the GUVs were not unilamellar and in the histogram all of these were selected but only a few of the unilamellar.

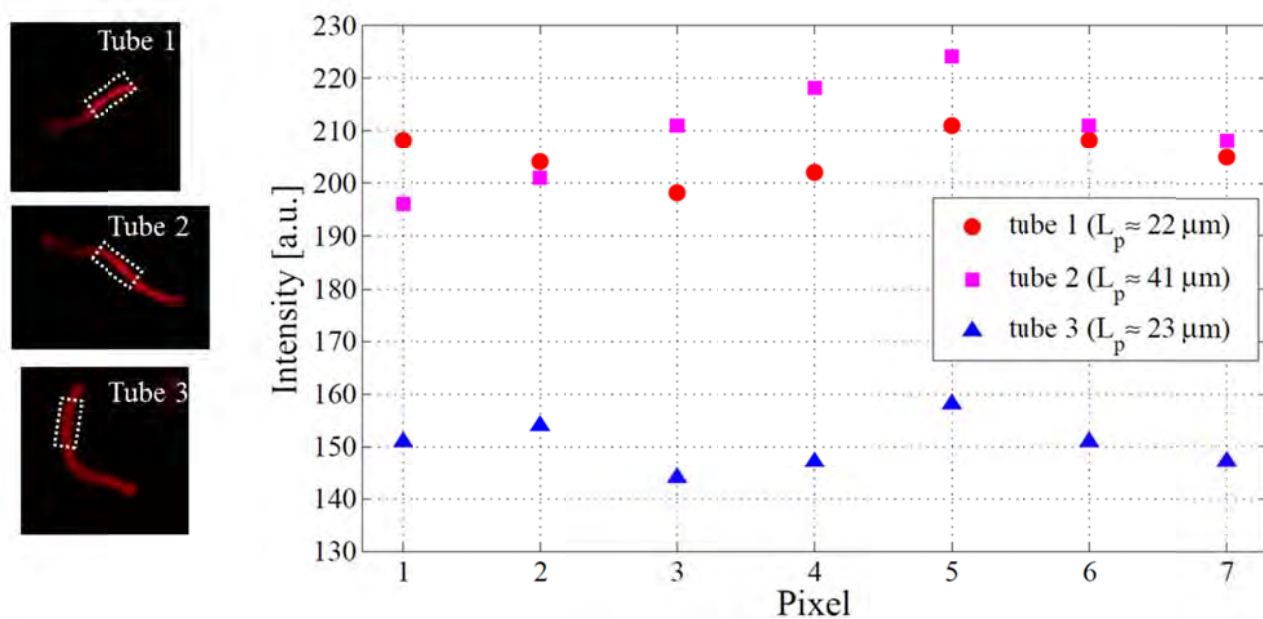


Figure S5 Variability in tube intensity along tubes. The intensity profile for three different tubes is plotted along the tube length. The variability along the tube is $\sim 5\%$ which is an approximate estimate for the experimental uncertainty. Comparing tube 1 and tube 3 we show that tubes having distinctive intensity levels can have similar persistence lengths thus strongly suggesting the presence of multilamellarity in the tubes.

